University of Sussex

Yb ion trap experimental set-up and two-dimensional ion trap surface array design towards analogue quantum simulations

James D. Siverns

Submitted for the degree of Doctor of Philosophy

University of Sussex

June 2011

Declaration

I hereby declare that this thesis has not been and will not be submitted in whole or in part to another University for the award of any other degree.

Signature:

James D. Siverns

UNIVERSITY OF SUSSEX

James D. Siverns, Doctor of Philosophy

Yb ion trap experimental set-up and two-dimensional ion trap surface array design towards analogue quantum simulations

For Dad...

Abstract

Ions trapped in Paul traps provide a system which has been shown to exhibit most of the properties required to implement quantum information processing. In particular, a two-dimensional array of ions has been shown to be a candidate for the implementation of quantum simulations. Microfabricated surface geometries provide a widely used technology with which to create structures capable of trapping the required two-dimensional array of ions. To provide a system which can utilise the properties of trapped ions a greater understanding of the surface geometries which can trap ions in two-dimensional arrays would be advantageous, and allow quantum simulators to be fabricated and tested.

In this thesis I will present the design, set-up and implementation of an experimental apparatus which can be used to trap ions in a variety of different traps. Particular focus will be put on the ability to apply radio-frequency voltages to these traps via helical resonators with high quality factors. A detailed design guide will be presented for the construction and operation of such a device at a desired resonant frequency whilst maximising the quality factor for a set of experimental constraints. Devices of this nature will provide greater filtering of noise on the rf voltages used to create the electric field which traps the ions which could lead to reduced heating in trapped ions. The ability to apply higher voltages with these devices could also provide deeper traps, longer ion lifetimes and more efficient cooling of trapped ions.

In order to efficiently cool trapped ions certain transitions must be known to a required accuracy. In this thesis the $^2S_{1/2} \rightarrow ^2P_{1/2}$ Doppler cooling and $^2D_{3/2} \rightarrow ^2D[3/2]_{1/2}$ repumping transition wavelengths are presented with a greater accuracy then previous work. These transitions are given for the 170, 171, 172, 174 and 176 isotopes of Yb^+.

Two-dimensional arrays of ions trapped above a microfabricated surface geometry provide a technology which could enable quantum simulations to be performed allowing solutions to problems currently unobtainable with classical simulation. However, the spin-spin interactions used in the simulations between neighbouring ions are required to occur on a faster time-scale than any decoherence in the system. The time-scales of both the

ion-ion interactions and decoherence are determined by the properties of the electric field formed by the surface geometry. This thesis will show how geometry variables can be used to optimise the ratio between the decoherence time and the interaction time whilst simultaneously maximising the homogeneity of the array properties. In particular, it will be shown how the edges of the geometry can be varied to provide the maximum homogeneity in the array and how the radii and separation of polygons comprising the surface geometry vary as a function of array size for optimised arrays. Estimates of the power dissipation in these geometries will be given based on a simple microfabrication.

Acknowledgements

Due to nature of the work involved in designing, setting-up and implementing a working ion trapping experiment from scratch parts of the work described in this thesis were carried out as part of a team. Here I will outline the contributions of others:

Chapter 3: Yb^+ ion trap experimental set-up

The ultra high vacuum system described was designed by Altaf Nizamani. It was constructed by Altaf Nizamani with help from James McLoughlin, Robin Sterling and Philippa Young. The macroscopic linear Paul trapped used in this thesis was designed by Robin Sterling and assembled by myself, Marcus Hughes, James McLoughlin and Robin Sterling. The experimental laser set up was designed and set up by myself, Marcus Hughes, James McLoughlin and Robin Sterling. The lasers themselves were built by James McLoughlin and the 780nm Rb reference laser was built by Robin Sterling, both were based on designs by Prof. Ted Hänsch.

Chapter 4: Laser locking using scannable Fabry-Pérot cavities

The scanning cavities used to lock the lasers to the reference laser were designed by James McLoughlin and Robin Sterling. The locking electronics were designed, constructed and tested by myself. The locking program was written and tested by myself and Altaf Nizamani.

Chapter 5: The application of radio frequency voltages to ion traps via helical resonators

The work in this chapter was carried out by myself, Luke Simkins and Seb Weidt.

Chapter 6: An imaging system design for ion trap experiments

The imaging system was designed and constructed by myself with help from Marcus Hughes.

Chapter 7: Experiments with trapped ions

All of the experiments described in this chapter were carried out by myself, Marcus Hughes, Bjoern Lekitsch, James McLoughlin, Altaf Nizamani, Bjoern Stein, Robin Sterling and Seb Weidt. The theory for the heating measurements was researched and explained by Bjoern Lekitsch with help from James McLoughlin.

Chapter 8: Two-dimensional ion trap surface array design optimisation for an analogue quantum simulation

The C^{++} program used to calculate electric fields from surface geometries was written by Bjoern Stein and adapted for two-dimensional arrays of polygons by myself. The optimisation of the surface geometry was carried out by myself with help from Kim Lake and Seb Weidt. The microfabricated design used to calculate the resistance and capacitance of these types of arrays was adapted from one designed by Marcus Hughes.

Personal thanks

Personally, thanks must go to my supervisor Winfried Hensinger who has had the unenviable task of attempting to turn me into a physics researcher. I am thankful for all the time, effort and patience he has put in over the duration of my DPhil. Massive thanks goes to Altaf Nizamani, James McLoughlin and Robing Sterling as without their help from day one I would still be sat in an empty lab and this thesis would simply contain blank pages. Thanks must also go to Marcus Hughes who joined us during the setting up of the experiment and spent many a long evening (and day and night) with us attempting to trap ions. I must also thank all those who have joined us since trapping our first ion: Kim Lake, Bjoern Lekitsch and Seb Weidt for helping push the experiment forwards and for all your help with bits and pieces throughout this thesis. I hope all the work and long hours spent putting the experiment together allows you to achieve things I could only have dreamt of when first setting foot in an empty lab. A special thanks goes to Luke Simkins for all his help with the work for the helical resonator, you helped me complete something that had been bugging me for ages! I would like to thank all the members of Wolfgang Lange's group: Peter Blythe, Matthias Keller, Anders Mortenson and Alex Wilson. They provided advice and ideas that were invaluable during my DPhil, as well as kindly lending various pieces of equipment! I am also grateful to all the undergraduates who have worked in the lab over the years. In particular I would like to thank Dan Brown, Brendan Murray, Ben Pruess, Rajiv Ramasawmy and Joe Randall for their help

towards many aspects of the experimental design. Finally to my mother, brother and sister, Michael Finnie, Sean and Laura Hamerton, Sam Page, Dan Lloyd, Simon Moore and all those from my undergraduate years and, of course, the rest of my family (there are too many of you to mention individually, but you know who you are) you all have, knowingly or not, got me through the last few years and I thank you all.

Publications

Journal Publications

Versatile ytterbium ion trap experiment for operation of scalable ion-trap chips with motional heating and transition-frequency measurements James J. McLoughlin, Altaf H. Nizamani, James D. Siverns, Robin C. Sterling, Marcus D. Hughes, Bjoern Lekitsch, Bjoern Stein, Seb Weidt, and Winfried K. Hensinger, Phys. Rev. A 83, 013406, (2011).

On the application of radio frequency voltages to ion traps via helical resonators J.D. Siverns, L.R. Simkins, S. Weidt, and W.K. Hensinger, Applied Physics B: Lasers and Optics, 2012, Volume 107, Number 4, Pages 921-934.

Optimisation of two-dimensional ion trap arrays for quantum simulation James D. Siverns, Seb Weidt, Kim Lake, Bjoern Lekitsch, Marcus D. Hughes, and Winfried K. Hensinger, New Journal of Physics, Volume 14, 085009, August 2012.

Conference Contributions

Trapped ytterbium ions for scalable quantum technology J.J. McLoughlin, A.H. Nizamani, J.D. Siverns, R.C. Sterling, M.D. Hughes, B. Lekitsch, B. Stein, S. Weidt and W. K. Hensinger. Poster at 1st European Conference on Trapped Ions (ECTI 2010), 19-24 September 2010, at Redworth Hall, County Durham, UK.

Design and setup of an ytterbium ion trap experiment towards scalable ion quantum information processing

Altaf H. Nizamani, James J. McLoughlin, James D. Siverns, Robin C. Sterling, Marcus

Hughes and Winfried K. Hensinger. Poster at ICOLS 2009 - 19th International Conference on Laser Spectroscopy, 08-14 June 2009, Kusshаro, Hokkaido, Japan.

Design and set up of an ytterbium ion trap experiment for quantum information James D. Siverns Talk at QIon09, Workshop on Quantum Information and Quantum Dynamics in Ion Traps, Tel-Aviv, Israel, April 2009.

Towards ion trap array architectures with $^{171}Yb^{+}$ ions
James J. McLoughlin, Altaf H. Nizamani, James D. Siverns, Robin C. Sterling, Merlin Bevan-Stevenson, Nicholas Davies, Jessica Grove-Smith, Marcus Hughes, Ben Johnson, Kieran Lee, Ben S. Pruess, Rajiv Ramasawmy, David N. Scrivener, Tim Short, and Winfried K. Hensinger Poster at Modern Applications of Trapped Ions conference, at Les Houches, France, 18-23 May 2008.

Towards laser cooling and trapping of $^{171}Yb^{+}$ ions: The vacuum system, arbitrary electrode modelling and design of a chip carrier mounted linear Paul trap
Altaf H. Nizamani, Robin C. Sterling, James J. McLoughlin, James D. Siverns, Nicholas Davies, Tim Short and Winfried K. Hensinger. Poster at QuAMP 2007, 10-13 September, 2007, at University College London, London, UK.

Towards laser cooling and trapping of $^{171}Yb^{+}$ Ions: lasers and their stabilisation, transitions, cooling cycles and radio frequency applications for Paul traps
J. D. Siverns, J. J. McLoughlin, R. C. Sterling, B. S. Pruess, J. N. M. Grove-Smith, D.N. Scrivener, A. H. Nizamani and W. K. Hensinger. Poster at QuAMP 2007, 10-13 September, 2007, at University College London, London, UK.

Towards Laser Cooling and Trapping of $^{171}Yb^{+}$ Ions: Lasers, Transitions, Cooling Cycles and the Vacuum Chamber
James J. McLoughlin, Altaf Nizamani, Robin C. Sterling, James D. Siverns, Jessica Grove-Smith, Nicholas Davies, Dave Scrivener and Winfried K. Hensinger Poster at Atomic Physics Gordon conference, at Tilton School, NH, US, July 1-6, 2007.

Contents

List of Tables

List of Figures

Chapter 1

Introduction

The first computers bearing a resemblance to today's were created by Babbage in the 1820s with the aim of tabulating polynomials. Turing then developed the idea of computing with the concept of a universal machine which could be used to simulate any other system [4]. Since these initial steps, the computer has developed into a device used to solve all manner of increasingly complex problems and, thus, revolutionise the world we live in. There exists, however, despite the wide ranging use of these computers, limits to their efficient use as their operation is governed by classical physics. These limits are reached when a classical computer is used to simulate a quantum mechanical system. This is because the time taken to simulate these systems grows exponentially with the size of the quantum system [5]. In order to simulate a quantum system efficiently (with a simulation time which grows linearly with the system size) one has to utilise quantum physics to build a new type of computer.

The idea for a quantum computer was first put forward by Richard Feynman in 1982 who described how quantum bits could be used to perform calculations [5]. This idea was then further developed by Deutsch who suggested that these quantum computers could be used to perform some calculations more efficiently than their classical counterparts [6, 7]. In particular, Shor and Grover developed algorithms which utilised the greater efficiency of quantum computers. The algorithms proved to be far more efficient at the factorisation of numbers and the searching of databases compared with what classical computing would allow [8, 9, 10]. Additionally, it was shown that quantum technology could allow the secure encryption of information due to the impossibility of cloning quantum states [11, 12, 13]. With these developments a quantum computer has become a tantalising prospect for both academic research and industry.

Trapped ion systems have been used to demonstrate many aspects required for quantum

computing [14, 15, 16, 17, 18, 19, 20, 21, 22, 23, 24, 25, 26, 27, 28, 29, 30] and is currently considered to be a leading technology with which to construct a quantum computer. One application of arrays of such trapped ions, or indeed any other quantum technology, is quantum simulation. Classical computers are thought to have the same exponential size growth issue with the simulation of quantum systems as they do with factorising large numbers and searching large databases, whereas quantum simulators feature polynomial scaling. This means that a quantum simulator could provide a tool with which to efficiently simulate a quantum system. Although quantum simulators would only provide the limited ability to simulate quantum systems, and not fully fledged quantum computation, they present an achievable stepping stone between today's classical computers and the quantum computer. Devices of this nature would allow many aspects of physics to be tested and discovered which could be extremely difficult with current classical computation and simulation.

The incorporation of microfabrication techniques into the field of ion trapping provides a way of designing and building large scale structures with which to trap multiple ions [3, 31, 32]. The ability to be able to trap many ions with a microfabricated surface geometry moves the possibility of building a quantum simulator a step closer. However, in order to make quantum simulators a reality it will be necessary to implement and test different types of ion traps, from macroscopic multi-layer traps to microfabricated surface chip traps. To make this task easier an experimental set-up which can house this wide variety of traps without any modification is required. Lasers must be locked to transition wavelengths to provide efficient cooling of the trapped ions, and radio frequency high voltages must be delivered to the trap electrodes. The work in this thesis shows the development of such an experimental set-up with particular focus on efficiently applying radio frequency voltages to ion traps using helical resonators and the development of surface geometries capable of trapping two-dimensional arrays of ions.

In chapters 3 to 6 the design of an Yb^+ ion trap experiment is described. This set-up allows for the operation of both symmetric and asymmetric types of Paul traps with up to 90 electrical connects. The design includes the presence of a chip carrier which allows for various designs of trap to be tested within a short turn around period without the need to redesign parts of the vacuum system housing the experiment for each trap. This provides an experimental base with which improvements in microfabricated chip trap designs can be made. Included in these chapters is an in-depth discussion on the application of radio frequency voltages to ion traps via a helical resonator. The theory behind the helical

resonator is described along with a discussion on how to optimise the design of the helical resonator to provide the highest quality factor for a given set of experimental constraints. This is of importance as higher quality factors act to filter out noise on the rf voltages required to trap ions in Paul type traps. It is thought that the presence of noise on these voltages can contribute towards the heating of trapped ions which can lead to decoherence in interactions required for quantum information processing.

Chapter 7 then describes the trapping of the 170, 171, 172, 174 and 176 Yb^+ isotopes with the experimental set-up described in chapters 3 to 6. Frequency measurements of the $^2S_{1/2} \leftrightarrow ^2P_{1/2}$ and $^2D_{3/2} \leftrightarrow ^3D[3/2]_{1/2}$ transitions are made in this chapter with higher precision that previous work [33]. Also in this chapter a heating rate measurement of a $^{174}Yb^+$ ion is made in a macroscopic symmetric Paul trap compatible with the vacuum system design, using a method described by [34].

Chapter 8 shows how a surface geometry, suitable for microfabrication, can be used to trap a 2D array of ions. It is shown how geometries of this type can be optimised to increase the homogeneity of interactions across the array whilst, simultaneously, maximising the ratio between the decoherence time and the interaction time. This is important as a homogeneous array allows the arrays to be scaled to larger sizes and interactions are required to occur on a faster time-scale than the decoherence of the system in order to allow simulations with a useful fidelity. A device of this nature would enable a 2D array of ions to be used as a quantum simulator providing a computing tool which would outperform even today's most powerful classical computers.

Chapter 2

The Yb^+ ion

2.1 Introduction

This chapter will discuss the atomic structure of Yb^+ ions and how this is exploited for the purpose of their cooling and detection. The energy levels will be shown for all stable isotopes (with the exception of 173). The effect of laser power and detuning from the resonance of transitions will be discussed in terms of the effect on the ion's scattering rate and subsequent detection.

2.2 Creating Ions

Atomic ions are commonly created using either photo-ionisation or electron bombardment of neutral atoms. The photo-ionisation process has the advantage of allowing for isotope selective loading of ions without the need for expensive enriched neutral atom sources. It also has the advantage that it can avoid charge build up occurring on insulating materials close to the ion trap. This is a common source of stray electric fields which perturb the trapping fields created by the trap electrode structures and, ultimately, affect trapping properties. It should be noted, however, that UV lasers have also been found to cause charge build up on some insulators due to the photoelectric effect. In terms of efficiency of ionisation, photo-ionisation has been found to be around two to three times more efficient when compared with electron bombardment [35]. This higher efficiency means that a lower atomic flux can be used with a photo-ionisation technique compared to electron bombardment, resulting in a reduction in coating of trap electrodes which is thought to augment the trapping field leading to heating and other unwanted motional effects.

Figure 2.1 shows the specific photo-ionisation process for neutral Yb atoms which requires the use of two photons. The first photon, at 399 nm, excites the atom from the

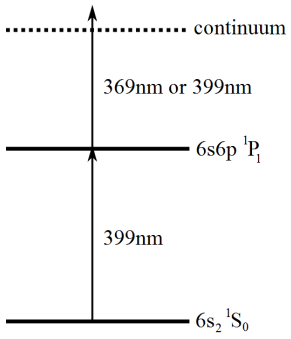

Figure 2.1: Energy level diagram showing the photo-ionisation process for ionisation of neutral Yb atoms.

$6s_2\ ^1S_0$ ground state to the $6s6p\ ^1P_1$ excited state. This first step is the isotope selective part of the ionisation process as the transition frequency is dependent upon the isotope being excited [36]. In order to complete the ionisation process, once in the excited state, a second photon must be absorbed by the atom with a wavelength shorter than 394 nm to remove the exited electron into the continuum. Typically with Yb a 369 nm (a laser present for Doppler cooling of Yb^+ ions) is used for this final step. However, due to the presence of the electric trapping fields the ionisation threshold is reduced allowing a second 399 nm photon to ionise the excited neutral ytterbium atom [35].

2.3 Trapping charged particles

Earnshaw's theorem [37] shows that it is impossible to trap an isolated charged object in free space with the use of just static electric fields. However, charged objects can be isolated and trapped in free space with the use of time dependant electric fields. In the case of Paul type ion traps [38], one typically applies a radio frequency signal to trap electrodes in order to obtain a suitable ponderomotive pseudopotential. Figure 2.2 shows examples of different types of Paul trap designs. The electric quadrupole potential created by the trap structure is given by

$$\Psi(t) = \frac{V(t)\eta}{2r^2}(\alpha x^2 + \beta y^2 + \gamma z^2) \tag{2.1}$$

where $V(t)$ is a time varying voltage applied to the electrodes given by $V(t) = V_0 \cos \Omega t + U$ and r is the distance from the ion to the nearest electrode. η is a geometric efficiency factor [39] (ranging between one and zero) which is equal to one for a perfectly hyperbolic geometry (shown top left in figure 2.2) and decreases as the geometry strays from this

perfect form. The Laplace condition, $\Delta\Psi = 0$, requires that $\alpha + \beta + \gamma = 0$. A simple solution to this requirement occurs when $\alpha = -\beta = 1$ and $\gamma = 0$ along with $U = 0$ and results in a trapping potential given by

$$\Psi(t) = \frac{V(t)\eta}{2r^2}(x^2 - y^2) \tag{2.2}$$

The ponderomotive potential from this trapping potential can be shown to be [39, 40]

$$\psi = \frac{e^2}{4m\Omega^2} |\nabla V(x, y)|^2 \tag{2.3}$$

yielding the pseudopotential

$$\psi = \frac{e^2 V_0^2 \eta^2}{4m\Omega^2 r^4} \left(x^2 + y^2\right) \tag{2.4}$$

where m and e are the mass and charge of the ion respectively, Ω is 2π times the drive frequency in Hertz, r is the distance from the centre of the trap to the nearest electrode and V_0 is the amplitude of the RF voltage applied to the trap.

The secular motional frequency of an ion trapped inside this ponderomotive pseudopotential is then given by [39]

$$\omega^2 = \frac{e^2}{4m\Omega^2} \frac{\partial^2}{\partial x^2} \left(|\nabla V(x, y)|^2 \right) \tag{2.5}$$

yielding

$$\omega = \frac{eV_0\eta}{\sqrt{2}m\Omega r^2} \tag{2.6}$$

A two-dimensional trapping potential in the x and y direction can be created by the linear trap structure shown top right in figure 2.2. This is achieved by applying a time varying potential of $V(t) = U + V_0 \cos \Omega t$. From the resultant electric potential the equations of motion of an ion can be shown to be [38]

$$\ddot{x} + \frac{e}{mr^2}(U + V_0 \cos \Omega t)x = 0 \tag{2.7}$$

$$\ddot{y} - \frac{e}{mr^2}(U + V_0 \cos \Omega t)y = 0 \tag{2.8}$$

There are conditions which exist that enable the trapped ion to have a stable motion in both the x and y dimensions axes. The solutions to the equations of motion (equations 2.7 and 2.8) providing stable motion in both axes are given by the Mathieu equations, which describe the motion of such a system, and are written as

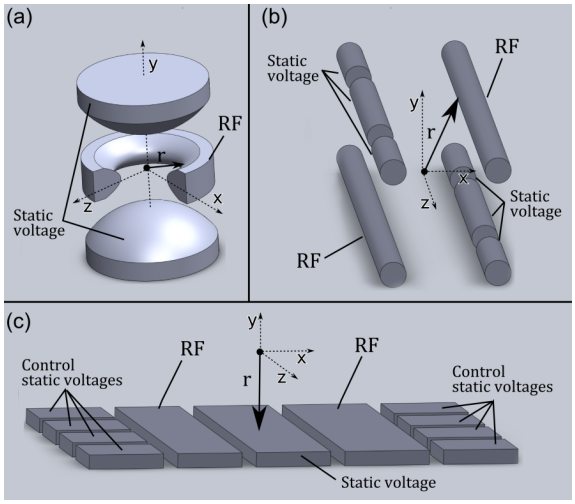

Figure 2.2: (a) Diagram showing a quadrupole Paul trap. The ponderomotive potential due to the RF and static voltage electrodes provide confinement in all three dimensions. All electrodes are hyperbolically shaped (b) A two layer linear Paul trap showing two rod RF electrodes providing transverse confinement with static voltage rod electrodes present to provide confinement in the axial direction of the trap. The static voltage electrodes in this design can also be used to rotate the trapping potentials principle axis to optimise laser interactions with trapped ions. (c) Diagram showing a five wire surface Paul trap. Here the ion is confined in a potential created by the surface electrodes at the midpoint between the two RF strips. Control static voltage electrodes are present to enable control of the potential nil along the length of the trap. This enables ions to be shuttled along the length of the trap.

$$\frac{d^2x}{d\tau^2} + (a + q\cos 2\tau)x = 0 \tag{2.9}$$

$$\frac{d^2z}{d\tau^2} - (a + q\cos 2\tau)y = 0 \tag{2.10}$$

and so by comparison with equations 2.7 and 2.8 the stability parameters a and q an be found to be given by

$$a = \frac{4eU}{mr^2\Omega^2} \tag{2.11}$$

$$q = \frac{2eV_0}{mr^2\Omega^2} \tag{2.12}$$

The stability of a trap depends upon these a and q parameters and figure 2.3 shows the values which provide the stable trapping of an ion in the x direction (areas bounded by solid lines) and the y direction (areas bounded by dashed lines). Figure 2.4 shows a close up of the region useful to ion trapping, when stability is achieved in both the x and y directions simultaneously.

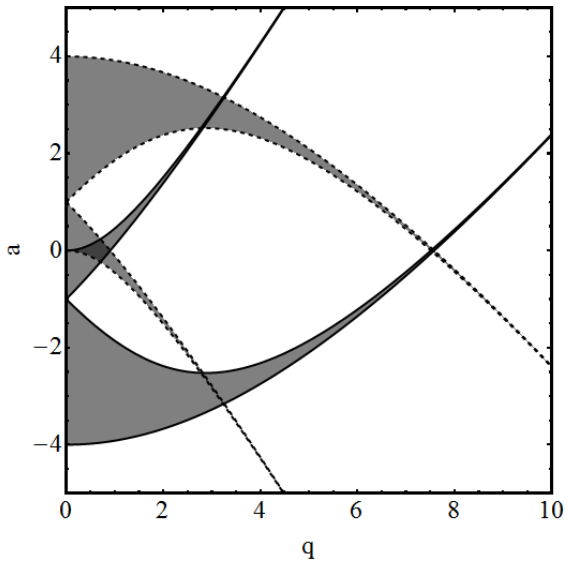

Figure 2.3: Graph showing the values at which the a and q parameters provide stable trapping of an ion in the x direction (area bounded by solid lines) and the y direction (area bounded by dashed lines)

When a linear ion trap (as seen top right in figure 2.2) possesses a and q parameters yielding stable trapping in both the x and y directions (the linear node of the trap) additional confinement along this node can be achieved by additional static voltages applied to certain additional electrodes as shown in figure 2.2.

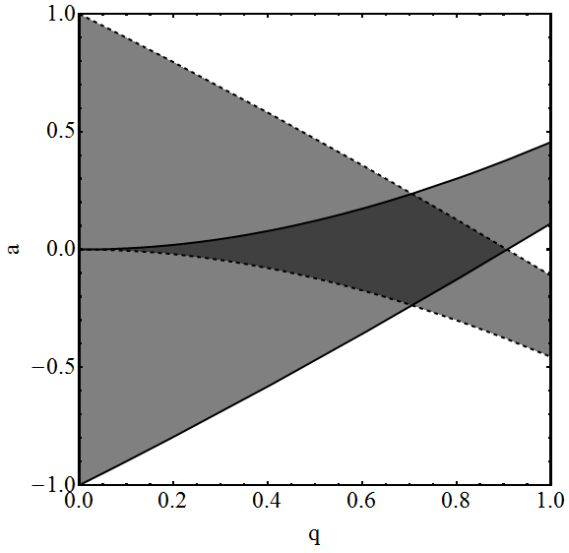

Figure 2.4: Graph showing the values at which the a and q parameters provide stable trapping of an ion in the x direction (area bounded by solid lines) and the y direction (area bounded by dashed lines).

2.4 Ytterbium ion atomic structure

In total there are seven stable isotopes of Yb (168, 170, 171, 172, 173, 174 and 176). During the work carried out in this thesis all the isotopes except 168 and 173 were ionised and trapped. The reason for these exceptions is the low natural abundance of the 168 isotope (less than 1%) and the 173 isotope's 5/2 spin which produces a hyperfine splitting of energy levels which require a combination of laser frequencies which are challenging to produce in order to cool the ion. The 171 isotope also has hyperfine structure, as shown in figure 2.6, however in this case it is relatively simple to produce the laser frequecies required to cool this isotope.

The energy level diagram of an even isotope Yb^+ ion can be seen in figure 2.5. For the purpose of detection and cooling a 369.5 nm laser beam is used to excite the ion from the $^2S_{1/2}$ ground state to the $^2P_{1/2}$ excited state, with spontaneous emission sending the ion back to the ground state. When the ion is in the $^2P_{1/2}$ state, a decay to the metastable state of $^2D_{3/2}$, with a branching ratio of around 0.005, can occur [41, 42]. Since this D-state has a lifetime of around 52 ms a 935 nm laser beam is required to return the ion to the 369.5 nm Doppler cooling cycle. This combination of 369 nm and 935 nm lasers form a closed cooling cycle which produces ion fluorescence at 369 nm. However, even in an ultra high vacuum, inelastic collisions with background gas particles can occur about once an hour which can result in the ion being transferred to the F state, which has a lifetime of

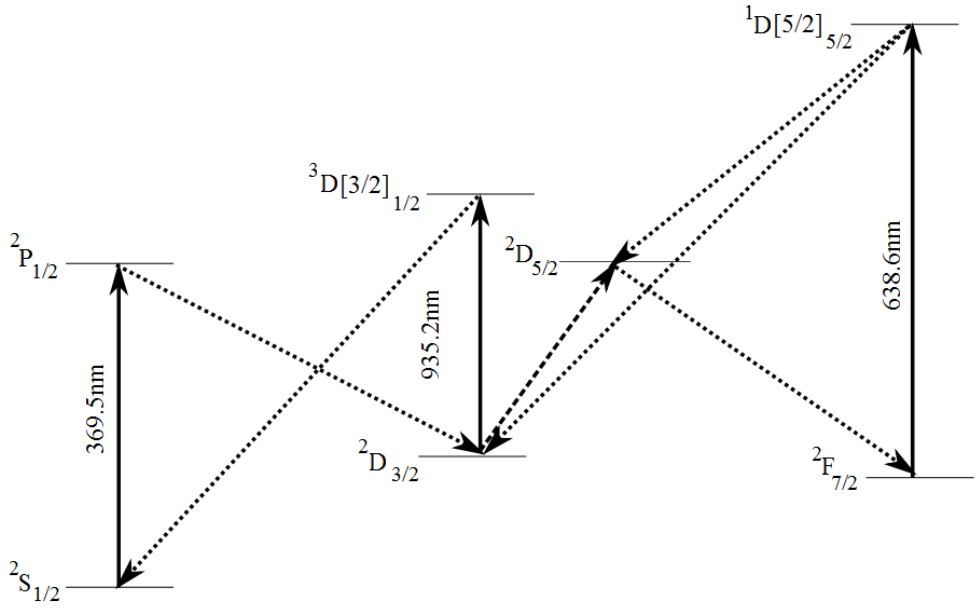

Figure 2.5: Diagram showing the energy levels in even Yb^+ ions. More precise wavelength data is shown in table 7.2.

around 6 years [43]. A collision of this type will remove the ion completely from the cooling cycle resulting in the ion heating, ceasing to fluoresce and, once hot enough, leaving the trapping field altogether. This can be avoided by using 638 nm light to depopulate the F state and allow decay back into the 369 nm and 935 nm cooling cycle. For the 171 isotope either two 638 nm lasers at different wavelengths are required or, as in this work, a single laser can be switched between the two wavelengths.

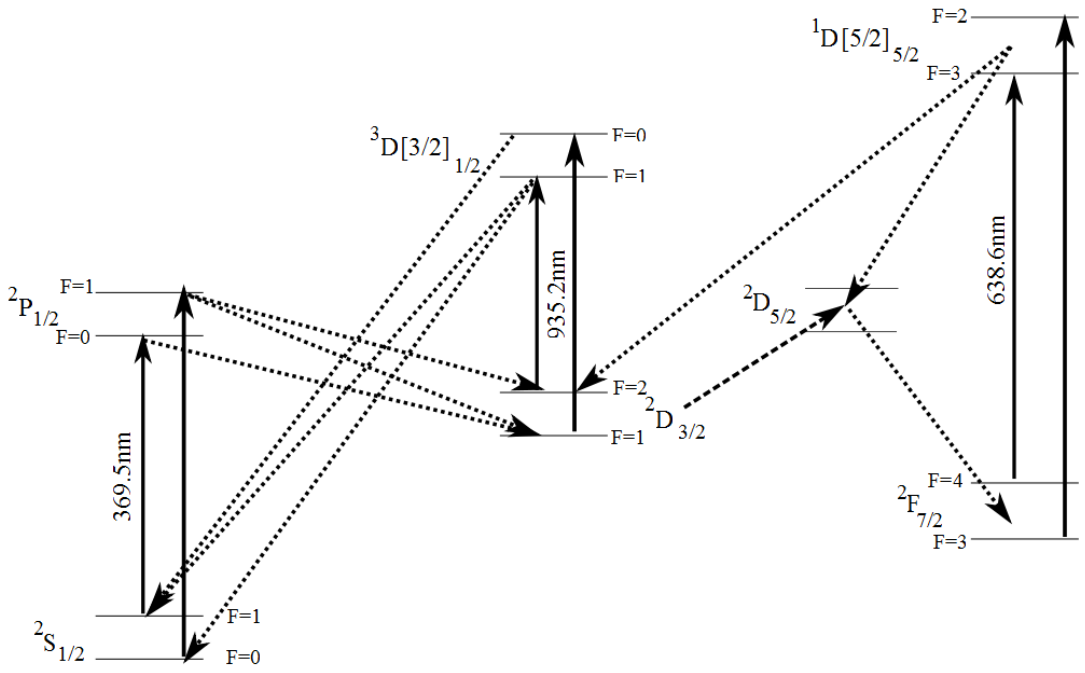

Figure 2.6: Diagram showing the energy levels in a 171 Yb^+ ion. Here the hyperfine splitting for the $^2S_{1/2}$, $^2P_{1/2}$, $^2D_{3/2}$ and $^3D\,[3/2]_{1/2}$ are 12.6 GHz, 2.1 GHz, 0.86 GHz and 2.20 GHz respectively. More precise wavelength data is shown in table 7.2.

The 171 isotope of Yb^+ possesses hyperfine doublets which are a result of the ion's spin half nucleus and are shown in figure 2.6. The ground state levels $^2S_{1/2}\,|F=0, m_F=0\rangle$ and $|F=1, m_F=0\rangle$ can be used to represent the $|0\rangle$ and $|1\rangle$ qubits respectively, for use in quantum information processing. Doppler cooling and fluorescence detection is carried out on the $^2S_{1/2}\,|F=1\rangle \leftrightarrow^2 P_{1/2}\,|F=0\rangle$ transition. It is possible for off-resonant coupling to occur during this process resulting in a population of the $^2S_{1/2}\,|F=0\rangle$ state. Selection rules dictate that this state can only be de-populated via the $^2S_{1/2}\,|F=0\rangle \leftrightarrow^2 P_{1/2}\,|F=1\rangle$ transition which is 14.7 GHz away from the $^2S_{1/2}\,|F=1\rangle \leftrightarrow^2 P_{1/2}\,|F=0\rangle$ transition due to the hyperfine splitting. As with the even isotopes the $^2P_{1/2}$ manifold can decay to

either the ${}^2D_{3/2}\,|F=1\rangle$ or ${}^2D_{3/2}\,|F=2\rangle$ states. Depopulation of these states is achieved using the two transitions of ${}^2D_{3/2}\,|F=1\rangle \leftrightarrow^3 D\,[3/2]_{1/2}\,|F=0\rangle$ and ${}^2D_{3/2}\,|F=2\rangle \leftrightarrow^3 D\,[3/2]_{1/2}\,|F=1\rangle$, which are 3.06 GHz apart due to the hyperfine splitting. Again, as with the even isotopes, collisions with background gas particles can cause the ion to be transferred to the ${}^2F_{7/2}$ manifold. This is de-populated via transitions at 638.610 nm and 638.616 nm used to excite the ion into the ${}^1D\,[5/2]_{5/2}$ manifold from where it can decay back into the cooling cycle [44].

2.5 Ion fluorescence and Doppler cooling of trapped ions

Many experiments in the field of quantum information processing require the trapped ions to be well localised [17, 19, 45, 46, 47]. To achieve this localisation, cooling of the trapped ions is required. Doppler cooling provides a simple method to implement this and, although Doppler cooling alone may not leave the ion in the required motional state, it is often a pre-requisite for cooling techniques used to provide further localisation [48, 49].

The scattering rate of a two level atomic system is given by [50]

$$\gamma = \frac{s\frac{\Gamma}{2}}{1+s+\left(\frac{2\Delta}{\Gamma}\right)^2} \tag{2.13}$$

where Γ is the linewidth of the transition, s is the saturation parameter and Δ is the detuning of the laser from the transition frequency. As the ion possesses a velocity, $\bar{v}$, a Doppler shift, $\omega_D = k\bar{v}$, of the transition frequency occurs which affects the scattering rate of the ion, giving a new scattering rate of

$$\gamma_D = \frac{s\frac{\Gamma}{2}}{1+s+(\frac{2(\Delta-\omega_D)}{\Gamma})^2} \tag{2.14}$$

Photons have a momentum, $\hbar k$, and so an ion absorbing a photon recoils from the photon source with equal momentum. This results in the ion feeling a force given by

$$F_D = \hbar k \gamma_D \tag{2.15}$$

Assuming a Doppler shift which is small in comparison to the detuning ($\Delta > \omega_D$) it is possible to Taylor expand equation 2.15 as

$$F_D = F_0 + \frac{dF_D}{d\Delta}\cdot k\bar{v} + \ldots \tag{2.16}$$

Setting $F_0 = 0$ (as we are only interested in the change in energy and not the initial conditions) the change in energy due to Doppler cooling can be expressed as

$$\frac{dE}{dt}_{cool} \approx \frac{2\hbar k^2 s\bar{v}^2\Delta}{\Gamma\left(1+s+\left(\frac{2\Delta}{\Gamma}\right)^2\right)^2} \tag{2.17}$$

If the frequency of the cooling laser is red detuned from the ion's resonant transition frequency then the Doppler shift will act to cause the ion to scatter more photons when its velocity, $\bar{v}$, is in the direction of the photon source. This means that the laser applies a force on the ion in the direction of the laser wave vector. A force is also felt by the ion when a photon is emitted, returning it to its ground state, but as these photons are scattered randomly in all directions the net force from these events will average to zero. This means that, averaged over many photon scattering events, the net force felt by the ion will be that given by equation 2.15. The energy associated with each of these spontaneous scatter events is given by

$$E = \frac{\left(\hbar\bar{k}\right)^2}{2m} \tag{2.18}$$

where m is the mass of the ion. This energy can then be combined with the scatter rate in equation 2.13 and the knowledge that both a photon absorption and emission event lead to heating, to give the change in energy due to heating as

$$\frac{dE}{dt}_{heat} = \frac{(\hbar k)^2 s\Gamma}{2m\left(1+s+\left(\frac{2\Delta}{\Gamma}\right)^2\right)} \tag{2.19}$$

The limit of Doppler cooling is then found by equating the cooling and heating rates in equations 2.17 and 2.19 yielding a minimum ion velocity in the Doppler limit of

$$v^2 = \frac{\hbar\Gamma^2}{8m\Delta}\left(1+s+\left(\frac{2\Delta}{\Gamma}\right)^2\right) \tag{2.20}$$

The temperature of the ion can be related to its velocity via $m\bar{v}^2/2 = k_B T/2$ yielding

$$T = \frac{m\bar{v}^2}{k_B} \tag{2.21}$$

which, in the case when $s \ll 1$, gives a Doppler cooling temperature of

$$T = \frac{\hbar\Gamma^2}{8\Delta k_B}\left(1+\left(\frac{2\Delta}{\Gamma}\right)^2\right) \tag{2.22}$$

A minimum Doppler cooling temperature, T_D, is achieved when the detuning is set to $\Delta = \Gamma/2$, resulting in

$$T = \frac{\hbar\Gamma}{2k_B} \tag{2.23}$$

This Doppler limit, T_D, can be expressed in terms of the ions secular frequency, ω_t, and the thermal motional state in which the ion resides $\bar{n}$ [50]

$$T_D = \hbar\omega_t \bar{n}_D \tag{2.24}$$

For a typical trapping secular frequency of $\omega_t \approx$1 MHz the minimal motional state Yb^+ ions can be cooled to is, therefore, $\bar{n}_D \approx 10$.

Chapter 3

Yb^+ ion trap experiment set up

3.1 Introduction

In this chapter the ultra high vacuum system used to house the ion trap will be introduced. This system has been specifically designed to cater for both surface and through chip traps with the additional ability of fast turnaround times when changing between different chip traps. The macroscopic trap fitted in the vacuum system used to initially trap and gain vital knowledge of Yb^+ ion wavelengths will be described. The optical apparatus used to combine and focus various lasers into the trapping region of the vacuum system will also be introduced and described along with the methods used to apply sidebands to the 935 nm and 369.5 nm lasers.

3.2 The ultra high vacuum system

A successful ion trap experiment requires the construction and operation of an ultra high vacuum (UHV) system. This is required in order to reduce the probability of collisions with other particles, which can cause the ions internal state to change and introduce decoherence. A severe enough collision is capable of ejecting an ion from the trapping potential. For these reasons it is desirable to design a vacuum system which is capable of achieving pressures of $\approx 10^{-12}$ Torr. At this pressure the mean free path length of the atoms and molecules is around 10^7 km resulting in ion lifetimes of hours to days. Another requirement for the vacuum system is the ability to accommodate both surface and through traps. This has been achieved with the use of a custom made chip bracket (shown in figure 3.1) designed to accommodate a commercially available chip carrier (Global Chip Material: PGA10047002).

The use of the chip bracket arrangement in figure 3.1 allows different micro fabricated

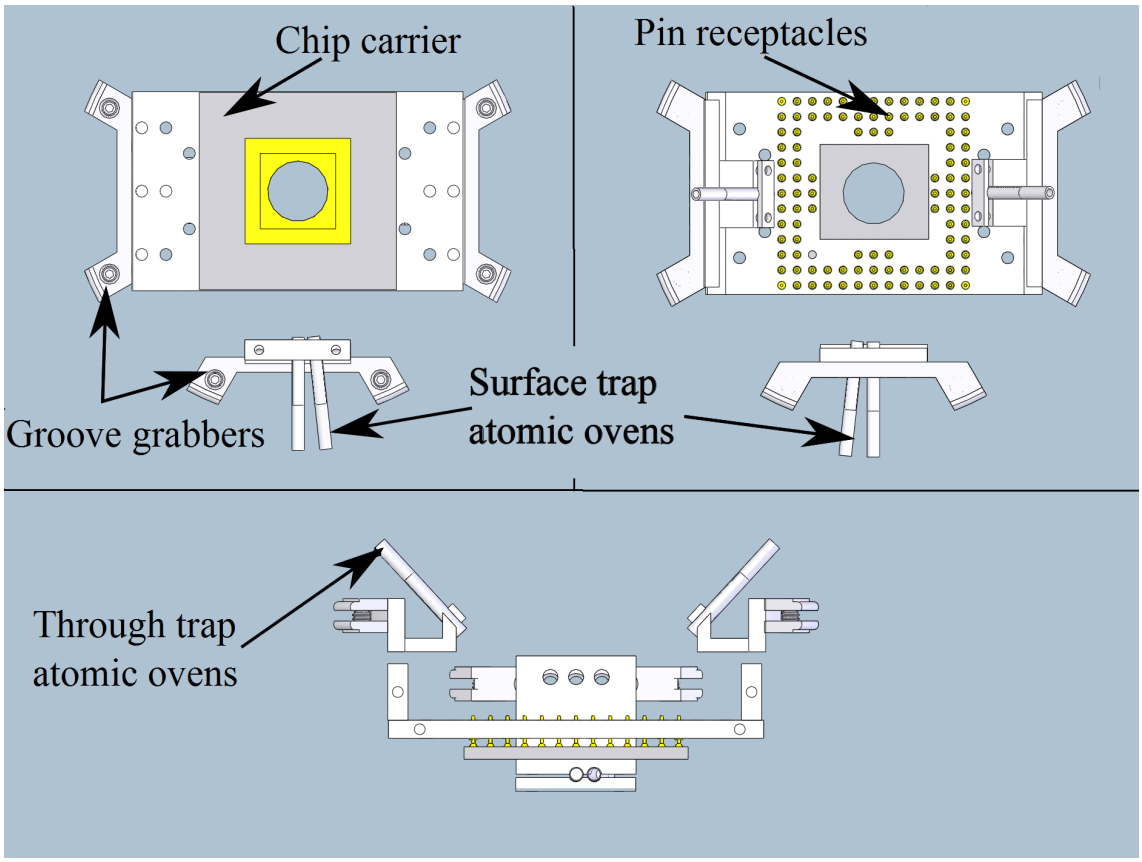

Figure 3.1: Diagram depicting the chip carrier, chip bracket and both surface and through trap atomic ovens. **Top left:** The chip carrier is shown containing a hole allowing for laser access for through traps. The chip bracket is shown along with the groove grabbers (Kimball Physics: MCF450-GG-CT02-A) used to mount the bracket onto the inside of the vacuum chamber hemisphere. Also visible are the atomic ovens used to supply an atomic flux for surface traps. **Top right:** The underside of the chip bracket is shown. Visible in this view are the pin receptacles from the chip carrier. These receptacles are used to supply voltages to bond pads on the chip carrier. Also visible are the atomic ovens used to produce an atomic flux for through traps. Again the surface trap atomic ovens are visible. **Bottom:** A side view shows the chip carriers pin receptacles penetrating the chip bracket. Also shown are the atomic ovens used to provide atomic flux for symmetric through type traps.

chip traps to be tested in UHV conditions with a short turnaround time (within two weeks). It provides 90 electrical connects for applying voltages to traps being tested. Eighty-eight of these connects are wired to two 50 pin feedthroughs which provide the ability to controllably apply static voltages directly to each chip pin. The remaining two connects are used to apply an RF voltage to the chip. This is done via connection to a power feedthrough (Kurt J. Lesker: EFT0521052) by bare copper wires insulated with ceramic beads. Initially Kapton insulated wires were used but were found to outgas and electrically short when high RF voltages were applied (in the range of 500-1000 V).

The chip bracket is encased within a Magdeburg hemisphere attached to an octagon (Kimball Physics: MCF450-MH10204/8-A and MCF450-SO20008-C respectively) as shown in figure 3.2. The combination of the hemisphere and octagon provides simple optical laser access to interact with trapped ions. Access for surface traps are provided by six $1\frac{1}{3}$" fused quartz silica windows in the octagon whilst access for through traps are provided by two $1\frac{1}{3}$" fused quartz silica windows in the hemisphere. All eight of these windows are anti-reflection (AR) coated to maximise the amount of laser power that reaches the trapping region. The AR coatings were specified to transmit 95% of incident light at all the wavelengths used (369 nm, 399 nm, 935 nm and 638 nm).

To provide an atomic source, four ovens are mounted onto the chip bracket, as seen in figure 3.1. These consist of ≈ 0.8 mm diameter stainless steel tubes connected to an external current source via an electrical power feedthrough (Kurt J. Lesker: EFT0265063). When ohmically heated by the current source, they provide a stream of divergent atomic beams aimed at the centre of the chip bracket. Two of the ovens provide atoms for a surface trap geometry whilst the other two provide atoms for a through trap. It is important to know the angle between the atomic ovens and the path of the ionising lasers (the 399 nm laser) as the wavelength at which the lasers will be resonant with the oven atoms is a function of the intersecting angle [36]. The change in the frequency, Δf, from the Doppler-free transition frequency, f, is given by

$$\Delta f = \frac{fv}{c}\cos\theta \tag{3.1}$$

where v is the mean velocity of the atoms exciting the atomic ovens, θ is the angle between the atomic motion and the intersecting laser beam and c is the speed of light. Using equation 3.1 along with the knowledge of the angle between the atomic ovens and the laser beam path it is possible to predict the shift in frequency from the Doppler-free transition frequency required to ionise the ejected atoms for the particular system set up.

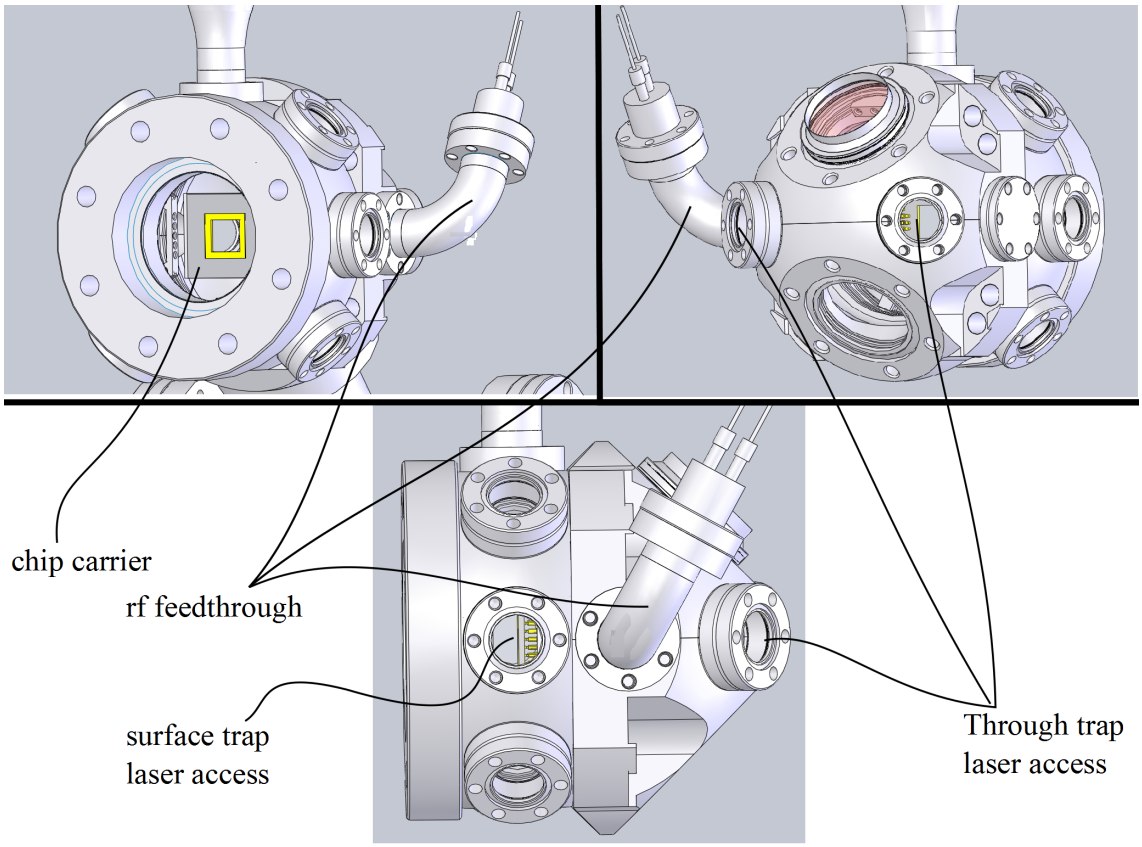

Figure 3.2: **Top Left:** Vacuum system hemisphere with the chip carrier visible through the main window of the octagon. **Top right:** The rear side of the hemisphere is shown. Here the laser beam entrance windows can be seen which enable laser access through the centre of the chip carrier for through traps. **Bottom:** A side view of the hemisphere and octagon with the octagon beam entrant windows visible for access to surface traps. Visible in all three views is the rf feedthrough used to apply radio frequency voltages to the trap electrodes via the chip carrier.

In the design used in this thesis the angle θ was $\approx 70^{\circ}$ which resulted in the wavelength of the 399 nm laser shifting by ≈ 220 MHz from the Doppler-free transition frequency for the particular isotope required for ionisation.

Before the vacuum system is assembled the individual stainless steel parts must be cleaned and baked. This is done to remove any dirt on the parts which may have accumulated during their transportation and storage. The parts are baked for a period of one week at a temperature of 200 °C and then cleaned again after this baking. The cleaning is carried out by immersing the parts in acetone (with the exception of the viewports) and placing them in an ultra-sonic bath, after which they are rinsed in methanol to remove any of the acetone residue left from the bathing. The viewports, however, must not be cleaned in this manner as acetone was found to degrade the anti reflection coating. Instead the viewports must be cleaned by rinsing them in isopropanol only. It is advisable to use this method of cleaning on any optical part with an anti reflection coating unless specifically instructed by the manufacturer.

Once the vacuum system has been assembled the ion trap should be degassed. This is done by pumping the system down to around 10^{-6} mbar using a roughing pump and then attaching a quarter wave helical resonator (described in chapter 5) to the rf feedthrough shown in figure 3.2. A voltage is then applied to the trap electrodes and slowly increased up to the desired operating range whilst the pressure of the system is closely observed, as a sudden increase in pressure could indicate a blown connection to the trap or electrical short. It is advisable to measure the capacitance and resistance of the trap before and after this procedure to help diagnose any electrical shorts that may have occurred. Carrying out this procedure allows for any sharp points or edges present on the trap electrodes to be smoothed and rounded.

3.2.1 Vacuum system baking and oven

After the degassing of the ion trap has been carried out and the electrical connections to the trap have been verified the vacuum system is ready to be baked and pumped down to a pressure of around 10^{-12} Torr. To reach this pressure the vacuum system must be baked at around 200 °C for a period of about two weeks. This ensures that all the water and other impurities present in the vacuum system are evaporated and pumped out of the system. If this is not carried out significant out-gassing can occur which reduces the final vacuum pressure achievable leading to reduced ion lifetimes due to an increased number of collisions with background gas particles.

The oven used to bake the system was an in-house built fan assisted system measuring 1 m by 1 m by 1.5 m and heated by eight 650 W ceramic elements (RS: FTE 650W 230V), as shown in figures 3.3 and 3.4. The heating elements are mounted on four aluminium pillars located in each corner of the oven (two per pillar) and are visible in figure 3.5. The oven walls, ceiling and door were constructed out of rockwool ($\approx$ 4 cm in thickness) sandwiched between a $\approx$ 1 mm aluminium plate (outer side) and a $\approx$ 1 mm stainless steel plate (inner side), a cut-through of which is shown in figure 3.3. Stainless steel was used on the inner side of the oven as it deforms less under heating compared with aluminium, and aluminium was used outside as it reduces the overall weight of the oven walls. Additional $\approx$ 3 mm thick aluminium edging was used to provide additional strength to the structure. The floor of the oven is constructed out of $\approx$ 1.5 cm superlux heat-proof board with a $\approx$ 1 mm thick aluminium cover.

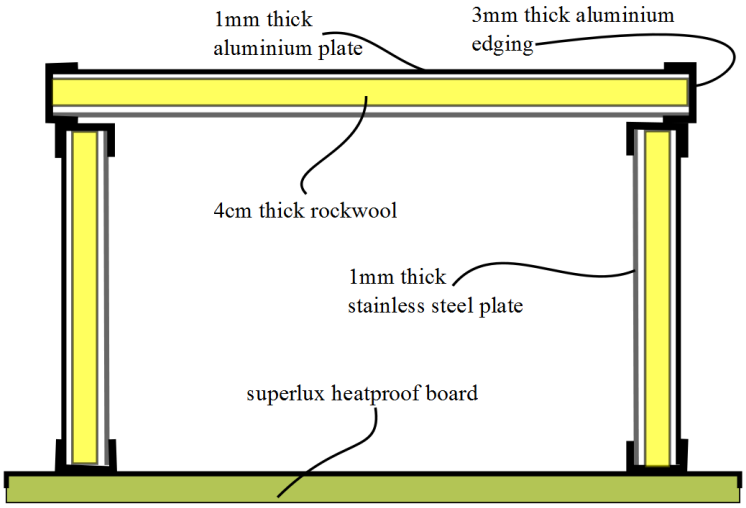

Figure 3.3: Diagram showing a cut-through of the oven wall, ceiling and floor. This consists of aluminium and stainless steel plates sandwiching a sheet of $\approx$ 4 cm rockwool.

In order to reach the baking temperature of 200 °C the temperature of the oven must be ramped at a maximum of 15 °C an hour to make sure that any expansion of the vacuum system and view ports does not cause any damage. The temperature ramp is controlled by a temperature controller (Barber Colman: 7EC) and solid state relay (Crydom: D53TP25D) which monitor the oven temperature via a type K thermocouple, placed centrally in the oven. They then act to alter the duty cycle of the current supplied to the heating elements in order to increase or decrease the oven's temperature.

Whilst the fully assembled vacuum system is being baked an external roughing pump is used to maintain the pressure at around 10^{-6} mbar until the oven temperature reaches

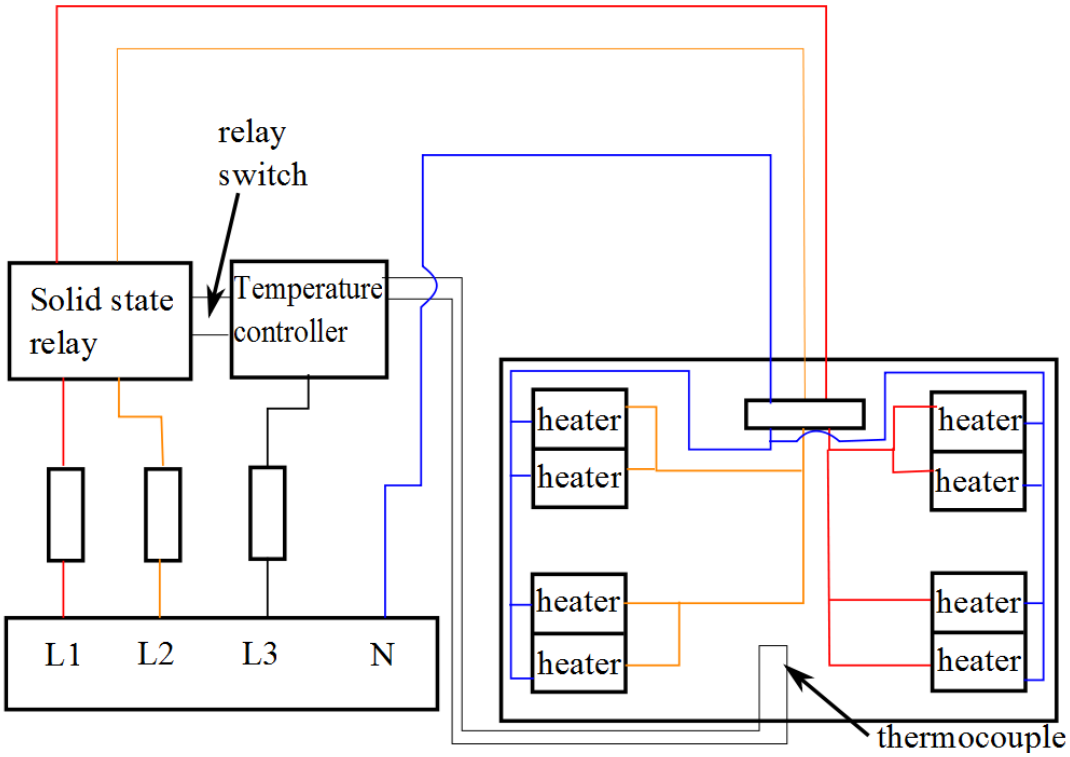

Figure 3.4: Diagram showing the wiring used to control the temperature of the oven. A three phase power line is used with live one and two (L1 and L2) used to power the heating elements and live three (L3) used to power the temperature controller. The neutral line (N) is also shown and is common to all the heating elements.

200 °C. At this point the roughing pump is switched off and an external ion pump is used to reduce the pressure further. After a few days this external ion pump is switched off and the two external pumps are disconnected from the system with the pressure maintained by the internal ion pump shown in figure 3.5. Once the baking is completed, the system is removed from the oven and placed on the optical table where a titanium sublimation pump (TSP) is used to reduce the pressure from 10^{-10} mbar to 10^{-12} mbar. This is done by running the TSP for around one minute every two hours for a period of two days at a current of 47 A.

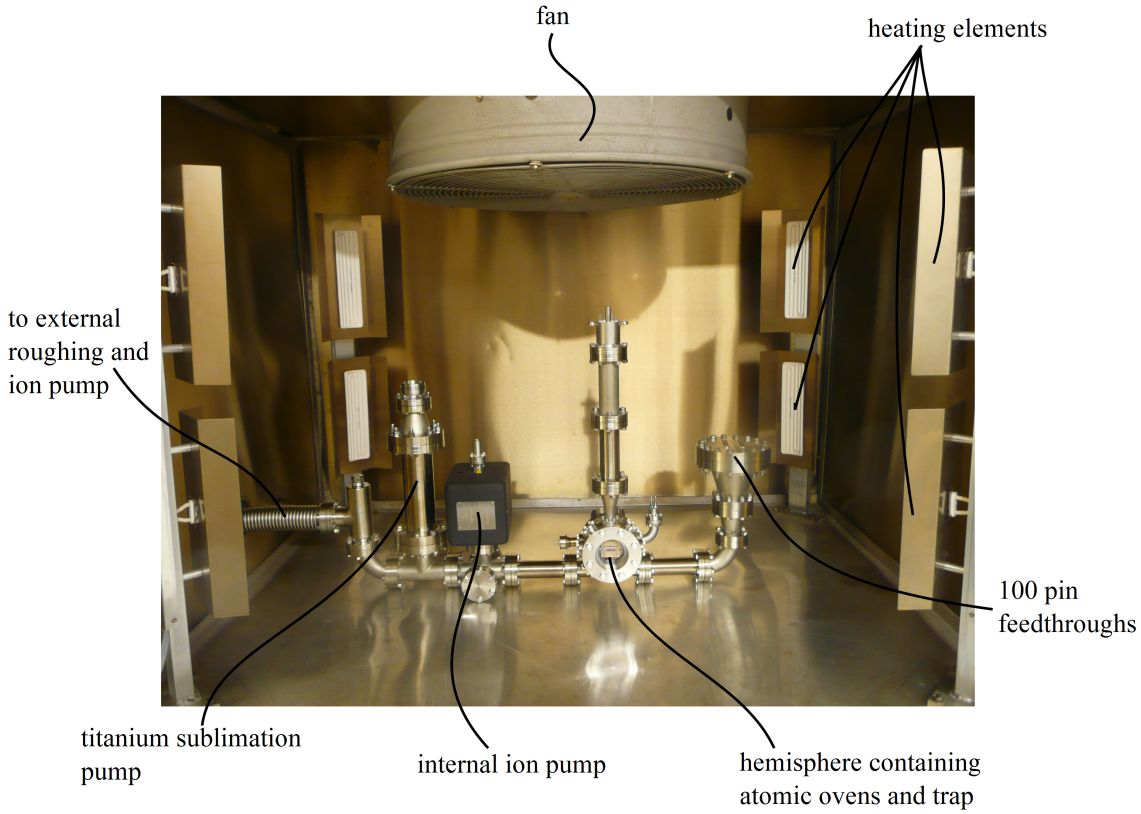

Figure 3.5: Picture of the entire vacuum system housed inside the in house built oven. Shown are the internal ion pump and the titanium sublimation pump, the hemisphere and octagon containing the chip carrier and the 100 pin feedthrough used to apply static voltages to the trap electrodes. Also shown is the oven fan and the ceramic heating elements.

3.3 Macroscopic linear Paul trap design

A macroscopic linear Paul trap was designed and built to be compatible with the chip bracket shown in figure 3.1. An initial macroscopic trap was chosen over an initial mi-

crofabricated trap due its ability to provide deeper trapping potentials (up to $\approx$ 10 eV compared with up to $\approx$ 1 eV), and robustness against static and RF voltage breakdown. This trap was also designed to be capable of trapping long chains of ions by keeping the residual RF ponderomotive potential along the Z-axis to $\approx$ 0.4% of the radial ponderomotive potential.

The basic structure of the trap is shown in figures 3.6 and 3.7 and consists of four blade shaped electrodes. Two of these electrodes run the entire axial length of the trap and are connected to the RF source. The other two are segmented into three pieces and are connected to external static voltage supplies in order to provide axial confinement fields and the ability to rotate the principle axes of the resulting static voltage and RF ponderomotive potential. The blades are coated with a 5 μm layer of gold to increase the surface smoothness. Additionally, two wire electrodes were placed between the blades to provide additional static voltage fields to compensate for any stray fields present that perturb the trapping field increasing the ions micromotion.

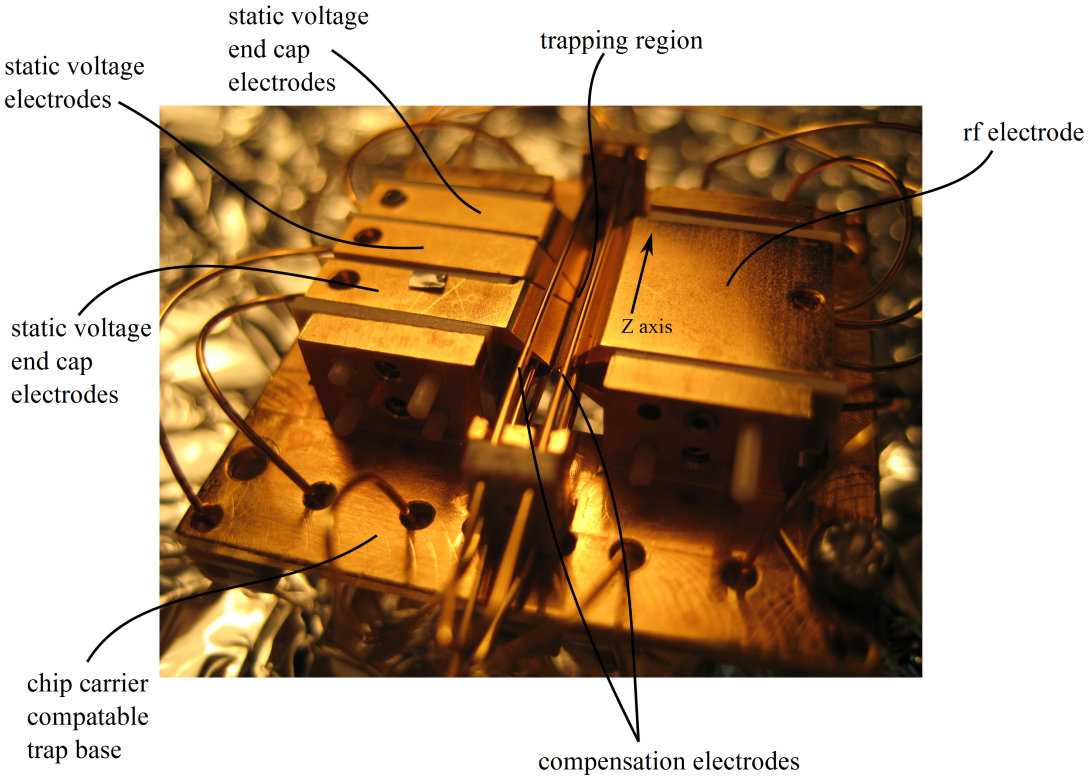

Figure 3.6: Picture showing the macroscopic linear Paul trap. The top level static electrodes and rf electrode are visible whilst the bottom layer are hidden below the upper layer. The Z axis of the trap is shown with the X and Y axis being perpendicular to this and each other.

The electric field produced by the trap structure was modelled using a boundary element method (BEM) in CPO (Charged Particle Optics [1]) to provided basis functions [51] for each individual electrode. These basis functions can then be used to determine the trap's secular frequency, depth and centre when any set of arbitrary voltages are applied to the electrodes. Initially the most important piece of information to be obtained from the simulations is the trap centre, allowing lasers to be correctly aligned and focused to the area in which the ion will be trapped and cooled. Additionally one can estimate the trap depth and the applied rf voltage by using the static voltages applied to the trap as inputs into the simulation and varying the rf voltage so the radial secular frequencies match the experimentally measured values. As the trapping potential along the Z axis is only given by the static voltages (as the residual rf ponderomotive potential along this axis is $\approx 0.4\%$) the Z secular frequency will be correct given only the static voltage inputs. Table 3.1 shows voltage configurations and trapping field specifications for a trap with a depth of 1.6 ± 0.2 eV and an rf voltage of 400 ± 20 V.

Table 3.1: Trapping voltage configurations and trapping field specifications.

rf voltage	400 ± 20 V
Static voltage 1	1.5 V
Static voltage 2	0 V
End 1	0 V
End 2	6.5 V
End 3	5.2 V
End 4	0 V
Comp 1	60.5 V
Comp 2	11.9 V
Secular frequency in X	1.27 ± 0.07 MHz
Secular frequency in Y	1.34 ± 0.07 MHz
Secular frequency in Z	154 ± 1 KHz
Depth	1.6 ± 0.2 eV

Laser access for the trap, depicted in figure 3.8, is provided through the back of the trap. This is accessible from the rear hemisphere windows shown in figure 3.2. This access is made possible by the cut away section in the base of the trap, shown in figure 3.6. The cut away section is large enough to allow the lasers to be directed onto all of the electrodes

[1] http://simion.com/cpo/

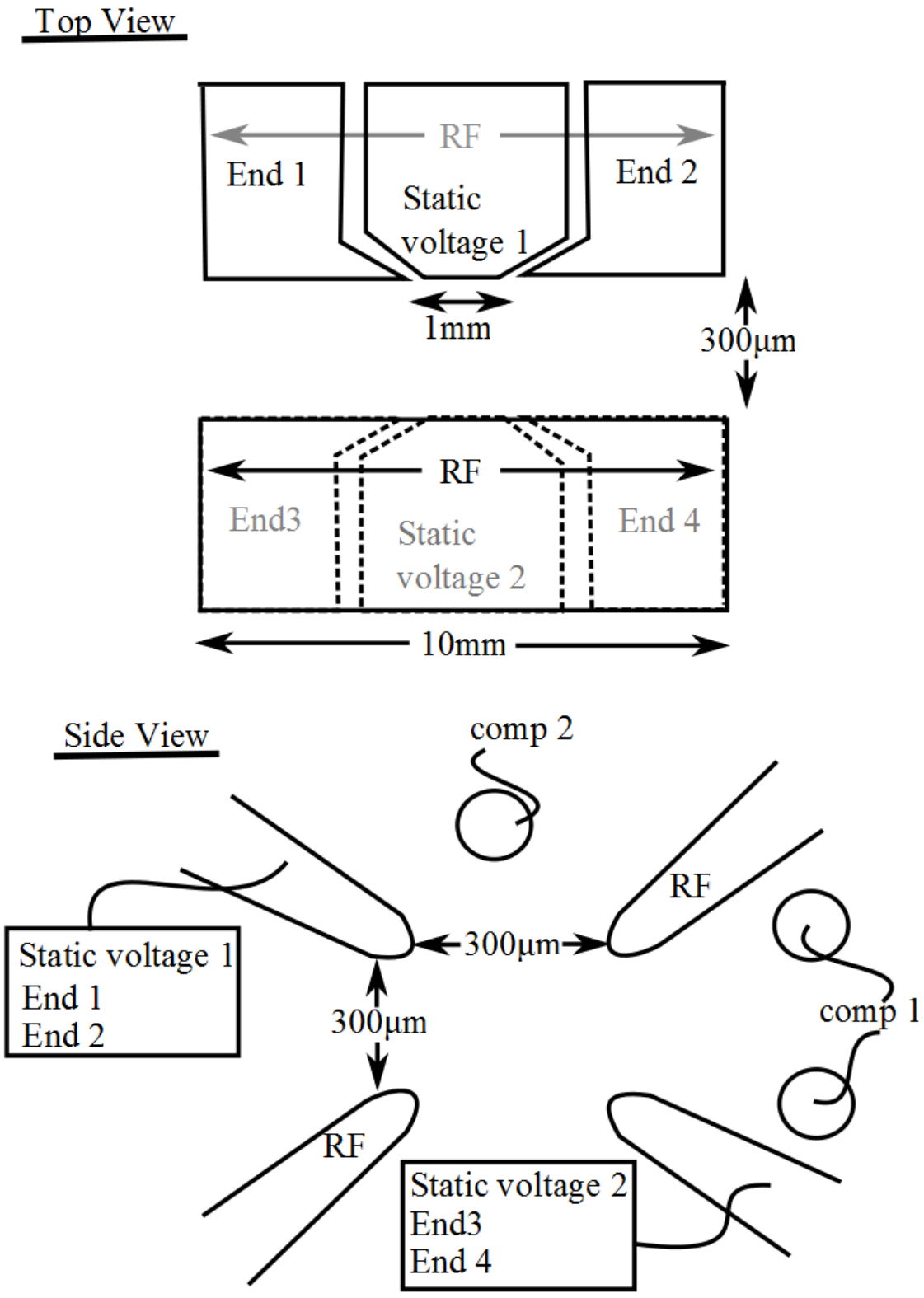

Figure 3.7: Diagram showing the macroscopic linear Paul trap. **Top view:** The four end cap electrodes (End 1 to 4) and both static voltage electrodes are shown. Dashed bordered electrodes are located below solid bordered electrodes. **Side view:** The location of the compensation electrodes (comp one and two) are shown. The electrode comp 1 consists of a single wire bent into a "U" shape to allow laser access through its centre.

in order to aid with their alignment. When aligned through the centre of the trap the laser beams are then able to exit the vacuum system via the front window, narrowly avoiding the imaging system.

3.4 Experimental laser set up

The lasers entering the vacuum system are focused to beam waists of between 50 μm and 100 μm by a series of telescoping and focusing optics placed in the beam paths of both the individual lasers and the combined laser paths. A schematic of the optical apparatus used to combine and focus the beams into the trapping region is shown in figure 3.8. The 369 nm and 935 nm beams are combined using a filter (Semrock: FF01-370/36-25) which transmits the 369 nm beam and reflects the 399 nm beam. The combined 399 nm and 369 nm beams are then combined with the 638 nm beam with a dichroic mirror. As shown in figure 3.8 telescoping lenses are used in some of the beam paths. The reason for this is that the telescopes can be used to increase the beam diameter before passing through the final focussing lens. By changing the beam diameter, the lasers beam waist at the focal point of the final lens can be altered. The relation of focused beam waist, w, to initial beam diameter, D, is the diffraction limited waist size given by:

$$w = \frac{2\lambda F}{\pi D} \tag{3.2}$$

where F is the focal length of the lens and λ the wavelength of light focused through the lens.

Additionally, the telescopes are used to control the divergence of the beams which pass through them altering their focal distance through the final focussing lens. This allows beams of different wavelengths to be focussed to the same point by altering the individual beam divergences. The combination of the beams is carried out after the individual laser's telescopes, enabling the divergence and diameter of each beam to be adjusted individually.

The individual laser wavelengths required for ionising Yb atoms and cooling Yb^+ ions can be determined from the ion's energy level diagram shown in figures 2.5 and 2.6. The wavelengths required are around 369 nm, 638 nm and 935 nm with a 399 nm laser required for ionisation. An additional laser at 780 nm was also used in this work to provide a stable reference for the other lasers, the process of which will be described in chapter 4. The light source at 369 nm was created by frequency doubling the light from a 739 nm laser diode (Toptica Photonics: TA-SHG). The remaining four light sources, the 399 nm (Sanyo: DL-4146-301, 20 mW), 638 nm (Sanyo: DL-6148-030, 40 mW), 780 nm (Sharp: GH0781JA2C,

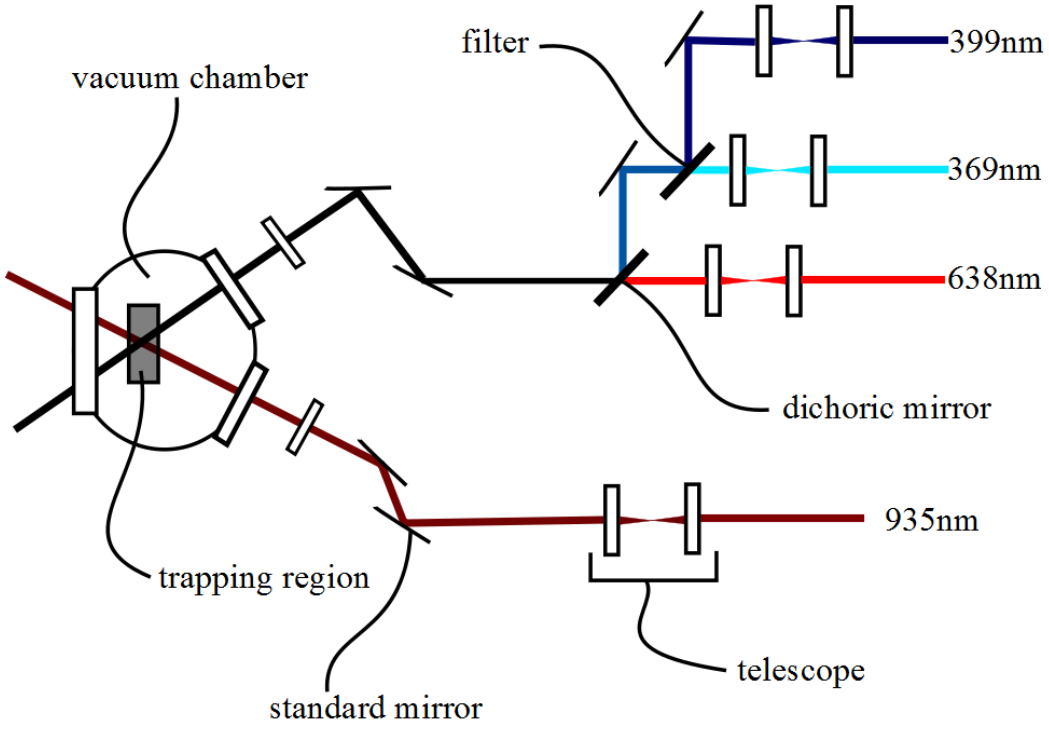

Figure 3.8: Schematic diagram showing the vacuum chamber and trapping region. Outside the laser paths are shown along with the optics used to focus and combine the lasers.

120 mW) and 935 nm (Roithner: RLT940-100GS, 100 mW) were built in-house using an external cavity diode laser (ECDL) design which utilises an external grating to provide optical feedback to the diodes. In each laser the grating and diode were placed in a Litrow [52] configuration as shown in figure 3.9 with the first order diffraction beam used to provide feedback to the diode and the zeroth order used as the output beam. The angle of the grating can be altered by the use of a piezo (PSt 150/4/5 bs) and is used to force the diode to emit at the desired frequency, λ, given by

$$\lambda = d \sin \theta \tag{3.3}$$

where d is the separation between the grooves on the diffraction grating and θ is the angle between the laser beam and the normal of the grating as shown in figure 3.9.

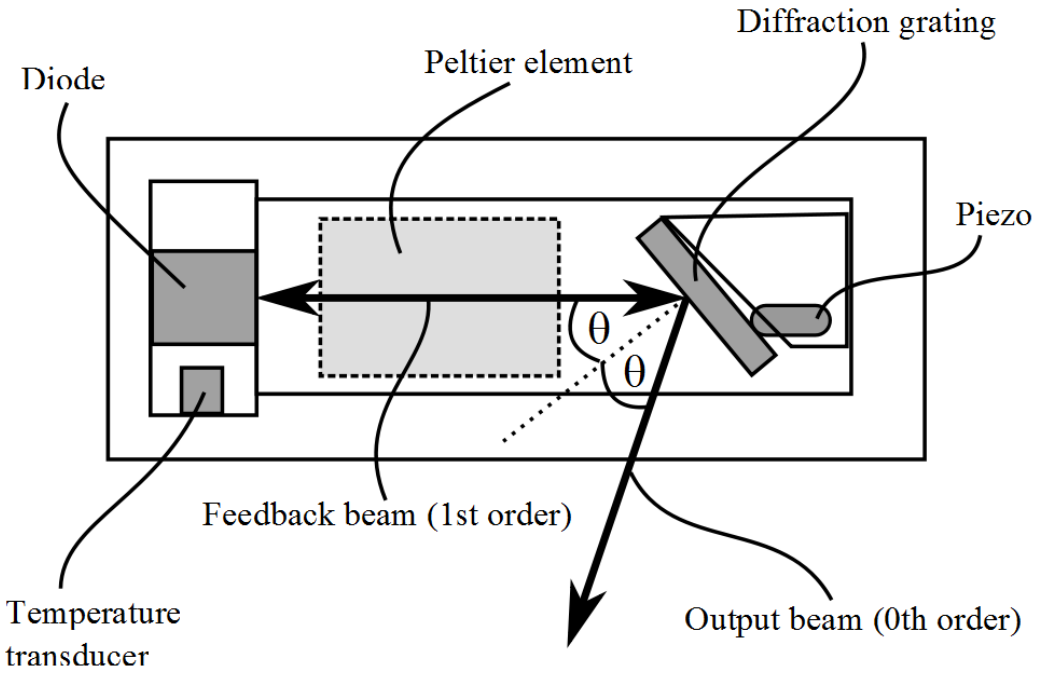

Figure 3.9: Drawing showing the general set up of an ECDL used to provide laser beams for the experiment.

As can be deduced from equation 3.3 the direction of the output beam is dependent on the wavelength the diode outputs. This can cause alignment issues when first adjusting the set up to provide the desired wavelength, but the problem is negligible once the laser is running at the desired wavelength and feedback is provided to maintain this. Feedback is also required to stabilise the temperature of the diode as the output wavelength is a

function of the temperature of the diode. This is done with the use of a temperature transducer (Analogue devices: AD592ANZ), a Peltier element (Global Component Sourcing: ETH-071-14-15-RS) and a temperature controller (Thorlabs: ITC 502). The temperature transducer and Peltier element are placed near to the diode with a good thermal contact to it. The temperature detected by the transducer can then be stabilised to the desired set point by the PID in the temperature controller to around 0.01 °C.

As described in chapter 2 side-bands need to be applied to the 935 nm and 369.5 nm lasers in order to access the hyperfine energy levels created by the non-integer spin of the $^{171}Yb^{+}$ isotope. The sidebands required on the 369.5 nm light are created by frequency doubling sidebands applied to the 739 nm laser light. The light emitted from the 739 nm diode is phase modulated at 7.35 GHz with an electro-optic modulator (New-Focus: 4851) and then passed through a doubling cavity, which is resonant with both the carrier and the modulated sidebands, producing 14.7 GHz sidebands on the 369.5 nm beam. For these experiments a doubling cavity with a free spectral range of 1.05 GHz was used (Toptica Photonics: TA-SHG). The sidebands required for the 935 nm laser light, on the other hand, are created simply by current modulation at 3.06 GHz via a bias-t (Mini Circuits: ZFBT-4R2G+).

Chapter 4

Laser locking using scanable Fabry-Pérot cavities

4.1 Introduction

In this chapter the laser locking scheme along with the equipment used to execute the scheme will be described. Locking the lasers described in chapter 2 is required initially to maintain their frequencies close to the resonant frequency of a particular transition. Drifting away from this resonant value will cause the fluorescence of the ion(s) to reduce (the exact amount of fluorescence reduction is dependent on the power broadening of the transition by the laser intensity at the ion). Additionally laser locking stops the 369 nm laser frequency becoming blue detuned from resonance and heating the ion out of the trapping field. In order to achieve this it is required to lock the lasers to within a few MHz over the time frame of a few hours.

4.2 Background and optical set up

The long term stability of the lasers used to trap Yb^+ ions (369 nm and 935 nm) is achieved using a method described by Zhao et al. and Seymour-Smith et al. [53, 54]. This method uses a Fabry-Pérot cavity to transfer the stability of a master reference laser to other lasers. A data acquisition card (DAQ) is used to scan the cavity length whilst simultaneously reading the spectra produced by the cavity. Each time the cavity is scanned the position of the fringes are measured relative to the stable reference laser's fringes. An error signal can then be produced to correct for the drift in the locked lasers.

The 369 nm laser light is created by frequency doubling 739 nm light from an ECDL

diode laser (Toptica: TA-SHG 36) and, so, the stability of the 739 nm light is passed onto the doubled light. 739 nm light was used in the locking scheme and not 369 nm light as it offers an easier wavelength to use both in terms of reflection coatings for mirrors and alignment (as the light is visible whereas 369 nm is not). The reference laser used in our experimental set-up is a 780 nm laser locked to a ^{87}Rb D_2 transition line with a stability of $\approx$ 1 MHz. To transfer this stability to the 935 nm and 369 nm lasers two separate Fabry-Pérot cavities were built from curved mirrors with reflectivities of 99.9% at the wavelengths required for use (739 nm, 780 nm and 935 nm). One cavity is designed to receive the 780 nm reference laser and the 935 nm laser and the other to receive the reference laser and the 739 nm laser. The beams are placed into the cavities forming a figure of eight pattern between the mirrors, giving a free-spectral range of $FSR = c/(4l)$ (where c is the speed of light). The free spectral range of the two cavities built and set up to accept 739 nm and 935 nm were $\approx$ 1 GHz and $\approx$ 750 MHz respectively. The cavity length, l, is scanned with a piezo (Piezomechanik: HPST 150/14-10/12 with thread adapter HAg) using a triangular waveform voltage obtaining a spectra of fringes related to the scanning voltage, as shown in figure 4.1. The frequency of this scan was set at 57$\pm$1 Hz and, so, any noise on the lasers with a frequency greater than this will not be compensated for. However, this frequency is sufficient to compensate for the long term drift (several hours) of the laser wavelengths required for initial trapping of ions. Using the fringes obtained from one scan of the cavity, two variables, a and b, can be obtained. These variables are the separation between a reference peak and a locked laser peak, a, and the distance between two of the reference peaks, b, and are shown in figure 4.1. A computer programme can then be used to calculate the ratio a/b for each scan of the cavity and produce an error signal which is used to adjust the angle of the locked lasers reflection grating (shown in figure 3.9), altering its wavelength and keeping the ratio constant. The wavelength of the locked laser can then be adjusted by changing the ratio a/b until the laser is at the desired operating wavelength. Additionally it is possible to scan the locked laser by scanning the ratio a/b in the computer programme. The reason for using the ratio a/b to produce an error signal to lock the lasers is that any changes in the free spectral range of the cavity is cancelled out in the ratio and, therefore, any changes are due to drifts in the two laser wavelengths. If the distance from a reference peak to a locked laser peak, a, was instead used this variable will change with a change in free spectral range as well as a drift in frequency. This would result in the feedback trying to compensate for both drifts instead of just frequency drifts.

In figure 4.1 the variable a is shown as the distance between a 780 nm reference peak and a locked laser peak in the next free spectral range. It is possible to use the locked laser peak in the same free spectral range instead to calculate a value of a but, in this case, the error on a will be greater. This is because the error on locating the position of a peak is fixed and so increasing the value of a reduces the percentage error on a and will, therefore, produce a more accurate error signal. Alternatively, a could be calculated using a peak in a much further away free spectral range than shown in figure 4.1, but one must ensure that it is not located too near the edge of a piezo scan as the piezo extension may no longer be linear with the applied voltage at this point. In practice, however, little, if any, difference was noted to the laser stability when calculating a using peaks in different free spectral ranges.

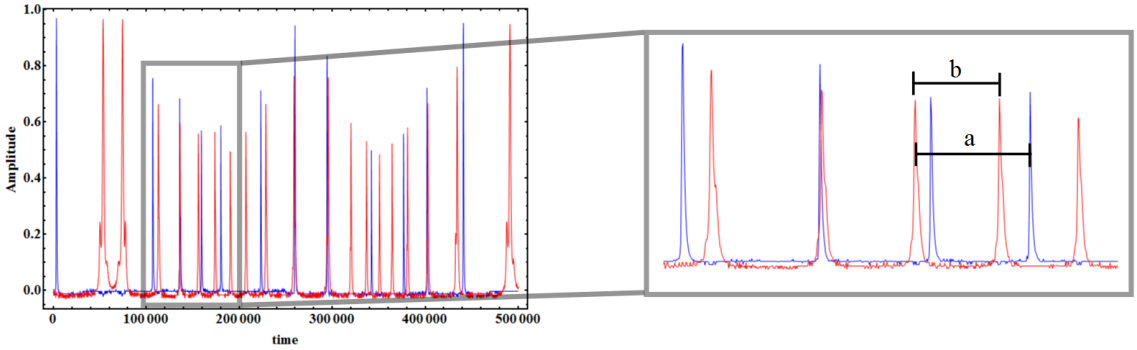

Figure 4.1: Plot of the output from a cavity showing the variables a (distance from a reference peak (Red) to a locked laser peak (Blue)) and b (the distance between two reference peaks) shown in the inset.

Figure 4.2 shows the optical set-up used to transfer the stability of the 780 nm laser to the 935 nm and 739 nm lasers via the two scanning cavities. The lasers are combined using polarising beam splitters allowing light from two lasers to be simultaneously coupled into a cavity at a time. Polarising beam splitters can then be used to separate the individual lasers output from the cavity in order to be read into a DAQ via individual photodiodes. This locking scheme will allow both laser signals to be detected on one photodiode, however, due to the different powers in the three lasers and the photodiodes efficiency varying over the wavelength range it is experimentally easier to use a photodiode per laser. This allows each signal to be individually optimised by adjusting the gain applied to each signal. Figure 4.3 shows a photograph of the optical set up for transferring the stability of the 780 nm laser to the 739 nm laser. Shown is the cavity used along with the photodiodes, beam splitters and a half wave plate is present to rotate the polarisation of the 739 nm

light. By adjusting the beam's polarisation the beam can be split between the cavity and the wavemeter fibre coupler used to monitor the laser's wavelength.

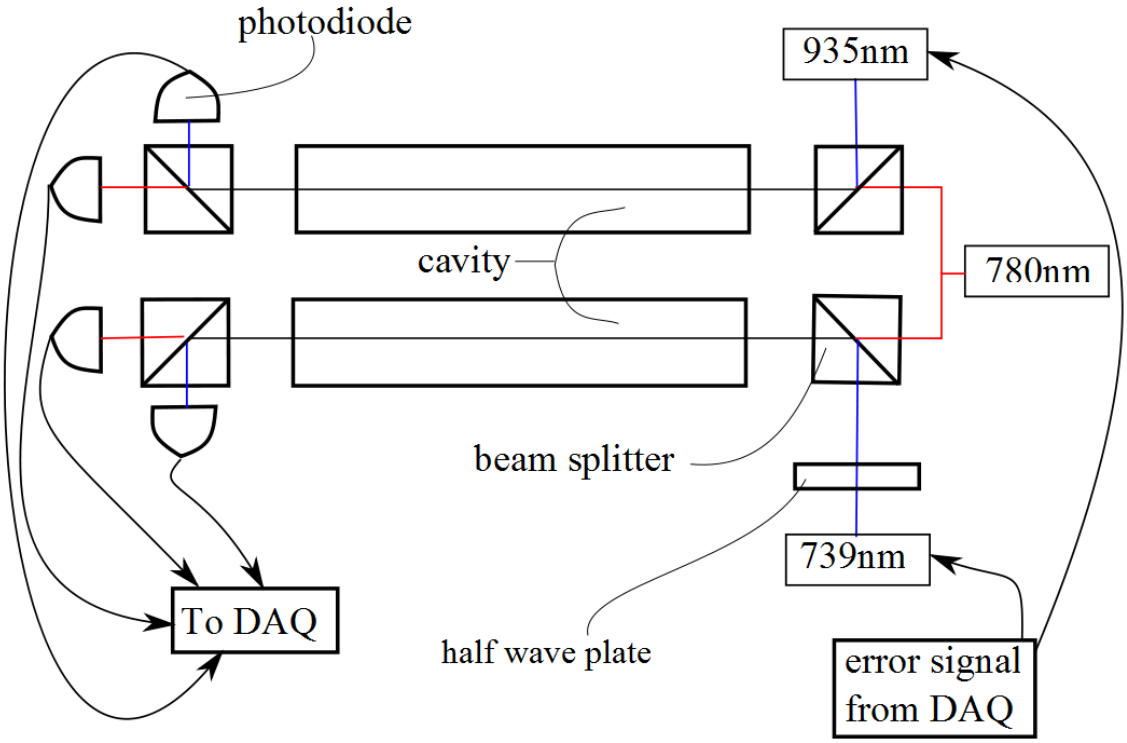

Figure 4.2: Diagram showing the optical set-up used to transfer the stability of the 780 nm reference laser to the 935 nm and 739 nm lasers via two scanning cavities. The outputs of the cavities are read into a DAQ via photodiodes and an error signal sent to the individual lasers depending on the signal detected by the photodiodes.

The cavities are used without being thermally isolated from the environment and so are subject to thermal drift in their length. This length change leads to the voltage driving the piezo required to produce a reference peak at a specific position to change. In other words the peaks, as seen displayed in figure 4.1, drift. This becomes a problem if one of the peaks used to calculate the variables a and b drift off of the display. This is solved by extending the process outlined by Zhao et al. [53] to include "thermal feedback" which compensates for this drift. This feedback adjusts the dc offset of the scanning voltage in order to keep the positions of the peaks from the reference laser constant in the display.

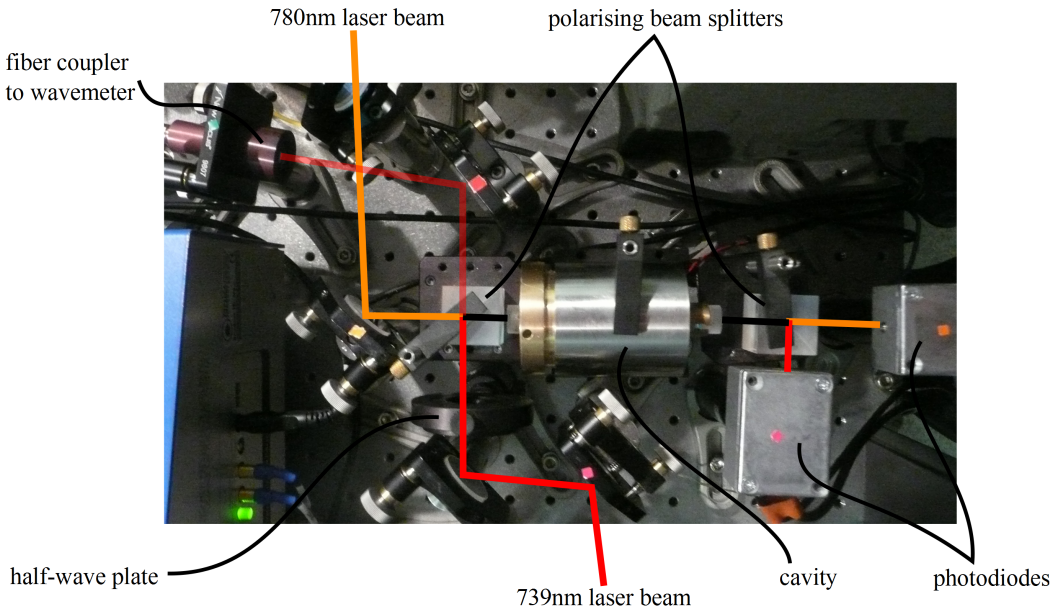

Figure 4.3: Photograph of the cavity used to transfer the stability of the 780 nm reference laser to the 739 nm laser. Shown are the polarising beam splitters, cavity and photodiodes. The half-wave plate present in the 739 nm beam is used to split the beam between the wavemeter fibre coupler (allowing wavelength measurements) and the cavity.

4.3 Locking electronics

In order to drive the cavities, read in photodiode signals and trigger the computer programme used to create the error signals with the experimental set up shown in figure 4.2 some additional electronics is required. A square wave (57±1 Hz and 12.8±0.3 V) is produced by a signal generator (GW Instek: GFG-8015G) which is used as a trigger pulse for the locking program. For the cavities to scan synchronously with the computer programme reading the photodiode signals, they must be driven with signals of the same frequency and phase as the programme's trigger pulse. The simplest way of achieving this is to use the same signal, however, to produce sets of evenly spaced output peaks, as shown in figure 4.1, a triangle wave has to be used to drive the cavity piezos. This is because the extension of the piezo is linear with the voltage applied to it. An integrating amplifier is used to transform the square wave used to trigger the computer program into a triangle wave of the same frequency and phase. This can be done for any number of cavities giving the design flexibility in how many cavities are used. Figure 4.4 shows the layout of the electronics used to produce the signals used to trigger the computer program and scan the cavities simultaneously. Figure 4.5 shows a more detailed circuit diagram

showing the components used to make the summing and integrating amplifiers.

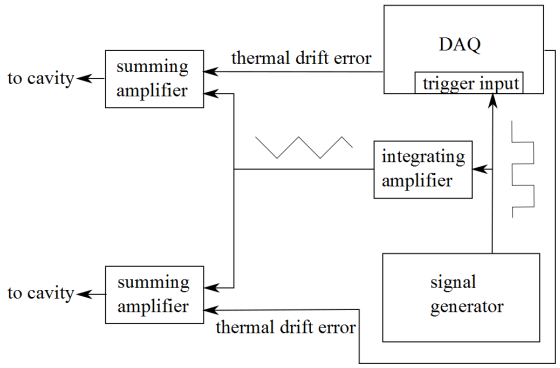

Figure 4.4: Diagram showing the drive signal used to simultaneously drive the cavities and trigger the Labview program.

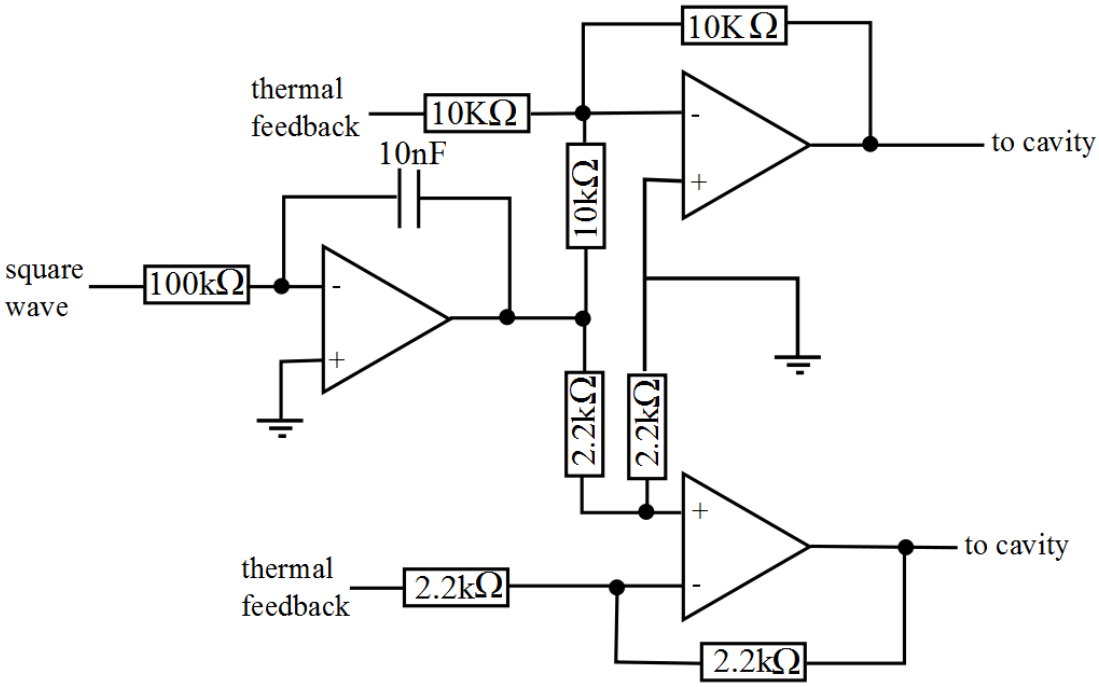

Figure 4.5: Diagram showing the circuit diagram of the two summing amplifiers and the integrating amplifier used to convert the square wave trigger signal into a triangle wave. The operational amplifier used in all the circuits is the LF411 and is powered with ±15 V.

It was found that simply scanning the cavity with a triangle wave resulted in a slow drift of the cavity output peaks over a period of time. This becomes a problem when

locking the lasers over a long period of time (over around 15 minutes) as the drift in peak position is enough to cause the locking scheme to fail. The movement of the peaks was thought to be caused by thermal drift in the cavity (length changes due to temperature) and so additional electronics and feedback was used to stabilise this. To do this, the time a specific peak occurs with respect to the start of the cavity scan is monitored and feedback produced to keep this time constant. The error signal produced was then added to the triangular driving signal via a summing amplifier, resulting in a dc offset to the driving signal. This offset acts to increase or decrease the length of the cavity, opposing the length change in the cavity caused by temperature drift. By doing this the peaks were kept stable and the lasers could be locked for periods of several hours.

4.4 The Locking program

A LabVIEW [1] programme was written to process the cavity signals detected by the photodiodes and produce the required error signals to be supplied to the laser diodes. The programme was deployed and run on a PC using a LabVIEW real-time operating system with the photodiode signals and trigger pulse read into the programme using a PCI card (National Instruments: PCI-6143 S series). The error signals produced by the programme are output using another PCI card (National Instruments: PCI-6722).

[1] http://www.ni.com/labview/

Figure 4.6: Screen shot of the locking programme's front panel. Highlighted in the yellow boxes are the cavity scan display and locking controls for transferring the stability of the 780 nm reference laser to the 739 nm laser. Highlighted in the red boxes are the cavity scan display and locking controls for transferring the stability of the 780 nm laser to the 935 nm laser.

Figure 4.6 shows the front panel of the locking programme. As two cavities are used to lock the 935 nm laser and the 369 nm laser there is a set of controls relating to each of the two cavities. The controls for the cavity locking the 739 nm laser (and thus the 369 nm laser) are highlighted in the yellow boxes, and the controls for the cavity locking the 935 nm laser are highlighted in the red boxes. In order for the locking programme to work successfully the 780 nm laser should be locked to the ^{87}Rb D_2 absorption line with a stability of ≈ 1 MHz.

4.4.1 Detecting peaks

Figure 4.7 shows an enlarged view of the cavity signals that are detected by the locking programme. In order for the programme to determine what is a peak and what is not, a peak detection system is used. This defines a peak as signal which is below a certain threshold and above a certain width. The controls for this detection system are shown in figure 4.8. To set up the peak detection correctly the following steps should be followed:

- The peak threshold for each laser signal should be set to a value below the noise of the signal but above the top of the smallest peak. It is preferable to set these values as close to the noise level as possible (as shown in figure 4.7).
- The dials controlling the minimum peak width should now be turned up slowly until the number of peaks detected is equal to the number of peaks displayed in the cavity scan display.
- If the number of peaks detected differs from the number of peaks shown in the cavity display then the peak width should be adjusted. If there is still a problem, the peak threshold should be reduced/increased and the peak width adjusted again.
- The peak threshold and width should be adjusted until the number of peaks detected equals the number on the display and does not vary randomly.

4.4.2 Thermally locking the cavities

Once the peak detection has been set, the thermal drift of the cavities must be compensated to allow laser locking over the course of several hours. Figure 4.9 shows an enlarged view of the controls which produce an error signal which is fed to cavities to compensate for any thermal drift. To provide thermal feedback for the cavities the following steps should be taken:

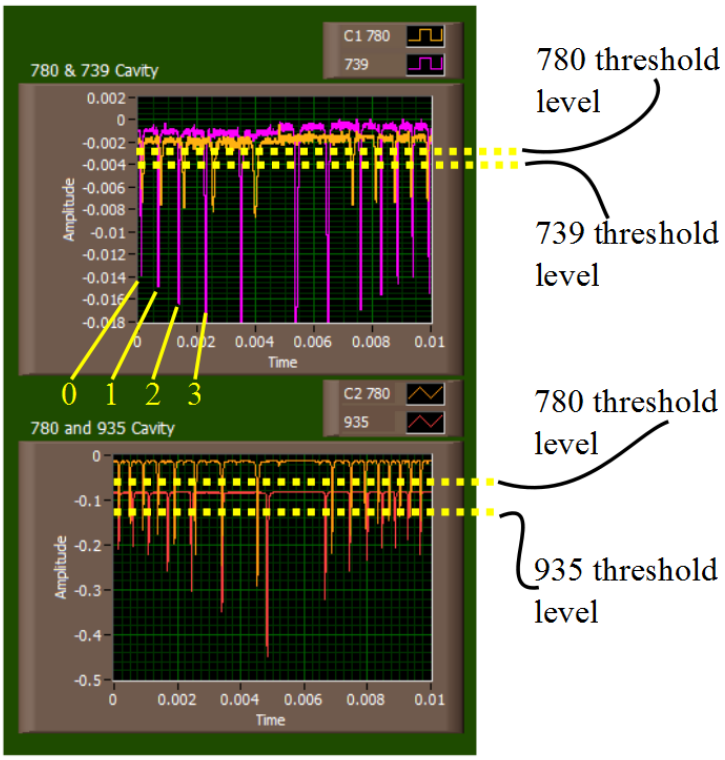

Figure 4.7: Enlarged view of the cavity signal display on the LabVIEW programme. Shown is the numbering system for the peaks (left to right and starting at zero) and the threshold level chosen to detect the peaks.

Figure 4.8: Enlarged view of the controls used to detect the cavity peaks. Here, the threshold level above which a peak must pass along with the minimum width a peak above the threshold must have in order to be counted by the programme can be adjusted. The number of peaks detected by the programme is displayed allowing the user to determine if the control settings are correct.

- Ensure that the polarity and integral time inputs are set to zero.

By setting all these values to zero it ensures that there is no error signal being created by the programme and sent to the cavities when the thermal locking process is started.

- Enter the value in box called “80 thermal lock peak” into the “780 peak position” box. This should be done for each cavity separately.

The box “780 thermal lock peak” displays the position of a selected cavity peak from the 780 nm laser, as shown in figure 4.7. The “780 peak position” box provides a set point for the locking programme and so the programme will, given the correct settings, provide feedback to keep the peak in the position provided in this box over successive cavity scans.

- For the 739 nm thermal lock a polarity of -10 should be entered.

- For the 935 nm thermal lock a polarity of 10 should be entered.

The magnitudes of the thermal lock polarities are not of exact importance as they simply scale the generated error signal outputted by the programme. This scaling of the error signal can also be achieved externally from the programme via the individual piezo’s driving amplifiers (Piezomechanik: SVR 150/3). A larger magnitude than 10 can be used

provided this does not cause the error signal to saturate the output card. The sign of the polarity, however, is important as the wrong sign will cause the feedback to move the peak position away from the set point instead of towards it. The differing signs of the 739 nm and 935 nm thermal lock polarities arises from the use of a non-inverting and an inverting summing amplifier to apply respective cavity error signals to their drive signal, as shown in figure 4.5.

- For both cavities thermal locks, a value of 0.0001 should be entered in the integral time box
- The cavities should now be thermally locked.

The number entered into the integral time box is the inverse of the gain factor for the integral part of the PI feedback provided by the programme. The smaller the number the faster the programme will act to move the peak towards the set point and vice versa. Care must be taken if this number is reduced below that stated as high frequency noise on the cavity will cause the thermal lock feedback to become unstable.

If the steps followed above are successful, nothing should visibly change in the cavity display window. If the peaks move suddenly across the display, the polarity and integral should be set to zero and the process followed again. If the problem persists a common issue is that the polarity is of the wrong sign, and it is advised to try swapping this sign when repeating the steps again.

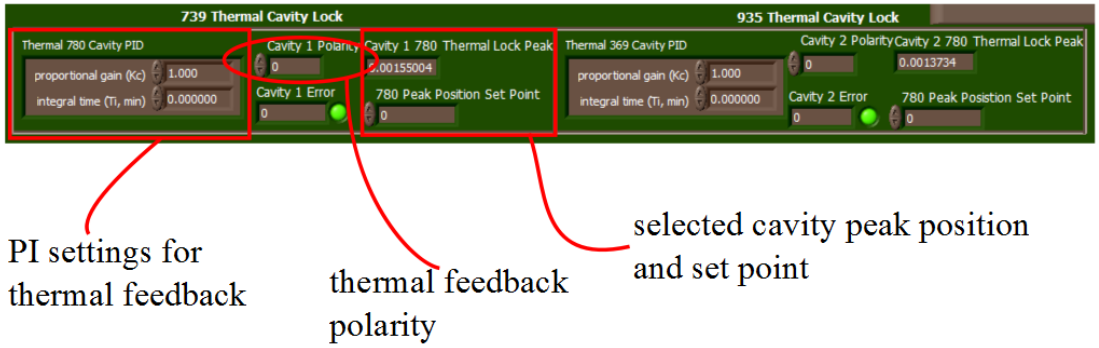

Figure 4.9: Enlarged view of the controls used to produce error signals to counter the effects of thermal drift of the cavities.

4.4.3 Locking the lasers

Once the peak detection and thermal locking of the cavities has been successfully implemented feedback to transfer the stability of the 780 nm reference laser to the 739 nm and 935 nm lasers can be implemented. Figure 4.10 shows an enlarged view of the controls which set up the error signals needed to lock the two lasers. To provide an error signal for the lasers the following steps should be carried out:

- Ensure that the polarity and integral time of the two cavity controls are set to zero.

Setting the polarity and integral time of the cavity controls to zero ensures that no error signal is being produced by the programme and being sent to the lasers at the beginning of the locking procedure.

- For both cavities two adjacent 780 nm peaks should be selected using the "peak selector" controls.

The 780 nm peaks chosen should not be the first two peaks of the scan but instead two peaks located in the centre of a bunch of peaks. For the front panel image shown in figure 4.6 the 780 nm peaks 1 and 2 are used for the 739 nm and 780 nm cavity (red boxes) and the peaks 2 and 3 are used for the 739 nm and 780 nm cavity (blue boxes). It is important to note that the peaks are numbered left to right and starting at zero, as shown in figure 4.7.

- If the peak detection procedure and cavity thermal control procedure (given in sections 4.4.1 and 4.4.2 respectively) have been set up correctly the value displayed in the boxes "739 Ratio" and "935 Ratio" should be stable. These values may drift but they should not increase or decrease suddenly. If they are not stable (if the value randomly varies) then it is likely that the peak detection has not been implemented correctly.

The "739 ratio" and "935 ratio" boxes display the ratio of a (the distance from a reference 780 nm cavity peak to a locked 739 nm or 935 nm cavity peak, depending on the cavity in question) to b (the distance between two 780 nm reference cavity peaks). This ratio can be seen in figure 4.1.

- The ratio displayed in the "739 Ratio" should be placed into the "739 Set Point" box.

- The ratio displayed in the "935 Ratio" should be placed into the "935 Set Point" box.

The programme will act to keep the ratio a/b of each cavity constant at their respective values entered in the "739 Set Point" and "935 Set Point" boxes. If the values in these boxes are altered, then the programme will provide an error signal which will act on the 739 nm and 935 nm lasers changing their frequencies in order to create the a/b ratio given in the boxes.

- A polarity of -1 should be entered into the boxes "739 Polarity" and "935 Polarity".

These values set the scaling of the error signal which the programme produces. The sign of these values is important as the wrong sign can cause the laser frequencies to be sent away from the desired set points by the error signal instead of towards them.

- In the PI settings the value 0.001 should be entered into the "integral time" box.

The number entered into the integral time box is the inverse of the gain factor for the integral part of the PI feedback provided by the programme. The smaller the number the faster the programme will act to alter the ratio a/b towards the desired set point by changing the locked laser (935 nm or 739 nm lasers) frequency. Care must be taken if this number is reduced below that stated as high frequency noise on the laser frequencies will cause locking to become unstable.

- The wavelength of the 935 nm and 739 nm lasers should now be stable. Alterations to the wavelength can be made by increasing/decreasing the third digit after the decimal place in the "935 Set Point" and "638 Set Point" boxes.

- If one of the laser wavelengths at any point become unstable set the polarity and integral time to 0 and repeat the locking procedure for the cavity in question.

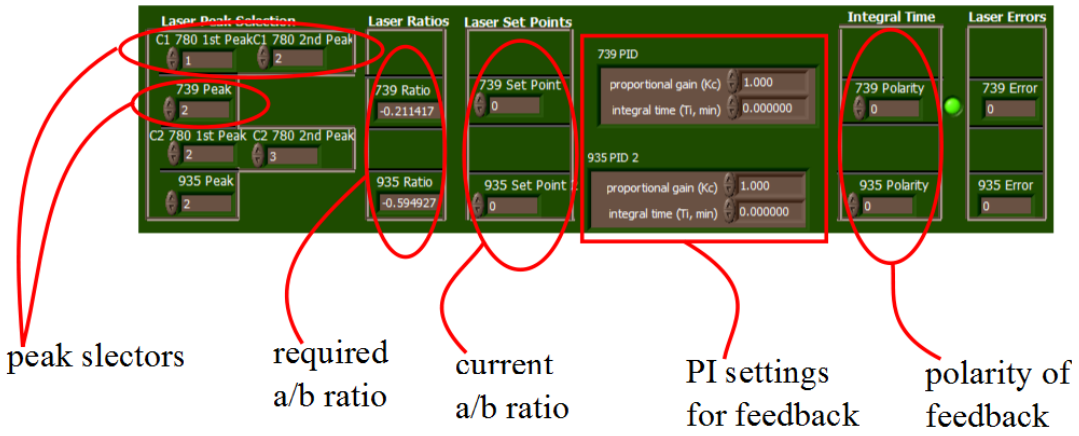

Figure 4.10: Enlarged view of the controls used to produce error signals from the detected peaks. Shown are the peak selector controls, PI setting controls and the polarity controls.

Chapter 5

The application of radio frequency voltages to ion traps via helical resonators

5.1 Introduction

Trapped ions are a powerful tool which have many applications such as mass spectrometry [38] and frequency standards [55, 56], whilst also being recognised as a leading contender for the practical implementation of quantum information processing [14, 26, 57] and quantum simulations [58, 59, 60, 61]. To trap ions within a Paul trap a radio frequency high voltage is applied to electrodes in order to produce the required pseudo potentials. A helical resonator allows impedance matching between a radio frequency source and an ion trap enabling high voltages while reducing the noise injected into the system. These properties make the resonator an important device not only in ion trapping but also in a wide range of physical sciences including ultra high frequency (UHF) mobile communication systems [62], spin resonance spectroscopy [63] and measuring the dielectric properties of materials [64].

An empirical study of shielded helical coil resonators was performed by Macalpine and Schildknecht [65] who considered isolated operation with a self resonant frequency due to the coil inductance and shield capacitance. In contrast this work considers a shielded helical coil connected to an ion trap where the resonant frequency will be determined by the whole system. Macalpine and Schildknecht [65] showed that, when tuning a resonator with an external capacitance, the Q factor would vary with the tuned resonant frequency, however, they did not predict this resonant frequency or the effect of a lossy (resistive)

capacitance on the Q factor. Due to these limitations, when connecting an ion trap to a helical resonator the predications of Macalpine and Schildknecht [65] for the resonant frequency and Q factor can deviate by orders of magnitude from those observed. This work will provide reliable predictions for the resonant frequency and Q factor for a shielded helical coil connected to an ion trap impedance. A design guide which allows a helical resonator to be constructed with the highest possible Q factor for the constraints of a particular experiment will also be provided along with a discussion on the process of impedance matching with a helical resonator and the voltage applied to the ion trap as a function of the Q-factor, input power and the properties of the resonant circuit will be predicted.

5.2 The Resonator: A radio frequency source

A common way of applying the radio frequency voltage to ion traps is via a helical quarter wave resonator. This can be thought of, quite simply, as the commonly used coaxial quarter wave resonator with the addition that its central conductor is wound into a helix. The reason for such a winding is a space saving one, which can be demonstrated by comparing the physical size of a helical resonator, with a resonant frequency in the tens of MHz, with that of a coaxial resonator. In this case the respective sizes would be on the order of 100 mm by 100 mm and 7620 mm by 76 mm [65]. In order to successfully construct a resonator it is important to obtain a detailed understanding of its operation. It is the aim of this section to give an overview of the main properties of the resonator in order to familiarise the reader with the central workings of the device, namely impedance matching, calculation of the output voltage and a list of equations used to help design a resonator.

5.2.1 Output voltage

The application of high voltages must be limited to avoid either electrical breakdown or experimentally intrusive temperatures due to the power dissipated in the ion trap. It is, therefore, important to know the voltage being applied to the ion trap for a given input power. A combined ion trap-resonator system can be represented as a series LCR circuit with resonant frequency $\omega_0 = \frac{1}{\sqrt{LC}}$ and $Q = \frac{1}{R}\sqrt{\frac{L}{C}}$. The voltage across the ion trap will be approximately equal to the voltage across the capacitor when the capacitance of the ion trap dominates the overall capacitance of the circuit. At resonance the peak voltage over the capacitor is equal to the peak voltage over the inductor. The instantaneous voltage of

the inductor is

$$V(t) = L\frac{dI_{peak}\sin(\omega_0 t)}{dt} = L\omega_0 I_{peak}\cos(\omega_0 t), \tag{5.1}$$

where I_{peak} is the peak current and L is the coil inductance. The peak voltage over the inductor occurs when $\cos(\omega_0 t) = 1$, hence the peak voltage over the ion trap can be approximated as

$$V_{peak} \approx LI_{peak}\omega_0. \tag{5.2}$$

Power is only dissipated in the system through the resistance R, thus the power dissipated is

$$P_d = RI_{rms}^2 = \frac{1}{2}RI_{peak}^2, \tag{5.3}$$

where $I_{rms} = \frac{1}{\sqrt{2}}I_{peak}$ is the root-mean-square current. Using these equations and $Q = \frac{1}{R}\sqrt{\frac{L}{C}}$, we find that

$$V_{peak} \approx \kappa\sqrt{2P_d Q}, \tag{5.4}$$

where,

$$\kappa = \left(\frac{L}{C}\right)^{\frac{1}{4}}, \tag{5.5}$$

and $V_{rms} = V_{peak}/\sqrt{2} \approx \kappa\sqrt{P_d Q}$. Here κ can be interpreted as a geometric factor as the values of the capacitance, C, and the inductance, L, are given by the geometry of the resonator which will be described in detail in section 5.3.3.

This shows the output voltage of a resonating system can be predicted given the input power, P, the capacitance, C, inductance, L, and quality factor Q of the system. Applying RF voltages via a high Q factor resonator reduces the power in unwanted frequencies being applied, reducing their contribution to motional heating of ions [66] and also provides higher voltages per input power, resulting in deeper trapping potentials and higher secular frequencies.

The impedance of the ion trap and connections are typically large enough to contribute to the response of the LCR resonator, and thus must be considered when designing a resonator to operate at a given frequency. Considering $\omega_0 = \frac{1}{\sqrt{LC}}$ and $Q = \frac{1}{R}\sqrt{\frac{L}{C}}$, in order to maximise the Q factor for a fixed frequency ω_0 we must minimise C while maximising L. The use of a helical coil allows for an inductor to be made with a low self capacitance

and resistance, enabling the resistance and capacitance of the ion trap and connections to dominate the R and C of the LCR resonator and thus maximising the Q factor.

5.3 Circuit model

5.3.1 Impedance matching via inductive coupling

RF voltages could be applied by direct connection from the ion trap to an RF amplifier; however this can cause multiple issues. A mismatch of impedance between the amplifier and the ion trap will cause the RF signal to be reflected from the ion trap, resulting in power dissipated over the output impedance of the amplifier. This would require an RF amplifier with a much greater power handling than for a matched system. The amplifier also injects noise into the ion trap which can cause heating of the ion [66]. Passing the output of the amplifier through a resonator filters this noise, reducing the contribution to ion heating. In order to maximise the filtering of this noise the resonator must have a high Q factor, and hence a narrow bandwidth. Direct connection of a resonator to the amplifier will reduce the resonator's Q factor due to the damping effect of the finite output impedance of the amplifier. The RF amplifier can, however, be connected to the resonator through a capacitive or inductive coupling, which decouples the resonator from the resistive output impedance of the amplifier, allowing for a resonator with a high Q factor. This technique also allows impedance matching of the ion trap and RF amplifier by altering the coupling, thus reducing the reflected power, and hence the required power for a given voltage.

For inductive coupling an antenna coil is attached to an end cap and placed directly and centrally above the main helical coil as shown in figure 5.1. By altering the physical properties of this coil, impedance matching between the resonator and the radio frequency source can be achieved.

To understand how altering the physical properties of the antenna coil allows impedance matching, the resonator is represented by two electrically isolated circuit loops as shown in figure 5.2. Here the inductor, L_1, represents the antenna coil and the inductor, L_2, represents the main coil. The voltage source V_s and impedance Z_0 represent the output of an RF amplifier. The two coils are placed in close proximity to each other creating a coupling between the two circuit loops due to the mutual inductance.

The voltage in each circuit loop is given by

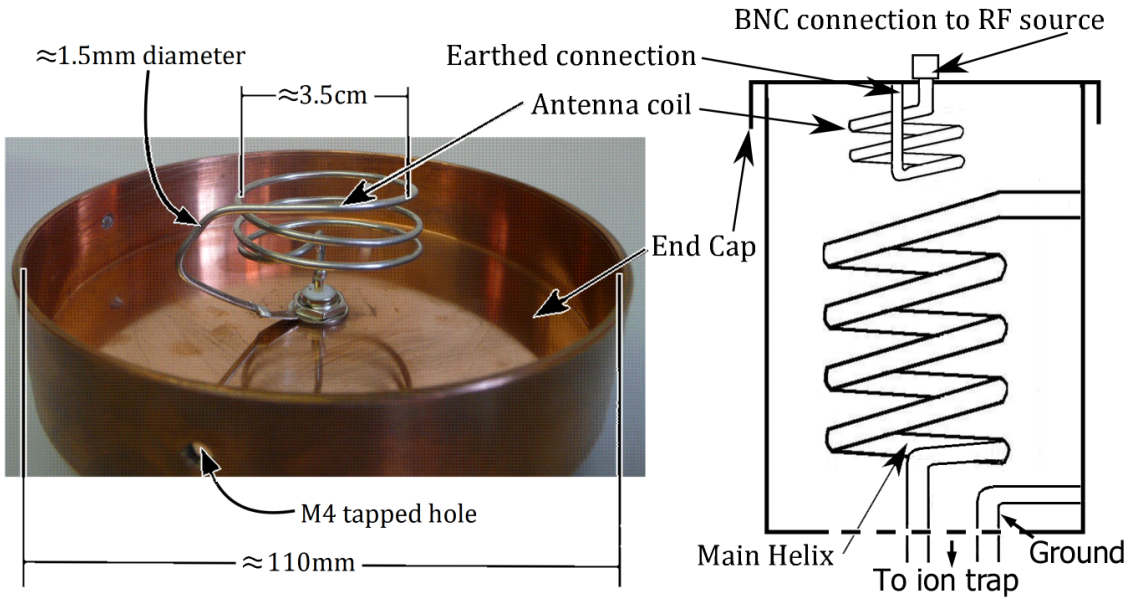

Figure 5.1: A resonator end cap showing the antenna coil together with a diagram showing its location in a fully constructed helical resonator.

$$V_{1/2} = i\omega L_{1/2} I_{1/2} + i\omega M I_{2/1}, \tag{5.6}$$

where $M = k\sqrt{L_1 L_2}$ is the mutual inductance of the two coils and k is the coupling. The electrical equivalent circuit is given in figure 5.2(b) where the impedance Z_{in} describes the overall impedance of the resonator (and ion trap), which can be adjusted by altering the physical parameters of the antenna coil enabling an impedance match to the RF amplifier (V_s and Z_0). The overall impedance, Z_{in}, of the two circuits, as shown in figure 5.2, is then

$$Z_{in} = V_1/I_1 = i\omega L_1 + i\omega M \frac{I_2}{I_1}. \tag{5.7}$$

Using

$$V_2 = -Z_L I_2 \tag{5.8}$$

and equation 5.6 we obtain

$$(Z_L + i\omega L_2) I_2 + i\omega M I_1 = 0. \tag{5.9}$$

Rearranging equation 5.9 for I_2/I_1 gives

$$\frac{I_2}{I_1} = \frac{-i\omega M}{Z_L + i\omega L_2}. \tag{5.10}$$

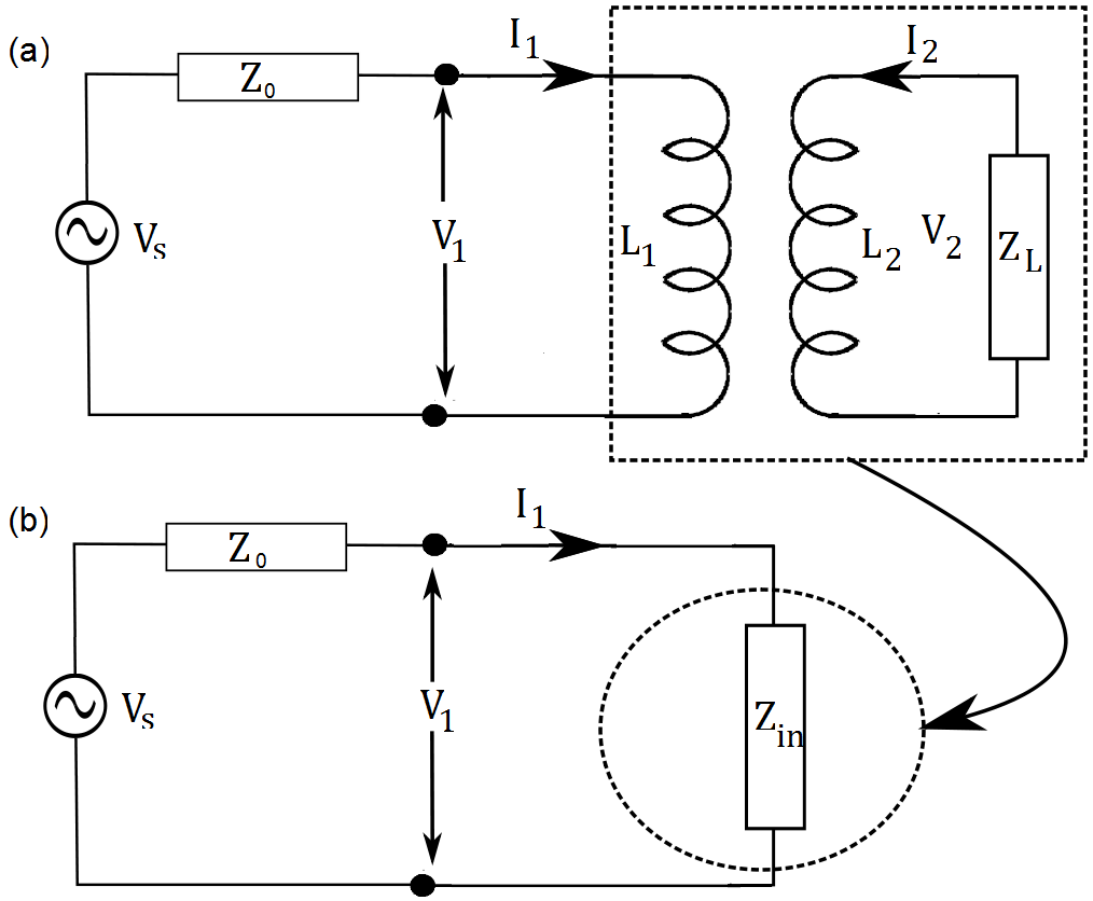

Figure 5.2: (a) Circuit of a resonator with attached load (inside dashed box) and signal generator (outside dashed box) represented as two physically separate circuit loops coupled together by the antenna coil inductor, L_1, and the main coil inductor, L_2. The impedance of the ion trap is shown as a load impedance, Z_L. The source voltage and impedance (outside dashed box) are shown as V_s and Z_0 respectively. (b) The circuit from (a) is represented as the Thévenin equivalent impedance, Z_{in}, along with the source voltage and impedance.

Inserting equation 5.10 into equation 5.7 we can describe the overall impedance as

$$Z_{in} = i\omega L_1 + \frac{\omega^2 M^2}{i\omega L_2 + Z_L}. \tag{5.11}$$

Approximating the antenna coil's inductance L_1 as $\frac{\mu_0 NA}{\tau}$, where τ, N and A are the winding pitch, number of turns and cross sectional area of the coil respectively and μ_0 is the permittivity of vacuum, gives

$$Z_{in} = \frac{\mu_0 NA}{\tau}\left(i\omega + \frac{k^2 L_2 \omega^2}{i\omega L_2 + Z_L}\right). \tag{5.12}$$

This shows that the input impedance of the resonator can be altered by simply adjusting the physical parameters of the antenna coil and, thus, match it to that of the voltage source. To illustrate how the physical parameters have to be altered to achieve a matching, equation 5.12 has been plotted in figures 5.3 and 5.4 for two common cases. The first case (solid black line) is when the combined resonator-ion trap load is high (a resistance of 15 Ohm and a capacitance of 100 pF) and the second (dashed black line) when the load is small (a resistance of 0.2 Ohm and a capacitance of 1 pF). In both cases the traps are driven at a frequency of $\omega = 2\pi \times 20$ MHz. Figure 5.3 shows the ratio of number of antenna turns to winding pitch as a function of the diameter of the coil required to impedance match the load to a 50 Ohm source. Figure 5.4 then illustrates how an existing antenna coil can be physically stretched (increasing the winding pitch of the coil) to impedance match to a source load. In figure 5.4 the number of turns is kept constant at three and the diameter is kept constant at 3 cm.

Figure 5.4 shows that in order to impedance match a source to a high impedance trap load (solid line) the antenna coil must be stretched compared with that required to match a low impedance trap load (dashed line).

5.3.2 Description of resonant frequency and Q factor using an LCR circuit model

In order to calculate the Q factor and resonant frequency, ω_0, the resonator is modelled as a lumped element circuit, shown in figure 5.5(a), which is simplified via figure 5.5(b) to figure 5.5(c) by creating Thévenin equivalent impedances, where each component is defined in the table in figure 5.5(d).

The coil impedance will depend on the mutual coupling, Z_M, which can be written as

$$Z_M = iX_{Lc} + \frac{\omega^2 M^2}{i\omega L_a + Z_0} \tag{5.13}$$

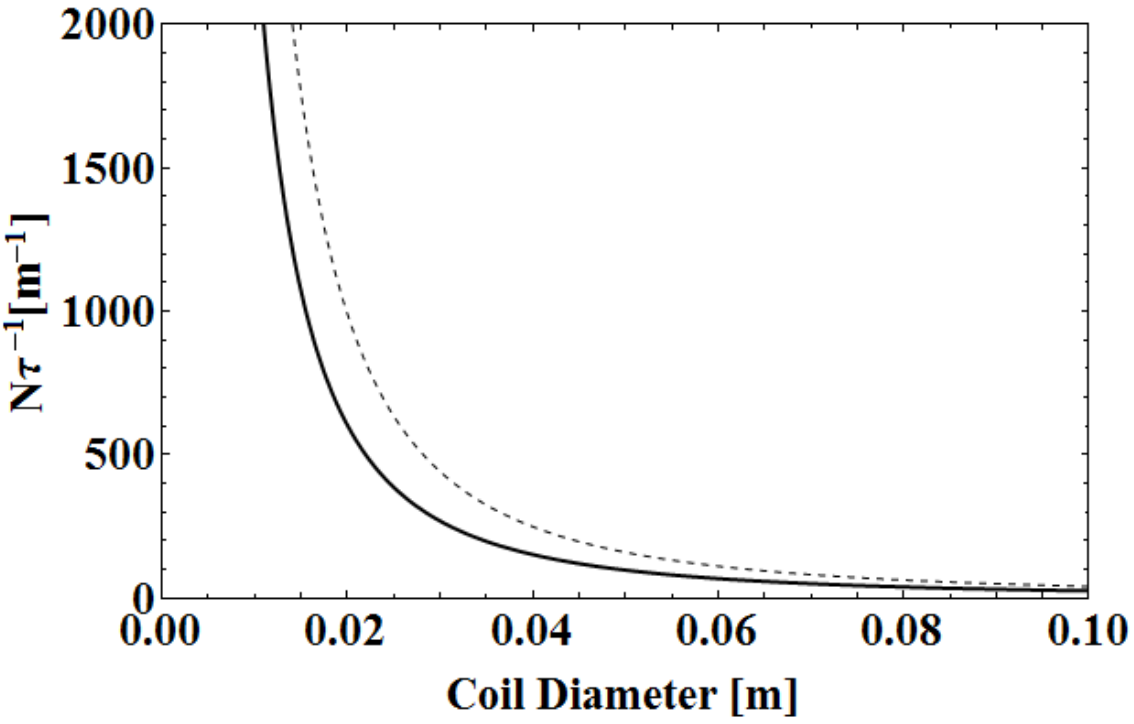

Figure 5.3: The ratio of number of antenna turns N to winding pitch τ, required to impedance match the load to a 50 Ohm source is plotted as a function of the antenna coil diameter. This is shown for the case when the combined resonator-ion trap load is high (solid black line, a resistance of 15 Ohm and a capacitance of 100 pF), and for the case when the load is small (dashed black line, a resistance of 0.2 Ohm and a capacitance of 1 pF). In both cases a resonant frequency of $\omega = 2\pi \times 20$ MHz is used.

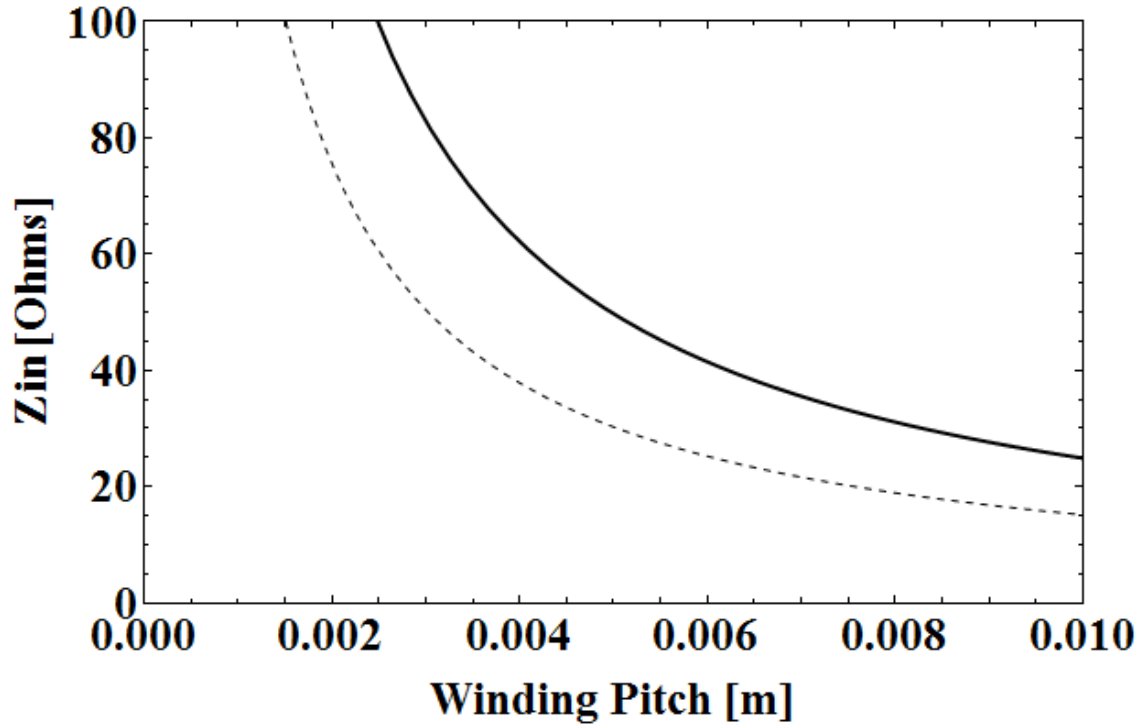

Figure 5.4: The resonator input impedance, Z_{in}, is shown as a function of the winding pitch, τ, of the antenna coil. This is shown for the case of a high combined resonator-ion trap load (Z_L given by a resistance of 15 Ohm and a capacitance of 100 pF) shown by the solid black curve and for the case of a small load (Z_L given by a resistance of 0.2 Ohm and a capacitance of 1 pF) shown by the dashed black curve. In both cases a resonant frequency of $\omega = 2\pi \times 20$ MHz is used and the number of turns and coil diameter are kept constant at 3 and 3 cm respectively.

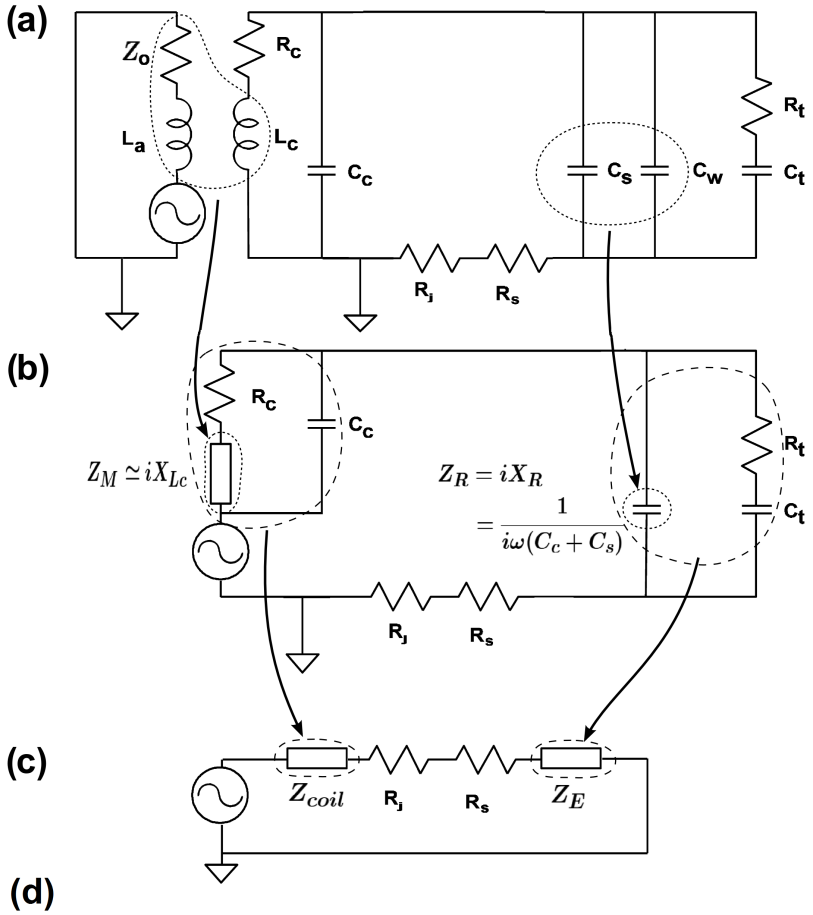

Z_{coil} Equivalent impedance of the Helical coil due to:
- R_c Helical coil resistance
- C_c Helical coil self capacitance
- Z_M Helical coil total inductance due to:
  - L_c Helical coil self inductance
  - L_a Antenna coil self inductance
  - Z_o RF voltage source impedance (typically 50Ω)

Z_E Equivalent impedance of the experimental system due to:
- R_t Ion trap resistance
- C_t Ion trap capacitance
- X_R Equivalent capacitance due to:
  - C_s Capacitance of Helical coil to surrounding shield
  - C_w Capacitance of the ion trap connecting wires

R_j Helical coil to shield junction resistance

R_s Shield resistance

Figure 5.5: Diagram showing the electrical equivalent of the overall resonant circuit. Part (a) shows the lumped element model electrical equivalent. Part (b) shows the simplified circuit. Part (c) shows the set of serial impedances the resonator can be represented as.

by using the same method employed to arrive at equation 5.11, where $X_{Lc} = L_c\omega$ is the reactance due to the inductance of the main coil. However, with the typical values required by ion trapping of RF drive frequency between $\omega \approx 2\pi \times 10$ MHz and $2\pi \times 50$ MHz, $L_c \approx L_a \approx 1$ mH and $Z_0 = 50$ Ohm it can be shown that $|Z_M| \approx iX_{Lc}$ and, thus, express:

$$Z_{coil} = \left(\frac{1}{(iX_{Lc} + R_c)} + \frac{1}{iX_{Cc}}\right)^{-1}. \tag{5.14}$$

Summing the trap capacitance and resistance in parallel with the wire capacitance and shield capacitance we can write the Z_E impedance as

$$Z_E = \left(\frac{1}{(iX_{Ct} + R_t)} + \frac{1}{iX_{Cw}} + \frac{1}{iX_{Cs}}\right)^{-1}, \tag{5.15}$$

where $X_{C_t} = \frac{1}{C_t\omega}$ is the reactance of the trap capacitance and X_{C_w} and X_{C_s} are the reactance due to C_w and C_s respectively.

The total impedance of the resonator, Z_{tot}, can then be expressed as

$$Z_{tot} = Z_{coil} + Z_E + R_s + R_j. \tag{5.16}$$

with $Z_{coil} = R_{coil} + iX_{coil}$ and $Z_E = R_E + iX_E$, where R_{coil} and R_E are the equivalent series resistance of the coil and experimental system respectively and X_{coil} and X_E are the equivalent series reactance for the coil and experimental system respectively. At resonance Z_{tot} will be purely resistive when

$$X_{coil} + X_E = 0. \tag{5.17}$$

From the calculated Thévenin equivalent impedances from figure 5.5 it can be shown that at resonance,

$$\frac{i\omega_0 L_C}{1 - L_C C_C \omega_0^2} + \frac{1}{i\omega_0(C_s + C_t + C_w)} = 0. \tag{5.18}$$

This equation can be used to calculate the resonant frequency:

$$\omega_0 = \frac{1}{\sqrt{(C_s + C_t + C_w + C_C)L_C}}. \tag{5.19}$$

The Q factor is defined as $Q \equiv \omega_0 \frac{\text{Energy stored}}{\text{Power dissipated}}$. The energy stored in the resonator will oscillate between the inductance of the coil and the combined capacitances in the circuit. The total energy stored will be equal to the peak energy stored in the inductor $E_{Lc} = I_{peak}^2 L_c/2 = I_{rms}^2 L_c$ and the power dissipated in the system is $P_d = I_{rms}^2 R_{_{ESR}}$

where R_{ESR} is the equivalent series resistance of the circuit and is given by the real part of equation 5.16. It can then be shown that the Q factor of a resonator is given by the following:

$$Q = \frac{X_{L_c}}{R_{ESR}}. \tag{5.20}$$

From equation 5.16, R_{ESR} can be derived as

$$R_{ESR} = \frac{R_c X_{Cc}^2}{R_c^2 + (X_{Cc} + X_{Lc})^2} + \frac{R_t X_R^2}{R_t^2 + (X_R + X_T)^2} + R_s + R_j. \tag{5.21}$$

For helical coils with a low self capacitance ($X_{Lc} \ll X_{Cc}$) and low resistance ($R_c \ll X_{Cc}$), and for an ion trap with low resistance such that $R_t \ll (X_{Ct} + X_{Cw} + X_{Cs})$, this can be approximated as

$$R_{ESR} \simeq R_j + R_c + R_s + R_t \alpha^2, \tag{5.22}$$

where $\alpha = \frac{a}{a+1}$, $a = \frac{X_R}{X_T} = \frac{C_t}{C_s + C_w}$ is the ratio of the trap capacitance to the combined capacitance due to the connecting wires and coil shield. For $a \to 0$ the capacitance of the shield and wires shunt the RF current and there is negligible contribution from the resistance of the ion trap. For $a \to \infty$ the trap capacitance dominates giving a maximum contribution of the ion traps resistance.

It should be noted that, as high Q factors are obtained when maximising the coil inductance and minimising the system capacitance, the effect of wire and feed-through inductance will be negligible compared to a typical coil inductance and, as such, has not been included in the model. This is not true of stray capacitances which can be on the same order of magnitude as the ion trap capacitance and can be treated as part of the wire capacitance C_w.

5.3.3 Resonator Capacitance, Inductance and Resistance

In order to construct a resonator to operate at a desired frequency the capacitance of the wires and ion trap $C_\Sigma = C_w + C_t$, which depend on the configuration of the ion trap and experimental setup, can be measured at the vacuum systems feed-through with a capacitance meter. Once these are known we must construct a shielded coil with the necessary capacitance C_c and C_s and inductance L_C. All equations in this section assume the use of SI units unless otherwise stated. It is also important to note that the predictive power of this work depends on the following equations and so it is important to understand

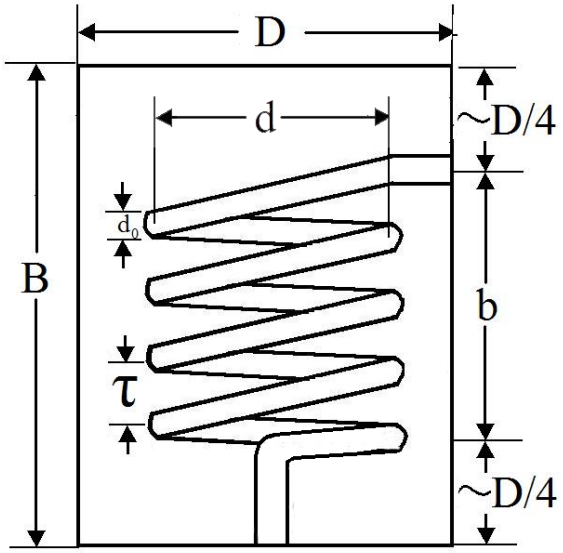

Figure 5.6: Outline design of a resonator showing the shield diameter D, shield height h, coil diameter d, coil height b, winding pitch τ and the coil wire diameter d_0

any approximations made by them. The self capacitance of the coil in units of farads, given empirically by Medhurst, is [67]

$$C_C \simeq (Hd) \times 10^{-12} \text{ farads}, \tag{5.23}$$

where d is the diameter of the coil and H is given empirically by, $H = 11.26\frac{b}{d} + 8 + \frac{27}{\sqrt{\frac{b}{d}}}$ farads/metre. This equation assumes a closely spaced coil which means that the pitch angle is small. As the pitch angle increases the self capacitance will decrease until it is that for a straight wire. This results in equation 5.23, at worst, producing an over estimate of the self capacitance in the case of widely spaced coils. However, the use of this overestimate still results in self capacitances which are small when compared to other capacitances in the system and, so, approximations made later in this work for low self capacitance are just as valid even in the case of widely spaced coils.

The capacitance present between the coil wire and the outer shield in units of farads is given empirically by [65]

$$C_s \approx bK_{Cs}\left(d, D\right) \text{ farads}, \tag{5.24}$$

where $K_{Cs}\left(d, D\right) = 39.37\frac{0.75}{\log\left(\frac{D}{d}\right)} \times 10^{-12}$ farads/metre, d is the diameter of the coil, D the inner shield diameter and b is the height of the coil.

The inductance of a coil inside a shield in units of henrys, for $b/d \geq 1$, is given empirically by [65]

$$L_C \approx bK_{Lc}\left(d, D, \tau\right) \text{ henrys}, \tag{5.25}$$

where $K_{Lc}\left(d, D, \tau\right) = 39.37\frac{0.025d^2(1-(\frac{d}{D})^2)}{\tau^2} \times 10^{-6}$ henrys/metre and τ is the winding pitch of the coil. For both equations 5.24 and 5.25 an assumption is made that $\tau < d/2$. In order to invalidate this long coils with few turns would have to be made and would almost cease to be helical in nature. This assumption is, therefore, valid for all cases considered in this work.

We can approximate the required height of a coil, b, for a resonator to operate at frequency ω_0, for chosen parameters of d, D and τ and for a set of measured capacitances $C_\Sigma = C_w + C_t$. The coil's self capacitance, given by equation 5.23, significantly complicates the solution for coil height, b, however a simpler solution can be found by approximating the self capacitance as a linear equation. Examining equation 5.23 it can be seen that the maximum of the non linear term $\frac{27}{\sqrt{b/d}}$ occurs when $b/d < 1$. As we require that $b/d \geq 1$ a simple linear approximation for the coil self capacitance can be found by setting the $\sqrt{b/d}$ term to 1. This gives an overestimate of the self capacitance but allows for an approximate solution for the coil height which will give a resonator with a resonant frequency typically within 2% of the desired frequency. The linear approximation to the coil self capacitance is, $C_C \simeq K_{cb}b + K_{cd}$, where $K_{cb} = 11.26 \times 10^{-12}$ farads/metre and $K_{cd} = 35d \times 10^{-12}$ farads. Substituting this approximation with equations 5.25 and 5.24 into equation 5.19 and rearranging for b in units of metres, we obtain:

$$b \simeq \frac{C_\Sigma + K_{cd}}{K_{Cs} + K_{cb}} \left(\sqrt{\frac{K_{Cs} + K_{cb}}{(C_\Sigma + K_{cd})^2 K_{Lc}\omega_0^2} + \frac{1}{4}} - \frac{1}{2} \right) \text{ metres}. \tag{5.26}$$

In order to estimate the resistance of the resonator one must consider the path along which the current flows and how it flows along this path. The current will flow along the surface on its path with a depth, δ, given by the skin depth of the coil material (in this case copper) at the resonant frequency of the resonator. This current is a result of a straight up current in the shield flowing back to ground and an induced current flowing around the circumference of the shield which acts to form an equal and opposite magnetic field to that produced by the coil (Lenz's Law). The distance around the shield the current will travel, l_s, can be calculated by equating the magnetic field, created by the coil at the shields surface:

$$B_{field} = \frac{\mu I l_c}{4\pi(D-d)^2}, \tag{5.27}$$

to that created by the shield B_{shield}:

$$B_{shield} = \frac{\mu N_s I}{b}, \tag{5.28}$$

where l_c is the unwound length of the coil.

This can then be solved to find the number of turns the current undergoes in the shield, N_s:

$$N_s = \frac{b l_c}{4\pi(D-d)^2}. \tag{5.29}$$

The distance the current will travel from the bottom of the shield to the top of the shield can then be calculated as

$$l_s = N_s \sqrt{(\pi^2 D^2) + \left(\frac{b}{N_s}\right)^2}. \tag{5.30}$$

The resistance of the coil and the shield can now be calculated using the relationship between resistance, R, and resistivity, ρ:

$$R = \frac{\rho l_s}{A}, \tag{5.31}$$

where l is the length along which the current travels and A the area through which the current travels. The resistance of the coil and shield can now be described as

$$R_c = \frac{\rho l_c}{d_0 \pi \delta}, \tag{5.32}$$

$$R_s = \left(\frac{N_s \rho l_s}{b\delta}\right), \tag{5.33}$$

where d_0 is the diameter of the coil wire.

Additional resistances acquired by attaching the coil to the shield must also be taken into account. The coils in this work are attached to the shield by soldering them onto a BNC bulkhead located at a distance $\frac{D}{4}$ from the top of the shield as indicated in [65] and figure 5.12. The solder joint created by this method will provide an additional resistance. The resistance of the connection at an angular frequency, ω_n is given by

$$R_n = \frac{\rho l}{\pi d_j \delta_n}, \tag{5.34}$$

where ρ is the resistivity of the material, l is the length through which the current flows, δ_n is the skin depth at an angular frequency ω_n and d_j is the diameter of the solder joint. Due to the effects of skin depth at high frequencies a simple DC resistance measurement of the

joint connecting the coil to the shield is not useful. Instead an AC resistance measurement must be made of the joint. Equipment exists (for example ISO-TECH: LCR819) which can perform resistance measurements at frequencies of approximately 100 kHz and this measurement can then be used to infer the resistance of the joint at a higher frequency, in this case the resonant frequency of the resonator. The measurement frequency needs to be chosen so that the skin depth is smaller then the radius of the joint. By defining $\gamma = (\rho l)/(\pi d_j)$ equation 5.34 can be re-written as

$$R_n = \frac{\gamma}{\delta_n}. \tag{5.35}$$

By using the frequency independent parameter, γ, it is possible to show for two different angular frequencies, ω_1 and ω_2,

$$R_1\delta_1 = R_2\delta_2, \tag{5.36}$$

and rearranging using $\delta_n = \sqrt{(2\rho)/(\omega_n\mu_0)}$ gives the resistance at a resonant angular frequency ω_0 in terms of the resistance measured at an angular frequency ω_1:

$$R_0 = R_1\sqrt{\frac{\omega_0}{\omega_1}}. \tag{5.37}$$

This derivation is only valid in a frequency regime where the solder joint is larger than the skin depth and when the resistivity, ρ, of the material is constant over the two frequencies used. This is the case for the resonators made in this work as the skin depth is of the order of 10 µm and the solder joint size is on the order of a few millimetres.

Equation 5.37 shows that by taking a resistance measurement at one frequency it is possible to calculate the resistance at another frequency. This method was used to calculate the resistance of the connection made between the main coil and the shield at the resonators resonant frequency.

5.4 Resonator design guide and analysis

5.4.1 Design guide

This section will provide a design guide which will enable a helical resonator to be constructed with a Q factor close to that of the highest Q possible for a given set of parameters consisting of the desired resonant frequency, ω_0, ion trap capacitance, C_t, and resistance, R_t, wire capacitance, C_w and the size constraints for the resonator. The helical resonator may require different construction techniques depending on priorities set by these

constraints, however there are some design issues universal to any resonator that must be considered.

When designing a resonator it is important that certain constraints are met for the resonant frequency and Q factor to be predicted by the theory. The resonant frequency depends on the inductance, which is predicted by equation 5.25. For this equation to be valid the coil height should be greater than the coil diameter, $b \geq d$, and the coil diameter should be greater than the wire diameter, $d \geq d_0$.

It can be seen from equation 5.25 that both the coil diameter and the winding pitch have a strong (d^2 and $1/\tau^2$) effect on the inductance. It is important to ensure the coil is made with precision for the winding pitch and the diameter of the coil to be constant along its length. This dependence also requires that the coil is not susceptible to mechanical vibrations. The strong effect the winding pitch, τ, has on the inductance will result in vibrations of the coil causing the inductance and hence resonant frequency of the resonator to become time dependent. In order to minimise vibrational effects the coil should be constructed to be rigid and should be firmly mounted inside the shield. Finally, the coil must be mounted centrally inside an outer shield of height $B \geq b + D/2$ (typically $B = b + D/2$ is recommended), where b is the coil height and D is the shield diameter, in order to keep the coil fringe effects from reducing the coil's inductance and increasing the shield capacitance [68].

In order to achieve high Q factors the resonator must be built to minimise the resistance of the shield, the coil and solder joints. The coil and shield should be made from a highly conductive material (such as copper) which is thicker than the skin depth at the desired operating frequency. Any solder junctions should be made with a clean oxide free surface before soldering, with both parts of the joint reaching a sufficient temperature to ensure good solder flow between them.

A low resistance for the helical coil can be obtained by ensuring the use of a large diameter wire, d_0. The effect of the wire diameter on the Q factor can be seen by plotting the 'largest' Q factor vs wire diameter d_0. The 'largest' Q factor available, Q_{large}, is defined for a given set of parameters, ω_0, C_t, C_w, R_t and d_0, as the coil diameter, d, and shield diameter, D, which maximise the Q factor. Figure 5.7 shows a plot of Q_{large} vs d_0 for three traps of $C_t = 5$ pF and $R_t = 5$ Ohm, $C_t = 20$ pF and $R_t = 15$ Ohm, $C_t = 50$ pF and $R_t = 15$ Ohm all for a resonant frequency of $\omega_0 = 2\pi \times 10$ MHz. There is an asymptotic increase to higher Q factors for large values of d_0. Even for high resistance, high capacitance traps modest Q factors of ≈ 100 can be achieved; however this requires the

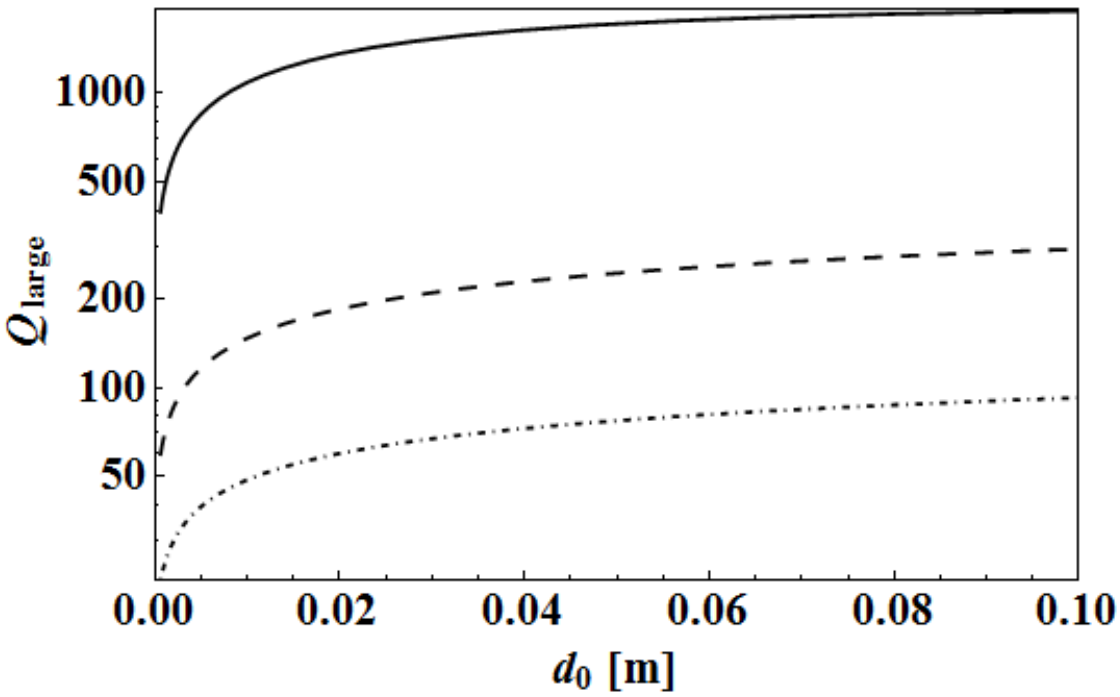

Figure 5.7: Q factor for values of d and d/D that maximise the Q factor for varying wire diameter, d_0, for traps D (solid), H (dashed) and I (dot-dashed) from table 5.1 at $\omega_0 = 2\pi \times 10$ MHz

coil to be formed from a thick rod. The upper limit to d_0 will result from an intersection of the limits that the coil height must be larger than the coil diameter, $b/d \geq 1$, and the coil diameter must be larger than the wire diameter, $d > d_0$. Increasing d_0 will increase the Q factor but will also increase the size of the resonator. It can be seen in figure 5.8 how the shield diameter required for Q_{large} (solid line) rapidly increases with d_0. However, for a Q factor 90% of Q_{large}, $Q_{90\%}$, a smaller shield diameter can be used. The minimum D for $Q_{90\%}$ is shown in figure 5.8 (dashed line). It is clear that making a resonator with a Q factor of $Q_{90\%}$ can reduce the size required for the resonator.

When designing a helical resonator for a specific experiment it is useful to examine contour plots of the Q factor as a function of coil diameter, d, and the ratio of the coil diameter to the shield diameter, d/D, as shown in figure 5.9 and 5.10. Using these plots it is possible to choose values of d and d/D that will optimise the Q factor for a set of parameters. These plots can be obtained using the parameters for ω_0, C_t, C_w, R_t for a given experiment and choosing values of d_0, τ and measuring or estimating R_j. The Q factor $Q(d, d/D)$ can be obtained by calculating:

$b(d, d/D)$ - The coil height - by using equation 5.26, K_{Cs} & K_{Lc} from equation 5.24 &

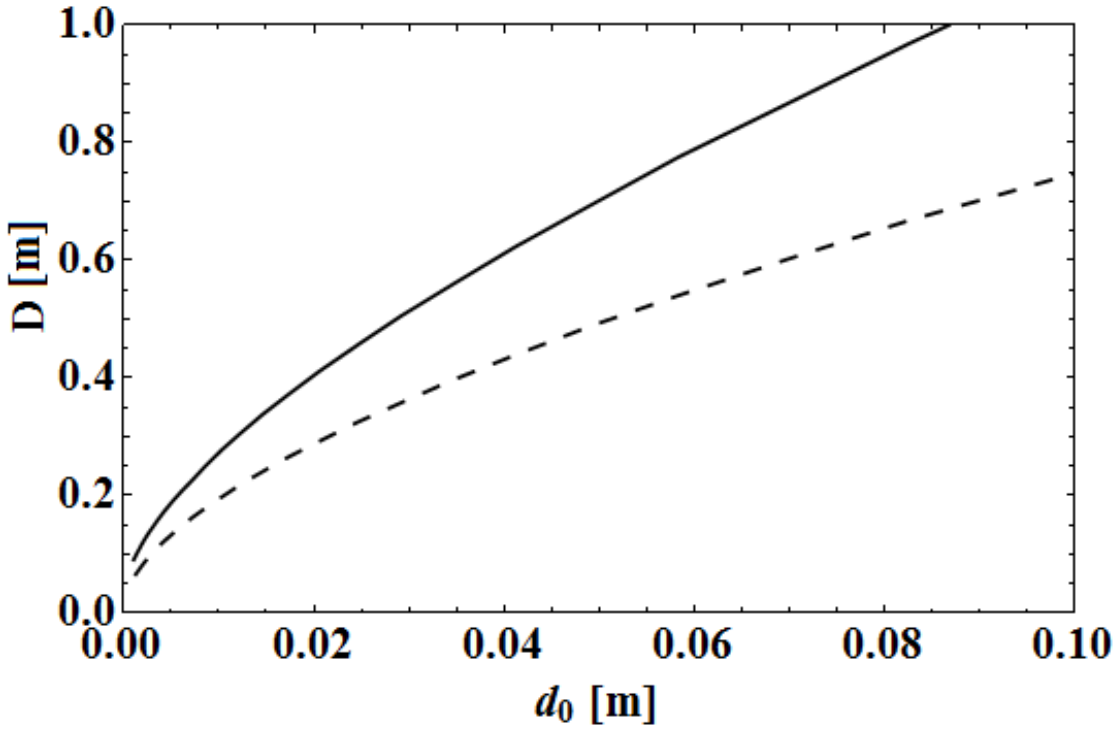

Figure 5.8: D vs d_0 for the D value that achieves a Q factor of Q_{large} (solid line) and the minimum D value that achieves a Q factor of $Q_{90\%}$ (dashed line) for trap D from table 5.1 at $\omega_0 = 2\pi \times 10$ MHz

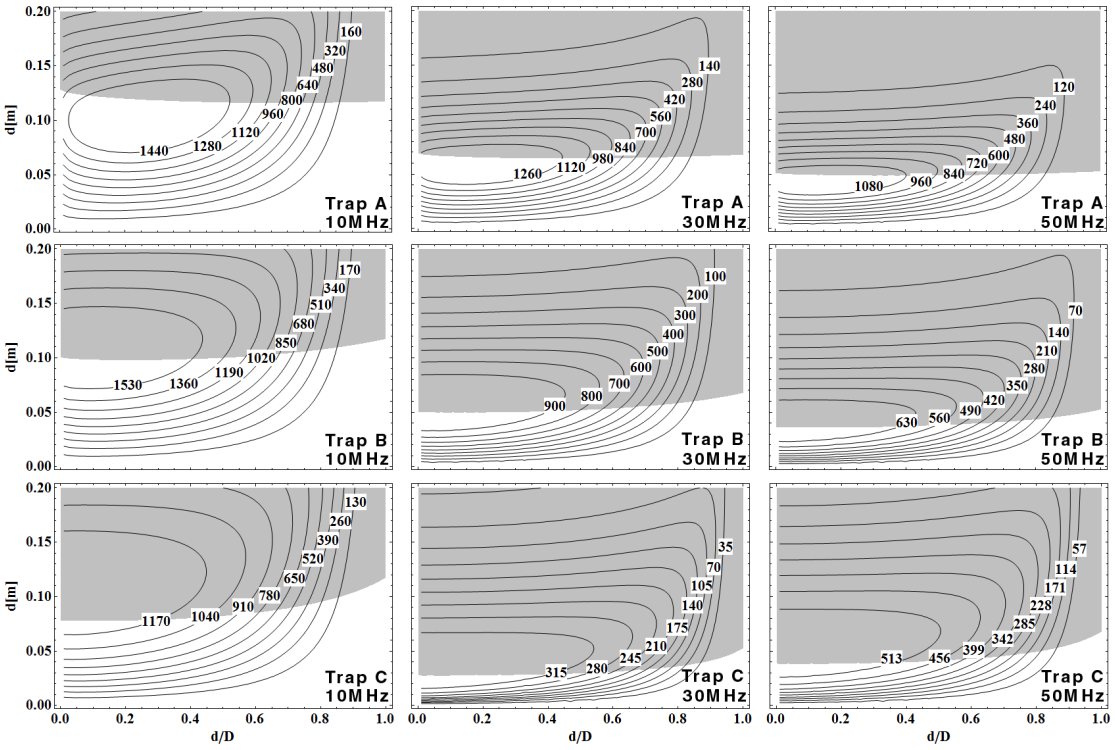

Figure 5.9: Contour plots for traps A, B and C (specifications in table 5.1) shown for operation frequencies of $\omega_0 = 2\pi \times 10$ MHz, $\omega_0 = 2\pi \times 30$ MHz and $\omega_0 = 2\pi \times 50$ MHz. The grey areas indicate where $b/d < 1$ therefore invalidating the theory.

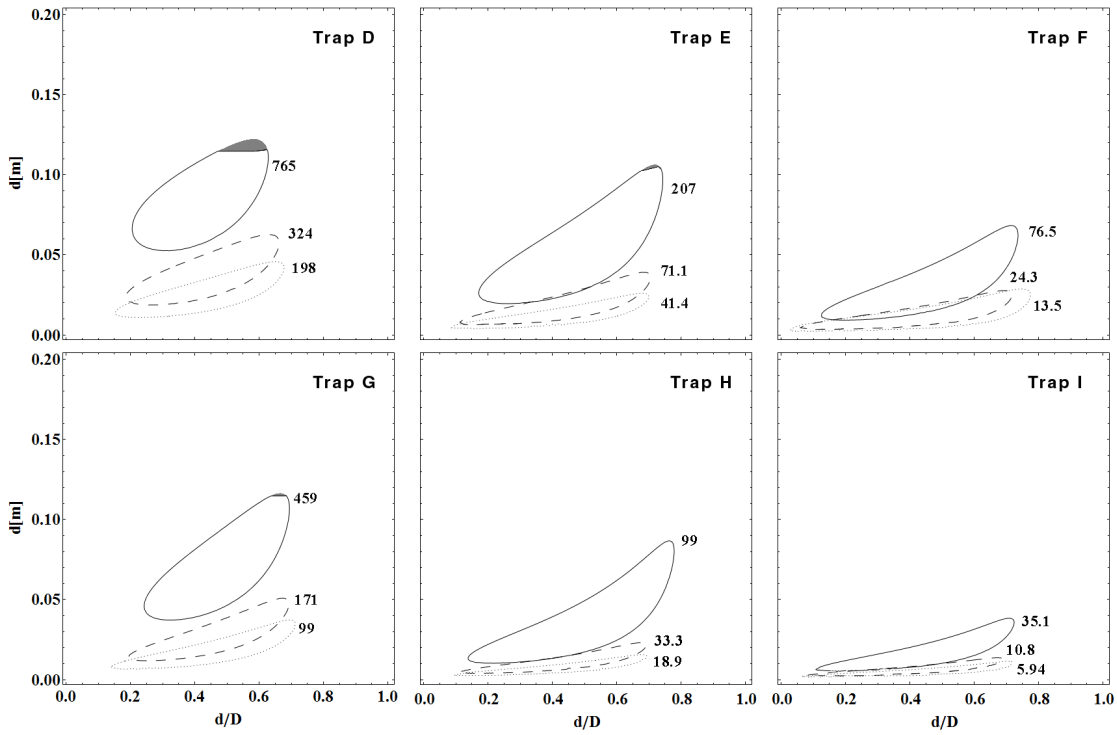

Figure 5.10: Contour plots showing $Q_{90\%}$ for each set of parameters corresponding to traps D to I from table 5.1 for operating frequencies of $\omega_0 = 2\pi \times 10$ MHz (solid lines), $\omega_0 = 2\pi \times 30$ MHz (dashed lines) and $\omega_0 = 2\pi \times 50$ MHz (dotted lines). The grey areas indicate where $b/d < 1$ therefore invalidating the theory. The value of $Q_{90\%}$ is indicated next to the contour line.

5.25 and K_{cb} & K_{cd} from the approximation for the coil capacitance.

$C_s(d, d/D)$ - The coil to shield capacitance - by substituting $b(d, d/D)$ into equation 5.24

$C_c(d, d/D)$ - The coil self capacitance - by substituting $b(d, d/D)$ into equation 5.24

$R_s(d, d/D)$ - The shield resistance - by using equation 5.33

$R_c(d, d/D)$ - The coil resistance - by using equation 5.32

$R_{ESR}(d, d/D)$ - The total resistance - by using equation 5.22

$L_c(d, d/D)$ - The coil inductance - by substituting $b(d, d/D)$ into equation 5.25

$Q(d, d/D)$ - The Q factor - by substituting $L_c(d, d/D)$ & $R_{ESR}(d, d/D)$ into equation 5.20

Figures 5.9 and 5.10 show contour plots for parameters corresponding to traps from table 5.1 for three resonant frequencies with $d_0 = 5$ mm and $\tau = 2d_0$. While larger values of d_0 would result in larger Q factors, and a larger Q_{large}, the values for d_0 and τ have been

chosen as they are typical for a hand wound coil, which will be discussed in detail later. Both plots feature a grey shaded region indicating where the condition that $b/d \geq 1$ (from equation 5.25) is not valid. Within this region the coil inductance will deviate from that predicted by equation 5.25 resulting in a deviation from the predicted ω_0 and Q factor. An expansion to this theory for short helical coils or wire loops could be implemented by utilising an appropriate equation for the inductance.

The experimental size restrictions will strongly dictate the achievable Q factor of the resonator. The values of d and d/D must be chosen to ensure that the shield diameter, D, and the shield height, B, will be within these size constraints, otherwise different values for d, d/D or d_0 will need to be chosen. Figure 5.9 for traps A to C show contour lines at a range of Q factors (as labelled) enabling the values of d and D to be chosen to maximise the Q factor for a given size constraint. Figure 5.10 for traps D to I shows contour lines of $Q_{90\%}$ for each set of parameters. The values of d and D can be chosen within the $Q_{90\%}$ contour line to optimise the Q factor (for a set of parameters ω_0, C_t, C_w, R_t, R_j, τ and d_0), while enabling a choice of d and D that minimises the size of the resonator.

For traps A, B and C figure 5.9 shows that higher Q factors are achieved when the coil diameter to shield diameter ratio, d/D, is close to 0. This corresponds to a large separation between the coil and the shield and hence a small shield capacitance. At $d/D = 0$, the shield diameter, D, would be infinite and the shield capacitance would be zero, indicating the resonator is dominated by the trap capacitance. However, it can be seen in figure 5.10 that Q factors of $Q_{90\%}$ can be achieved at values of d/D of order 0.5 with larger trap capacitance enabling larger ratios and hence a smaller shield diameter D and higher shield capacitance.

While figures 5.7 and 5.8 show that at large values of d_0 high Q factors may be achieved at a given size constraint, the construction of such resonators needs to be taken into account. In order to construct a resonator without specialist machinery, a wire diameter of approximately 5 mm is recommended. This wire size is sufficiently rigid not to be susceptible to mechanical vibrations, while being flexible enough when heated to be wound by hand into a coil. This can be achieved by winding the wire around a tube with notches cut into it to help align the wire to a constant winding pitch. The size of the resonator can be reduced by using a small winding pitch, however, a minimum winding pitch of $\tau = 2d_0$ is recommended when winding by hand in order to keep the error in the winding pitch small. A higher Q factor could be achieved by using $d_0 = 10$ mm, however, this would be hard to wind by hand, which can result in large errors in the winding pitch.

Coils can be constructed using large diameter wire but may require the use of specialist machinery. It should be noted that coils could be constructed from tubular material as current is only carried on the skin of the metal, however, this could affect the inductance of the coil. Similarly a rectangular cross-section wire could be used to form a coil or formed by cutting a tube into a coil. In order to predict ω_0 and the Q factor reliably equation 5.25 may need to be replaced with an expression for the inductance suitable for the desired geometry.

To summarise:

- A highly conducting material should be used to construct the resonator (for example copper).
- The coil wire should be made reasonably thick to provide mechanical stability and reduce coil resistance. If winding the coil by hand a wire on order of $d_0 \approx 5$ mm is suggested.
- The winding pitch should be as small and uniform as possible. If winding the coil by hand a minimum of $\tau \sim 2d_0$ is recommended.
- A contour plot of $Q(d, d/D)$ can be used to determine appropriate parameters for d and D within size constraints.
- The coil height is calculated from equation 5.26.
- The coil height must be greater than the coil diameter for equation 5.25 to be valid.
- The shield height B should be $b + D/2$.
- The coil and shield should be connected as close to the vacuum system as possible.
- Any solder joints made should be of low resistance.

5.4.2 Case study

Resonator construction and measurement

It will now be shown how a resonator for a typical ion trap experiment can be built without the need for specialist equipment. Following this a discussion on how the resonant frequency and Q factor can be measured, while ensuring impedance matching between the RF source and the resonator will be presented.

Table 5.1: Specifications of traps used for figures 5.9 and 5.10

Trap	Resistance Ohm	Capacitance pF
A	0.1	5
B	0.1	20
C	0.1	50
D	5	5
E	5	20
F	5	50
G	15	5
H	15	20
I	15	50

The coil can be wound by hand by using an annealed copper wire of diameter, $d_0 \approx 5$ mm. The copper can be annealed by heating with a blow torch in order to give increased flexibility. Once cooled, the copper can be wound, which will work harden the copper, creating a rigid coil. To ensure all the turns are equally spaced, the copper should be wound around a tube of diameter, $d - d_0$, with notches cut into the tube to align the wire when winding.

Once the coil is constructed it should be placed centrally inside the shield in order to minimise the coil to shield capacitance C_s. To ensure this, it must be clamped in place at the end of the coil before soldering the coil to a BNC bulkhead located in the shield as shown in figure 5.12. This clamping must be kept in position until the joint to the BNC is solid enough to support the coil on its own. This BNC bulkhead can be used to electrically connect the coil to the shield by connecting a BNC shorting cap. The ground rod is connected in the same way, although to the lower BNC bulkhead shown in figure 5.12. The ground rod must exit the resonator (as shown in figure 5.11) without coming into contact with conducting material. The ground rod and main coil can be held in place with the use of a non-conducting mesh, as shown in figure 5.11, to reduce the mechanical stress applied to them from connection to a vacuum feed-through or other similar load.

The antenna coil used to couple the radio frequency source to the resonator can be constructed out of 1.5 ± 0.5 mm wire and wound into 3 turns with a winding pitch of 10 ± 1 mm and diameter of 33 ± 1 mm. This, however, should be varied in order to match the impedance of the resonator to the source, as described in figures 5.3 and 5.4 and

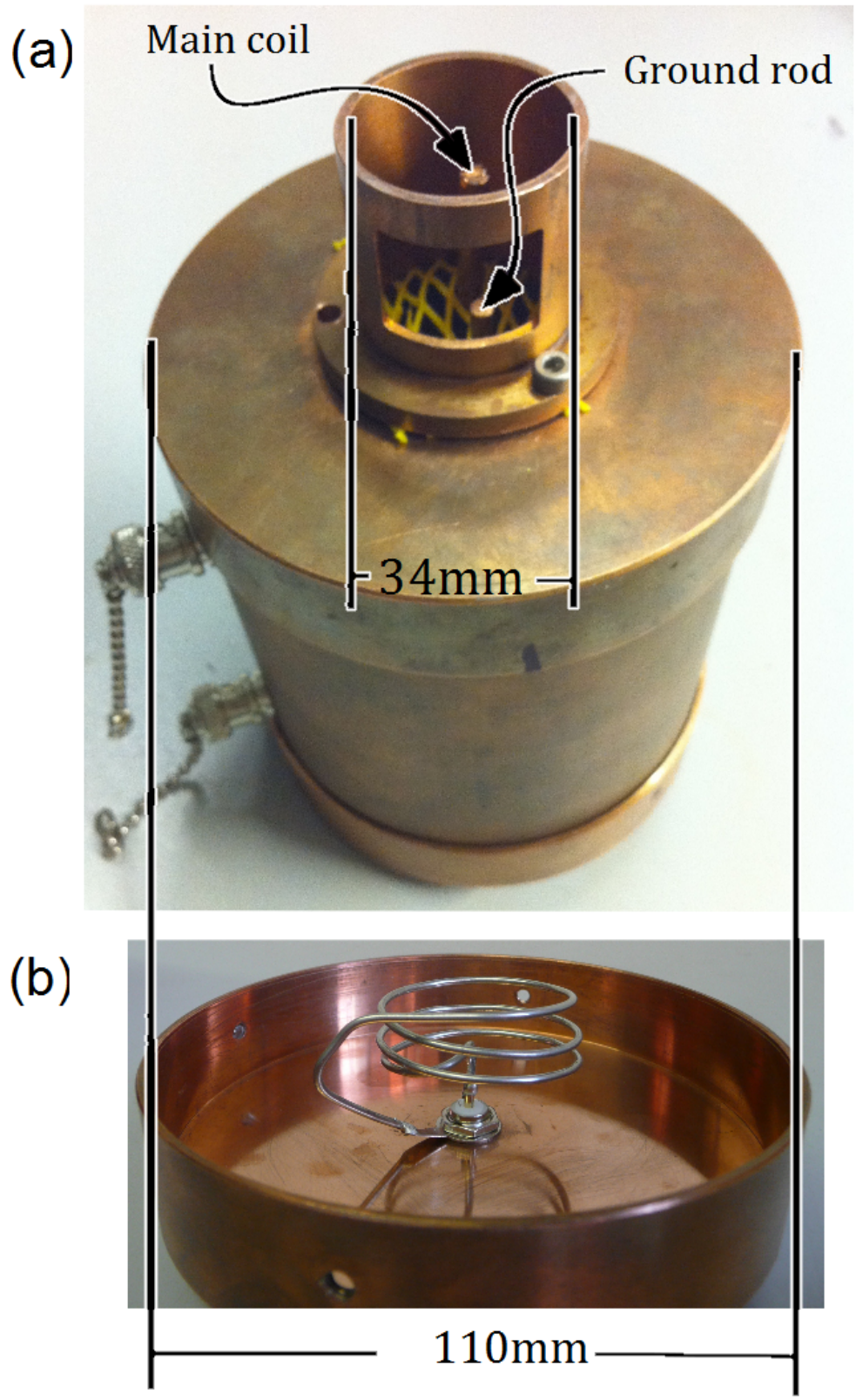

Figure 5.11: (a) Picture showing the bottom end cap including the top hat used to connect the resonator to a vacuum feed-through (in this case Kurt J. Lesker: EFT 0523052). The main coil and ground rod can be seen exiting the resonator and are held in position by a plastic mesh. The window in the top hat provides access for connecting the main coil and ground rod to feed-through pins. (b) Picture showing the top end cap and antenna coil (shown in further detail in figure 5.1).

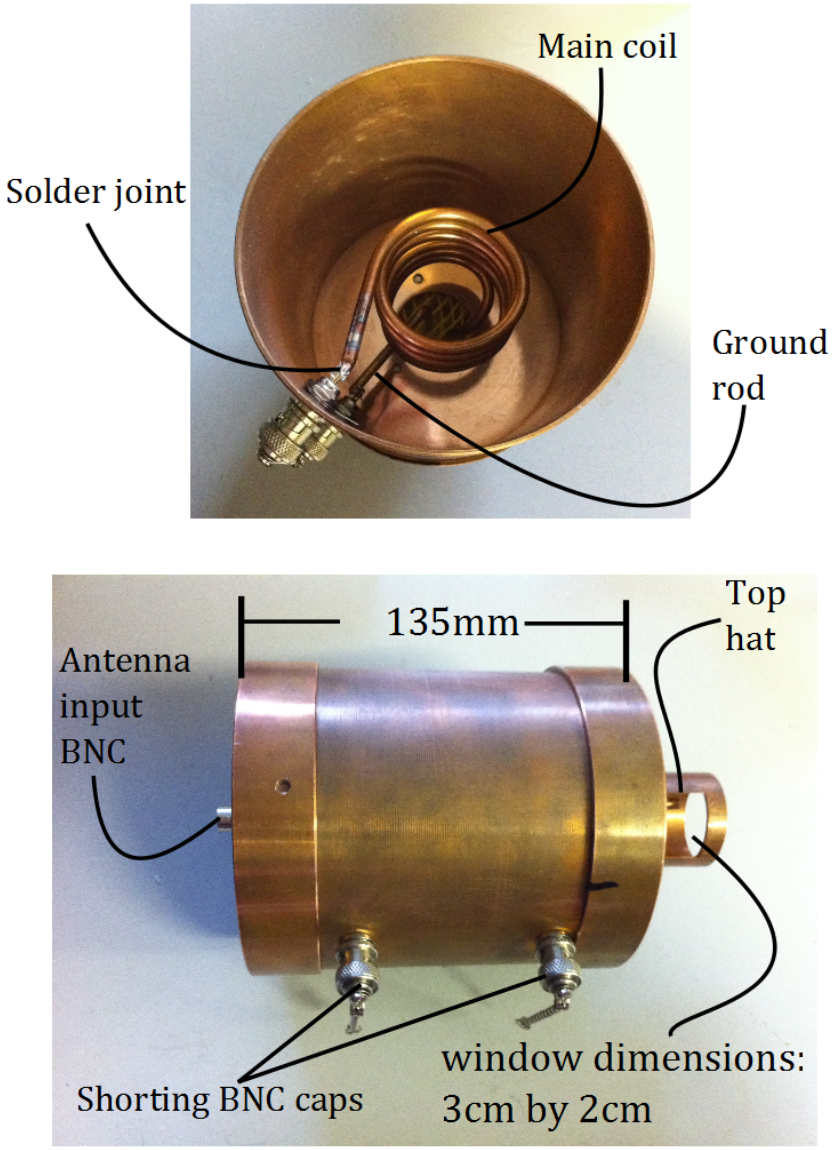

Figure 5.12: (a) Picture showing a coil and location of the solder joint used to make an electrical connection to the shield. This is done with the use of a BNC bulkhead located at a distance $\frac{D}{4}$ from the top of the shield where D is the diameter of the shield. The grounding rod is also shown. (b) Picture showing a fully constructed resonator. The top hat is shown on the bottom end cap and is designed to fit around a vacuum feed-through (in this case Kurt J. Lesker: EFT 0523052) which connects the main coil and grounding rod to the ion trap. A window is cut into the top hat to allow the connection between the feed-through and the main coil and grounding rod to be made. The top end-cap shows the BNC connection to the antenna coil, this is where the RF signal is applied to the resonator.

equation 5.12. To measure the resonant frequency of the resonator, a directional coupler (Mini Circuits: ZDC-20-3) should be placed between the output source port and the RF input port of a spectrum analyser's tracking generator (Agilent: N9320B) as shown in figure 5.13. Alternatively, the spectrum analyser can be replaced by an RF source and an oscilloscope, as shown in grey in figure 5.13. The resonator should be connected to the directional coupler and RF source via the end-cap that hosts the antenna coil shown in figure 5.1. Using the experimental set up shown in figure 5.13 the resonant frequency results in a minimum in the spectral response of the reflected signal detected by the spectrum analyser. The pitch and diameter of the antenna coil should be altered until less than 5% of the applied radio frequency signal is reflected back to the signal generator from the resonator when on resonance. The Q factor of this resonance is simply measured by dividing the resonant frequency, ω_0, by the full width of the resonance at $1/\sqrt{2}$ of the maximum voltage reflection, $\delta\omega_0$:

$$Q = \frac{\omega_0}{\delta\omega_0}. \tag{5.38}$$

Using the method described here it is possible to measure the resonant frequency and Q factor of a resonator when the ion trap is unconnected, which corresponds to R_T and C_T being equal to infinity and zero respectively. The resonant frequency and Q factor of a resonator with an ion trap applied across the output can then be measured by adding the required values of resistance and capacitance across the output of the resonator. The stray capacitance C_W created between the wires used to connect the trap resistance and capacitance can be reduced by keeping these wires as short and as separated as possible.

Experimental analysis of typical resonators

Two resonators were constructed with a range of parameters as described in table 5.2. The theoretical resonant frequencies of the resonators have been plotted in figure 5.14 as a function of the trap capacitance, C_t. The theoretical Q factor for these resonators can be seen in figure 5.15 plotted as a function of the trap capacitance, C_t, applied to the resonator. All these are plotted for typical trap resistances, R_t, of 0.1 Ohm, 1 Ohm and 10 Ohm, which is representative of the typical range over which the resistance of an ion trap can vary depending on what type of material and fabrication techniques are used.

Figures 5.14 and 5.15 show that the experimental measurement of the Q factor and resonant frequency over a wide range of trap loads is consistent with the theory described in this work. The Q factor of resonator A can be seen to be higher than that of resonator B as

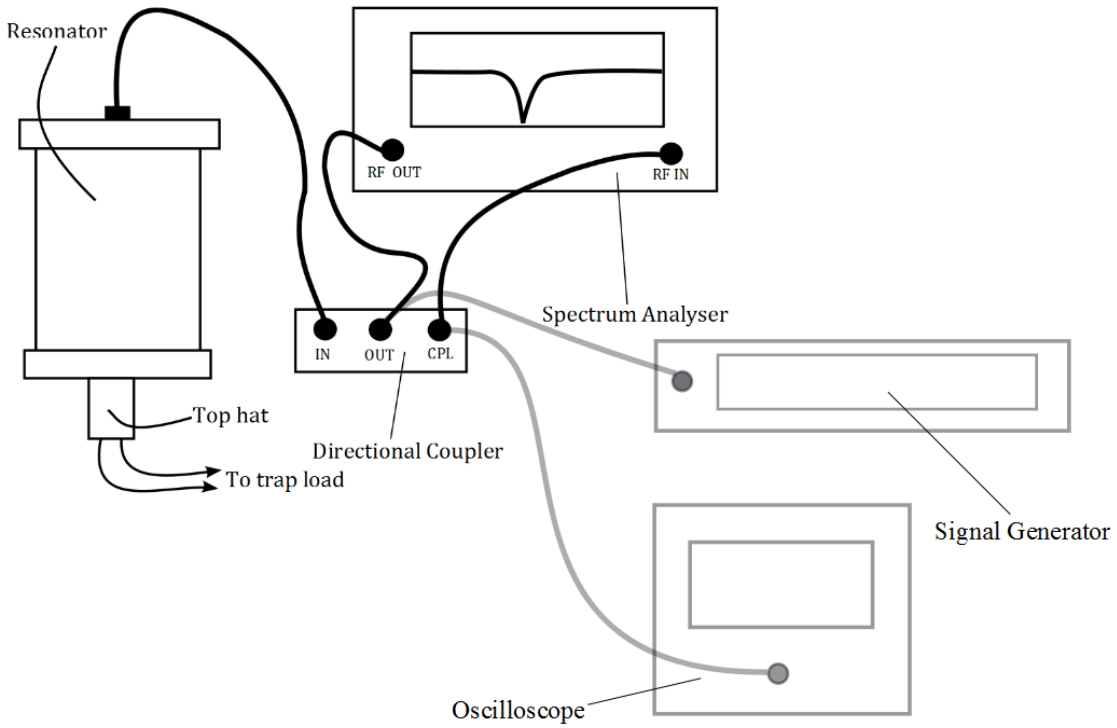

Figure 5.13: Experimental set up required to measure the resonant frequency, coupling and Q factor of a resonator. The resonator is connected to a spectrum analyser with a tracking generator via a directional coupler such that the reflected signal from the resonator is displayed on the spectrum analyser. Alternative equipment can be used and is shown in grey. This comprises of a signal generator and an oscilloscope.

Table 5.2: Specifications of the resonators. The Q factors and frequencies quoted are without the addition of an ion trap load.

Resonator	A	B
Shield diameter D [mm]	108±2	76±2
Shield height h [mm]	120±2	90±2
Coil diameter d [mm]	42±2	46±2
Coil wire diameter d_0 [mm]	5.0±0.1	5.0±0.1
Winding pitch τ [mm]	9±1	15±1
Number of turns N	6.75±0.25	4.5±0.25
d/D ratio	0.4±0.2	0.6±0.2
Predicted frequency [MHz]	64^{+8}_{-6}	78^{+10}_{-7}
Measured frequency [MHz]	67 ± 0.5	83 ± 0.5
Predicted Q	1970^{+252}_{-374}	689^{+46}_{-115}
Measured Q	2176±200	631±60

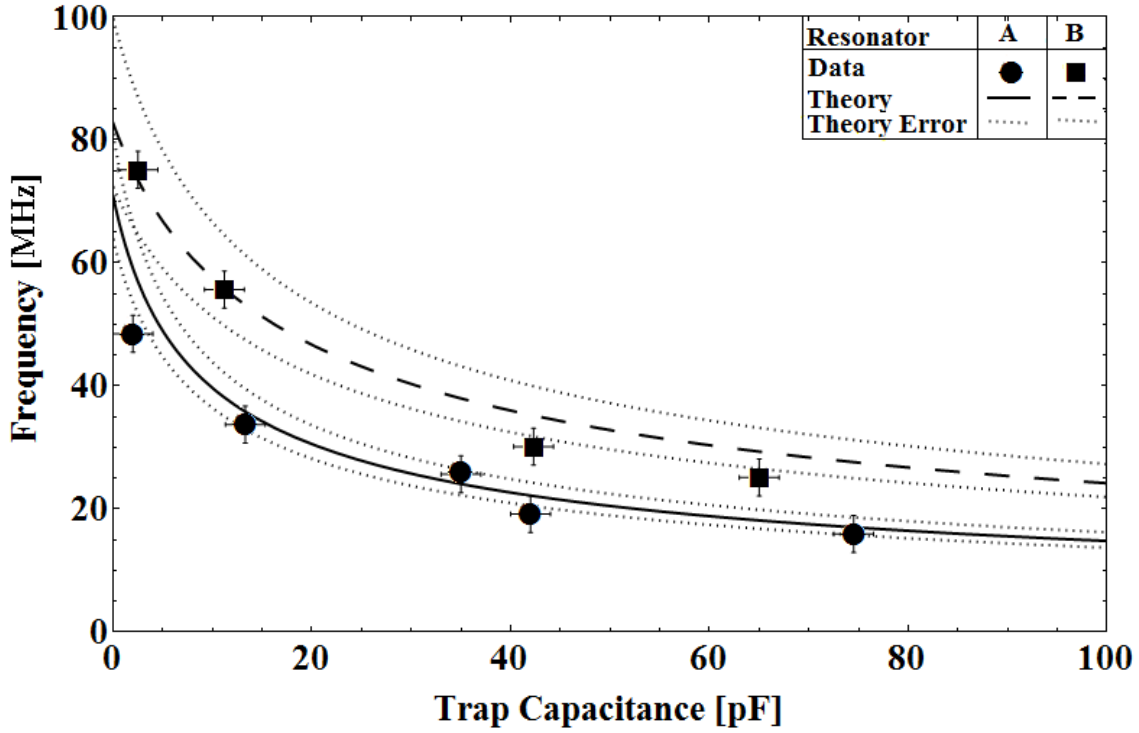

Figure 5.14: The resonant frequencies of resonator A (circles) and resonator B (squares) are shown as a function of the trap capacitance they are attached to. The dashed curves represent the error on this calculation based on the design errors stated in table 5.2. The resonant frequencies were measured for a resistance of 1 Ohm, however, we note that they are actually independent of the resistance.

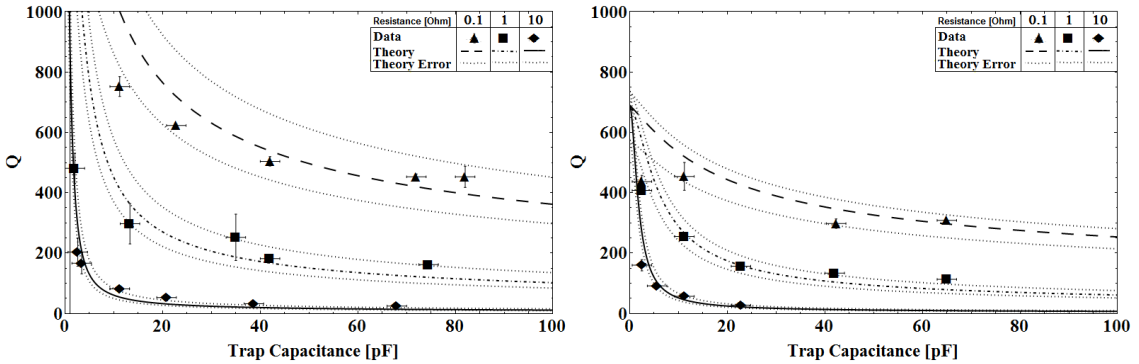

Figure 5.15: The Q factor of resonator A (left) and resonator B (right) are shown as a function of the trap capacitance. The dashed curves represent the error of the calculation based on the design errors stated in table 5.2. The Q factor was measured for different resistance loads shown by the triangles (0.1 Ohm), squares (1 Ohm) and diamonds (10 Ohm).

Table 5.3: Specification of resonator used for κ measurements

Resonator	C
Shield diameter, D [mm]	76 ± 1
Shield height, B [mm]	105 ± 1
Coil diameter, d [mm]	52 ± 2
Coil wire diameter, d_0 [mm]	4.0 ± 0.1
Winding pitch, τ [mm]	7 ± 3
number of turns, N	$7\frac{3}{4}$

it possesses specifications which are either optimum or nearer to optimum than resonator B (depending on the trap load applied). It can be seen that although the resonator is not optimum for the various ion trap impedances, the Q factor may still be sufficient for many experiments. This shows that a new resonator does not necessarily have to be built if the trap is altered slightly.

5.5 Experimental measurement of κ

It was shown in section 2 that the voltage output of a resonator is given by $V_{rms} = \kappa\sqrt{PQ}$, where P is the power of the signal applied to the resonator, Q is the quality factor of the resonator and $\kappa = (L/C)^{\frac{1}{4}}$. Here an experimental measurement of the value of κ in an ion trap experiment will be made. The value of κ is required in order to calculate the voltage applied to the ion trap electrodes used to create a trapping potential. A resonator, described in table 5.3, was electrically connected to an ion trap and vacuum system with a capacitance and resistance measured to be 17 ± 2 pF and ≈ 0.1 Ohm respectively. The resonant frequency and Q was then measured with this additional load to be $\omega_0 = 2\pi \times 21.895 \pm 0.010$ MHz and $Q = 477 \pm 28$ respectively.

A single $^{174}Yb^{+}$ ion was trapped in the electric field created by the trap electrodes with the resonator supplied with 1.0 ± 0.1 W at its resonant frequency. The secular frequencies of the ion under these conditions were then measured and a boundary element method (BEM) model of the trapping field was used to determine the RF voltage required to

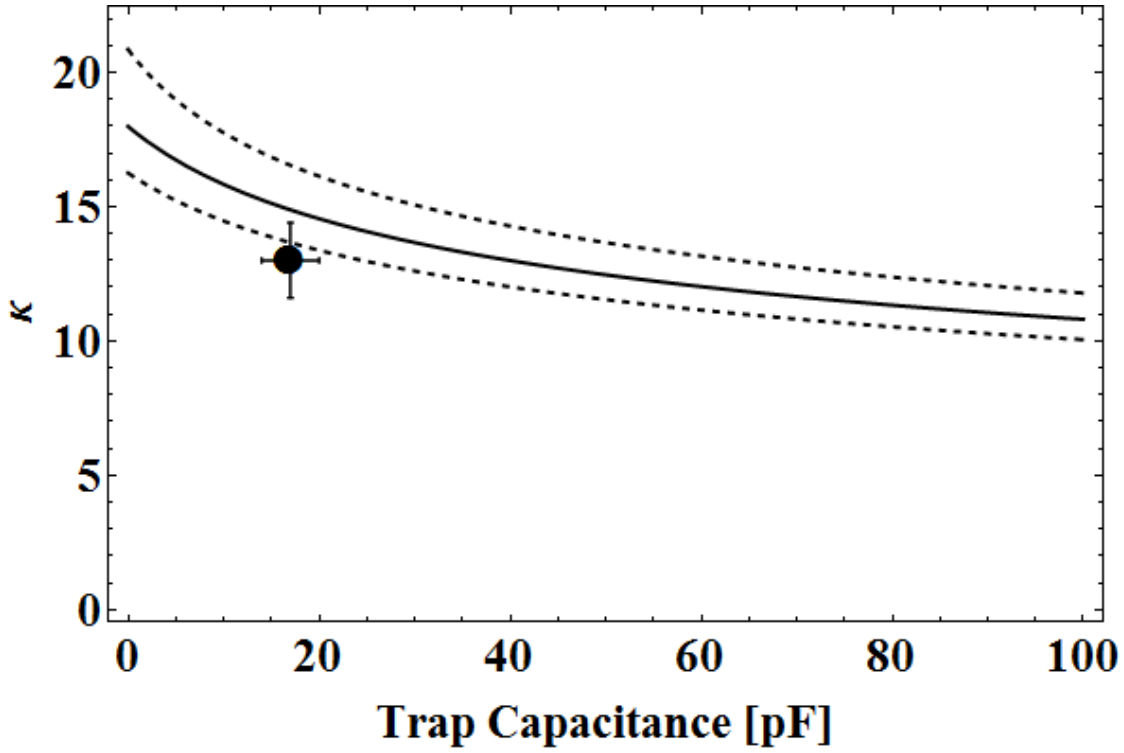

Figure 5.16: The factor κ from equation 5.5 is plotted as a function of the the trap capacitance for the resonator described in section 5.5. The thick curve shows the value of κ with the dashed curves showing the error on this calculation due to the uncertainty of the resonator specifications and its imperfections. The data point shown is for the resonator attached to a 17 ± 3 pF ion trap and vacuum system.

create such a field. This voltage was found to be 400 ± 20 V which, when used in equation 5.5 along with the power used to trap the ion, results in a κ of 12.9 ± 1.4. This result is compared with the theoretical prediction of κ (from equation 5.5) in figure 5.16. It is to be noted that the value of κ depends on the impedance of the ion trap attached to the resonator.

5.6 Conclusions

A detailed study of helical resonators for the use in applying high voltages at radio frequencies to ion traps has been carried out. This has been done by modelling the resonator as a lumped element circuit along with a detailed discussion on the losses present in helical resonators connected to ion trap loads in order to arrive at an expression for the Q factor and resonant frequency, ω_0. It has been shown how a resonator and load can be impedance matched to a frequency source by simply adjusting the physical parameters of an antenna coil which inductively couples the two. A general expression for the voltage output of the

resonating system has been derived in terms of the system's Q factor, input power, P, and a κ factor which is a function of the system's capacitance and inductance. The value of this factor has been experimentally confirmed using a single trapped ion. The theory described in this work has been confirmed by fabricating two resonators and measuring their Q factor and resonant frequency, ω_0, for a range of different trap loads (C_T from 2 pF to 85 pF and R_T from 0.1 Ohm to 10 Ohm).

A detailed design guide has been presented showing how a helical resonator can be designed which provides the highest Q factor achievable for a desired resonant frequency within the constraints of a particular experiment. Although high Q factors are currently routinely achieved in the range of $\approx$ 50 to $\approx$ 500 [69, 70, 71], depending on the trap used, it should be possible to produce resonators with Q factors 2-10 times greater using the method described in this work. Producing a resonator with an optimised Q factor allows the application of high voltages with optimised filtering. This will result in less noise injected into the system which could reduce anomalous heating of the trapped ions. The application of high voltages can give larger trap depths, leading to longer trapping lifetimes, and increased secular frequencies. This technology plays a significant role in many ion trapping experiments and should allow for progress in a variety of fields that require trapped ions or high radio frequency voltages.

Chapter 6

An imaging system design for ion trap experiments

6.1 Introduction

This chapter will describe the optics, photon detection devices and layout of the imaging system used to image single ions. In particular different types of photon detection devices will be compared in terms of signal to noise ratios with a view to illustrating which device provides the best signal to noise ratio under different experimental conditions.

6.2 Requirements of imaging system

The imaging system described in this thesis was required to be flexible enough to provide imagining via a photo-multiplier tube (PMT) and charged coupled device (CCD) for two separate ion trapping experiments without the need to re-image or change optical elements. It was also required to switch quickly and simply between the PMT and CCD imaging options. The basic design idea (shown in figure 6.1) to enable this simple switching was to build two separate tube systems to house the individual experiments imaging optics and then combine them with the use of a flipper mirror, allowing the switching between the two systems. A flipper mirror can then be used to switch between the PMT and CCD. By including separate arms for each experiment the optical elements can be adjusted for one system without affecting the other. Each individual arm can then be controlled by an xyz stage giving them the freedom to be manoeuvred in three dimensions allowing imaging of various parts of the trap.

To provide successful imaging of ions in a trap the optics used must be able to resolve

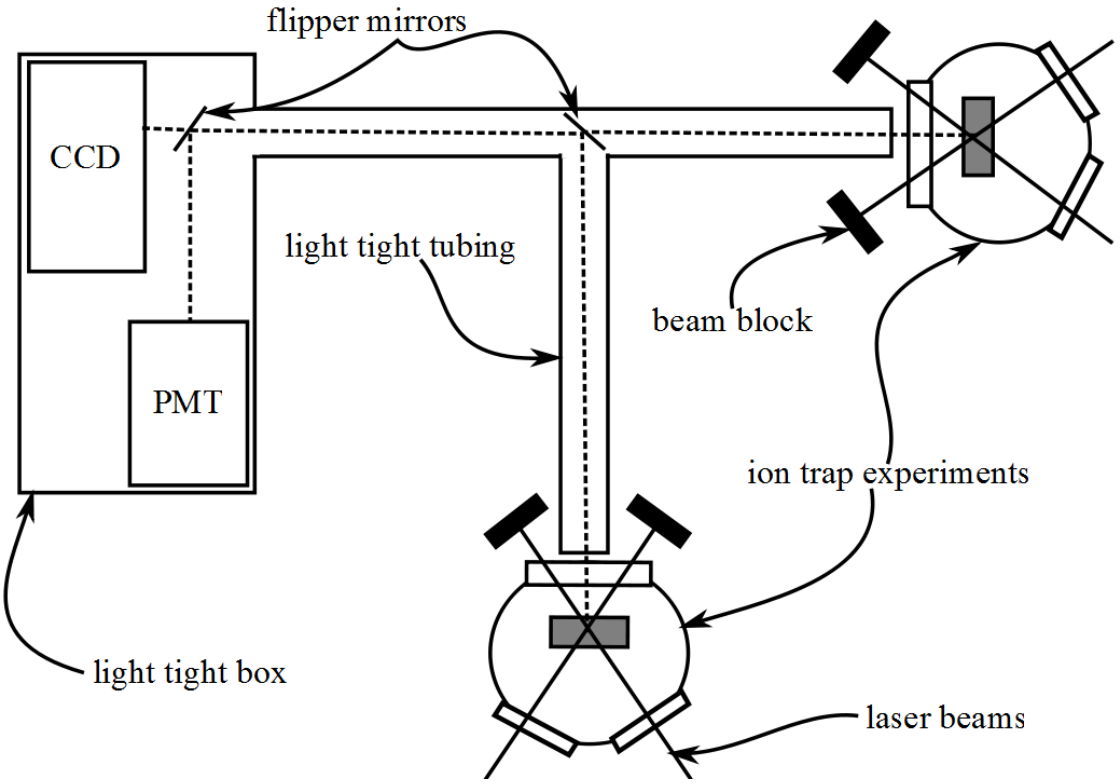

Figure 6.1: Basic imaging system layout. Shown are the CCD, PMT and two separate ion trap experiments. Flipper mirrors are present to allow imaging flexibility between each experiment and for switching between the CCD and PMT detection options.

multiple ions confined in the trap's oscillating electric field. The distance that two ions are separated by in a trap can be calculated by equating the restoring force felt by an ion in a trapping field $F_{trap} = m\omega^2 r$ and the Coulomb repulsion between the two ions $F_{coulomb} = e^2/(4\pi\epsilon_0 r^2)$ and solving for the distance between the ions r

$$r = \left(\frac{e^2}{4\pi\epsilon_0 m\omega^2}\right)^{\frac{1}{3}}, \tag{6.1}$$

where ϵ_0 is the permittivity of vacuum, ω is angular secular frequency of the trap in the direction that the ions are separated, m is the mass of the ion and e is the charge of one electron. The separation of two Yb^+ ions in a trapping potential can now be calculated as $r = 2.7\ \mu m$, using a typical secular frequency of $\frac{\omega}{2\pi} = 1$ MHz. It can be concluded from this that the imaging system must at least be able to resolve two objects separated by this distance.

6.3 The imaging optics

The optics used in the imaging system consists of a triplet lens formed from three separate lenses placed in close proximity and a doublet lens formed of two lenses. This section will describe both of these optical elements and explain how and why they are used for the purpose of imaging single atomic ions. Triplet and doublet lenses are used in the imaging system to reduce the effect of spherical aberrations on the produced image. Aberrations are caused by deviations in a real optical path length and a theoretical path length. Several types of aberrations can occur in optics including coma, spherical and chromatic. Chromatic aberration is caused by light of differing wavelengths focussing to different distances, and is not an issue in this system as we are only interested in the 369 nm light emitted from the ion. Coma is caused by imperfections in lenses resulting in off-axis sources being focused to different distances. Again, this is not considered an issue in this system as the ion(s) is (are) located close to the optical axis. Spherical aberration is due to the deviation from first order theory of light rays entering a lens from far off the optical axis, which can be considered to be the case as photons are emitted in all directions by the ion(s). By using a triplet lens the angle of the collected light is reduced and so reduces the effect of spherical aberration.

6.3.1 The triplet lens

The first optical element used in the imaging system is the triplet lens. This consists of three separate lenses placed next to each other and contained within the same housing.

Two triplet lenses (Special Optics: 54-17-29-369 and CVI: UVO-20.0-10.0-355-532) were found which provide the required resolution at a focal distance large enough to be placed outside the vacuum system. The Special Optics lens provides a resolution of 0.85 μm and the CVI lens 1.13 μm enabling them both to be able to resolve single ions separated by the coulomb interaction in a typical ion trap. The specifications of the two lenses are shown in table 6.1.

Table 6.1: Specifications of the two triplet lenses

Lens	Focal length [mm]	Back focal length [mm]	Aperture diameter [mm]	F-number	Magnification
CVI	20	14.8	10	2.1	-19.2
Special Optics	30	21	17	1.7	-17.5

To conclude which of the two triplet lenses would be used in the experiment's imaging system the number of photons collected by each triplet was calculated and compared. To do this, first, an expression for the number of photons collected by an aperture with a diameter, D, at a distance, l, from an ion emitting photons spontaneously in all directions should be derived. The photon flux density at a distance l from the ion is given by

$$F = \frac{\gamma}{4\pi l^2} \tag{6.2}$$

where γ is the number of photons emitted from the ion per second and $4\pi l^2$ is the surface area of a sphere with a radius equal to that of the ion-aperture distance. The number of photons that will be collected by the aperture can then be simply calculated by multiplying the photon flux, F, from equation 6.2 by the surface area of the aperture,

$$\gamma_i = \left(\frac{\gamma}{4\pi l^2}\right)\left(\frac{\pi D^2}{4}\right) = \frac{\gamma D^2}{16 l^2} \tag{6.3}$$

As there are other optical elements present in the system before the photon detection devices it is important to arrive at an expression which gives the number of photons incident on these devices, ϕ_i. This can be found by multiplying equation 6.3 by a transmission coefficient, T, which describes the transmission efficiency of the optics in the system.

$$\phi_i = \frac{\gamma D^2 T}{16 l^2} \tag{6.4}$$

By modelling the two triplet lenses in OSLO [1] it was found that the distance, l, the CVI and Special Optics lenses had to be from the ion to provide a diffraction limited image was 16.99 mm and 23.54 mm respectively. By estimating the transmission coefficient as $T = 0.9$ the number of photons collected by the two lenses per second can now be calculated in terms of the number of photons emitted by the ion(s) per second, γ. The number of photons collected by the CVI triplet per second is

$$\phi_{cvi} = 0.019\gamma \tag{6.5}$$

and the number collected by the Special Optics triplet is

$$\phi_{so} = 0.029\gamma \tag{6.6}$$

From equations 6.5 and 6.6 the proportion of photons emitted from the ion(s) collected by the triplet is greater in the Special Optics lens compared with the CVI triplet, however, these photons will be spread out in an Airy pattern formed by the diffraction of the light through the triplet. It is, therefore, required to define the better triplet lens in this set-up as the one which collects the most photons per second in the central Airy ring. The image pattern created by the triplet lenses was modelled in OSLO and the results are shown in figures 6.7 and 6.8.

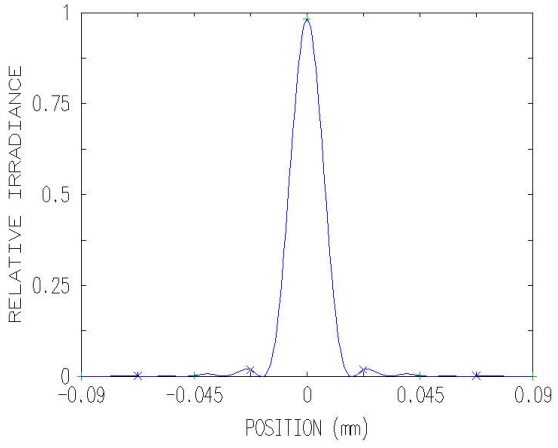

Figure 6.2: OLSO simulation of the magnified pattern created by the CVI triplet lens.

The OSLO simulations of the image patterns created by the two lenses show that the CVI lens diffracts 98.32% of the collected photons into the central Airy spot whereas, the Special Optics lens focusses 75.8% into the central spot. Figures 6.7 and 6.8 show the magnified image patterns of the respective triplet lenses. These percentages can then be

[1] http://www.sinopt.com/

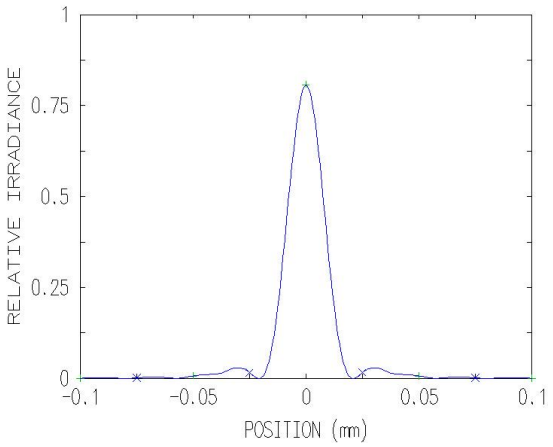

Figure 6.3: OLSO simulation of the pattern created by the Special Optics triplet lens.

used to calculate the number of photons collected in the central Airy spot per second by the CVI ($\phi_{CVIpeak}$) and Special Optics (ϕ_{SOpeak}) triplet lenses.

$$\phi_{CVIpeak} = 0.018\gamma \tag{6.7}$$

$$\phi_{SOpeak} = 0.022\gamma \tag{6.8}$$

Equations 6.7 and 6.8 show that, in the optical set-up used in this thesis, the Special Optics triplet will collect 2.2% of the ion's emitted photons, whereas, the CVI triplet will collect 1.8% of the emitted photons. It is for this reason that the Special Optics triplet was chosen to be used in the imaging optical set-up.

6.3.2 The doublet lens

A doublet lens is utilised after the triplet lens in order to allow an easy alteration of the overall magnification of the system by simply altering the two lenses. The total magnification of the system can be calculated by multiplying the magnification of the triplet, M_{tr}, with the magnification of the doublet, M_{du}

$$M_{total} = M_{tr}M_{du} = M_{tr}\frac{S_{2du}}{S_{1du}} \tag{6.9}$$

where S_{1du} and S_{2du} are the object and image distances of the respective lenses shown in figure 6.4. The triplet magnification, M_{tr}, cannot be calculated using its image and object distance like the doublet lens magnification as the combination of the three lenses means the thin lens approximation cannot be made. Instead the triplet lens magnification is calculated by using an OSLO simulation.

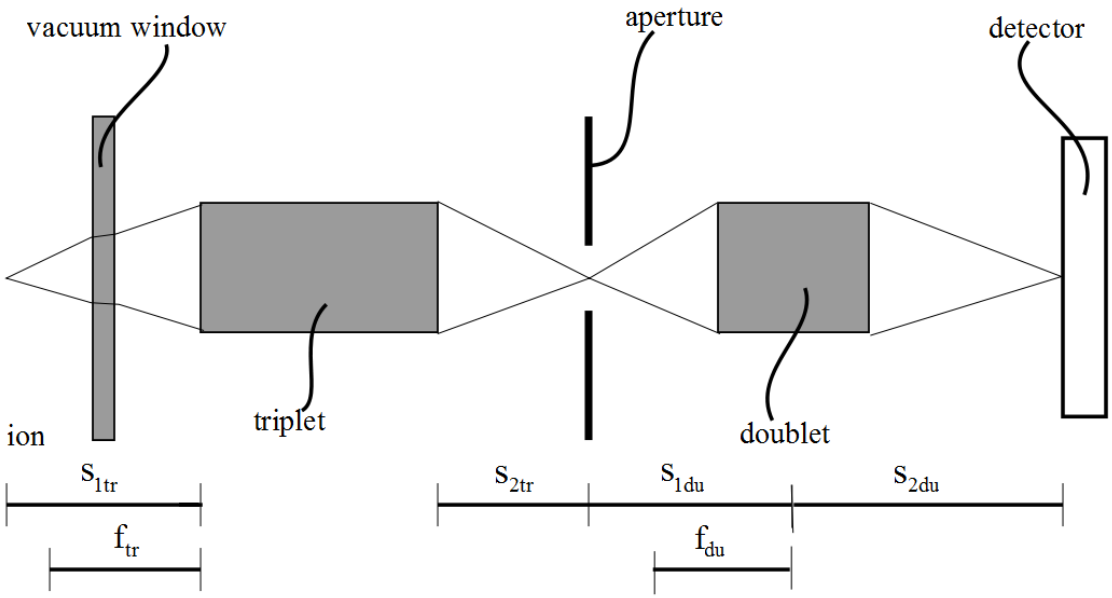

Figure 6.4: Basic ray trace diagram of the triplet and doublet showing relative positions of the vacuum window, aperture and detector.

To determine what object and image distances should be used for the doublet the overall magnification, M_{total}, the triplet magnification, M_{tr}, and the focal length of the doublet, f_{du}, must be calculated. The triplet magnification was given in the OLSO simulation of the triplet and for an object distance of 23.54 mm (corresponding to a diffraction limited ion image) the magnification was found to be $M_{tr} = -17.5$ producing an image distance of 549.7 mm. The total magnification can be calculated by determining how much larger the desired ion image size is compared to the diffraction limit of the triplet lens (1.13 μm). For example if an ion is required to cover 10 by 10 pixels (typical pixel sizes for example are 10 μm) then a magnification of ≈ 88.5 is needed to map the 1.13 μm diffraction limited ion onto the required 100 μm. By using a thin lens approximation the focal length of a doublet can be estimated using the focal lengths of the composite lenses, f_1 and f_2, by

$$f_{du} = \left(\frac{1}{f_1} + \frac{1}{f_2}\right)^{-1} \tag{6.10}$$

As the doublet consists of two thin lenses in very close proximity we can use the thin lens formula to relate its focal length to its object and image distances, S_{1du} and S_{2du} respectively

$$\frac{1}{f_{du}} = \frac{1}{-S_{1du}} + \frac{1}{S_{2du}} \tag{6.11}$$

which, when rearranged in terms of the doublets image distance, S_{2du}, gives

$$S_{2du} = \left(\frac{1}{f_{du}} - \frac{1}{S_{1du}} \right)^{-1} \tag{6.12}$$

It is important to note here that the minus sign in front of the doublet's object distance, S_{1du}, occurs due to the convention that a distance from the lens to the object is in the negative direction and a distance from the lens to the image is in the positive direction. Equation 6.12 can then be substituted into equation 6.9 and rearranged to give the required image distance of the doublet lens

$$S_{1du} = \left(\frac{M_{tr}}{M_{total}} - 1 \right) f_{du} \tag{6.13}$$

With this distance calculated the image distance of the doublet can then be calculated from equation 6.12.

6.3.3 Imaging optics set up

To construct the imaging system the Special Optics triplet lens was attached to one inch diameter lens tubing (Thor Labs: SM1L series) and the doublet lens mounted inside a non-rotating adjustable tube (Thor Labs: SM1ZM). An iris (Thor Labs: SM1D12SZ) was placed at a distance S_{2tr} (the triplets image distance) and a distance of S_{1du} from the doublet (the doublets object distance). This can then be used to cut out any stray light that may enter the system and focus to different points. For the experiments carried out in this thesis a doublet lens consisting of a 30 cm and a 20 cm focal length lens with an object distance of 18 cm and an image distance of 36 cm was used. This yields a total magnification of 35 when the triplet is placed 23.54 mm from the ion with a resulting image distance of 549.7 mm (the conditions required for the triplet to produce a diffraction limited image of the ion). Using this set-up an area of ≈230 μm by ≈230 μm is imaged onto the CCD or PMT.

Figure 6.5 shows a photograph of the constructed imaging system. The box housing the CCD and PMT is covered in a black cloth to further increase the light tightness of the box itself. A flipper mirror can be positioned inside the light tight box in the photograph that allows switching to a second vacuum system.

6.3.4 Imaging system set up examples

Due to the vacuum system's ability to house a range of different traps it is required to have the ability to alter the area over which the optics image. This can simply be done by

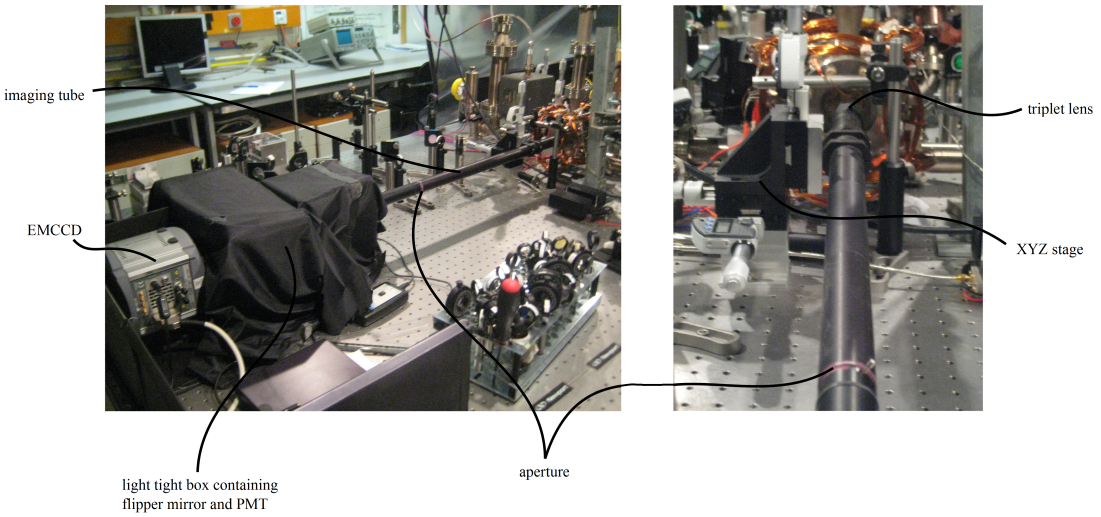

Figure 6.5: Labelled photo of constructed imaging system.

altering the doublet lens specifications (the individual focal lengths, object distance S_{1du} and image distance S_{2du}). Table 6.2 shows three different examples of doublet specifications which can be used to image a range of different areas. Firstly a 30 μm by 30 μm area is considered, where the ion is imaged to around 30 by 30 pixels. This type of imaging can be useful for minimising photons collected which have scattered off of electrodes as they are collected over a relatively small image area. The second case shows an example for a case imaging a 300 μm by 300 μm area. This can be useful for imaging multiple ions trapped over this area or to image shuttling of ions around a junction. The third case shows imaging for a 1000 μm by 1000 μm area which can be used to image ions and their surrounding trap structures (in symmetric traps) or shuttling around large junctions and ion arrays.

The required magnifications for the doublet lenses, M_{du}, in table 6.2 are calculated for imaging the desired area onto an 8 mm by 8 mm CCD array (Andor: iXon^{EM}+ 885). If a different array size is to be used the magnification of the doublet will have to be adjusted accordingly. As well as adjusting the doublet magnification depending on the CCD array, different individual doublet lenses can be used to reduce (or increase) the distances S_{1du} and S_{2du} (shown in figure 6.4) in order to fit the lens system in the experimental space available. A reduction in these lengths can be achieved by reducing the focal length of the doublet, given by equation 6.10. To achieve this one, or both, of the individual doublet lens focal lengths can be reduced.

Table 6.2: Examples of doublet specifications for three different imaging areas.

System	Imaged area [μm]	M_{tot}	M_{du}	Doublet lens focal lengths [cm]	S_{1du} [cm]	S_{2du} [cm]	Ion size [pixels]
1	30 by 30	280	-16	10 cm and 5 cm	3.5	56.7	30 by 30
2	300 by 300	$26\frac{2}{3}$	-1.5	20 cm and 30 cm	19.9	30.3	3 by 3
3	1000 by 1000	8	-0.45	20 cm and 40 cm	42.5	19.4	1 by 1

6.4 Photon detection devices

It is vitally important for many scientific applications to be able to collect and detect as many photons from a source as possible in order to achieve a good signal to noise ratio and, especially for low light applications, to be able to detect the source. In some cases it is required to detect single photons above the noise floor of the devices readout. There are three types of device which can provide the ability to detect and count single photons emitted from a source, an intensified charged coupled device (ICCD), an electron multiplication charge coupled device (EMCCD) and a photo-multiplier tube (PMT).

Charged coupled devices (CCDs) are arrays of photosensitive units (pixels) which, when exposed to incident photons, will generate, store and transfer electrons. The generated charge in the CCD array is directly proportional to the number of photons incident on the array. Due to the array nature of this type of device it is possible, via electronics and digitisation, to create an electronic form of the collected photons. In order for the device to do this the collected charge must be transferred to a readout amplifier, shown in figure 6.6. This is achieved by shifting the charged stored in each individual pixel down one row, by adjusting voltages which confine the charges to a particular pixel, resulting in the bottom row moving into the readout register. From this register the charge in each pixel can be sent through the readout amplifier and converted into an electronic signal which can be used to form a picture of the charge distribution.

6.4.1 The EMCCD

Electron multiplication CCD arrays (sometimes referred to as on chip multiplication arrays) use a signal amplification technique which takes place in an additional readout register known as a multiplication register, shown in figure 6.7. This multiplication of the collected signal takes place before the charge is converted into an electronic signal by the readout amplifier and so, if the multiplication is great enough, reduces the noise of the readout to negligible levels.

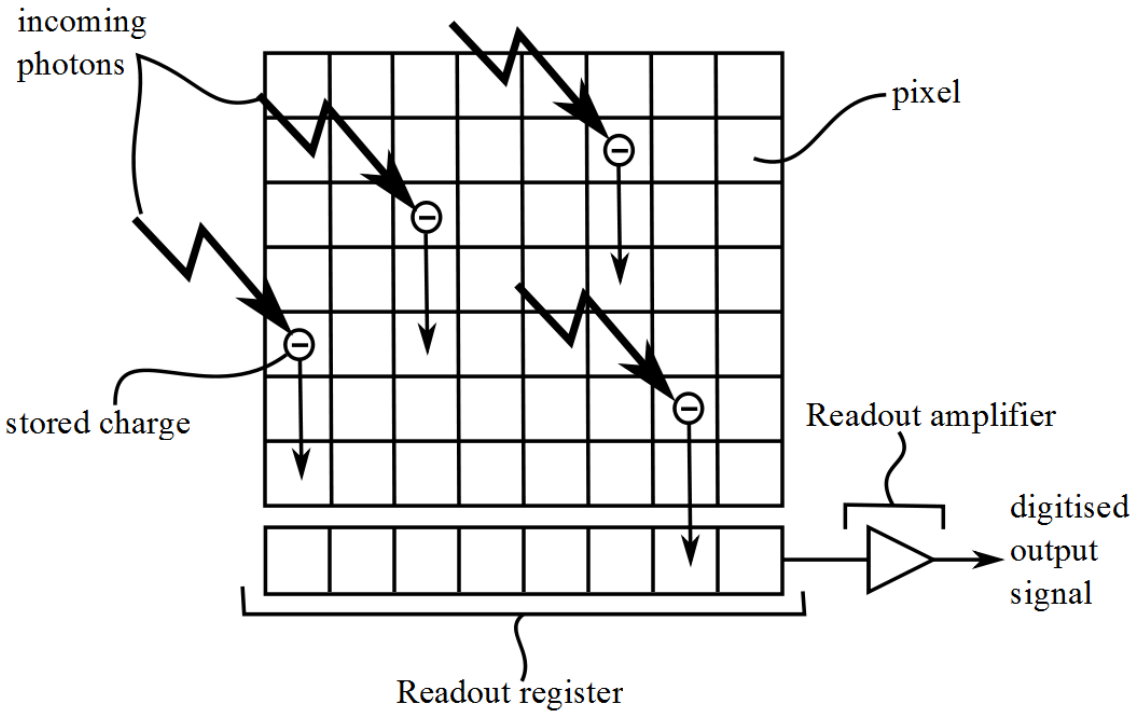

Figure 6.6: Diagram showing the general layout of a CCD array, including the readout register and the readout amplifier used to digitise the collected signal.

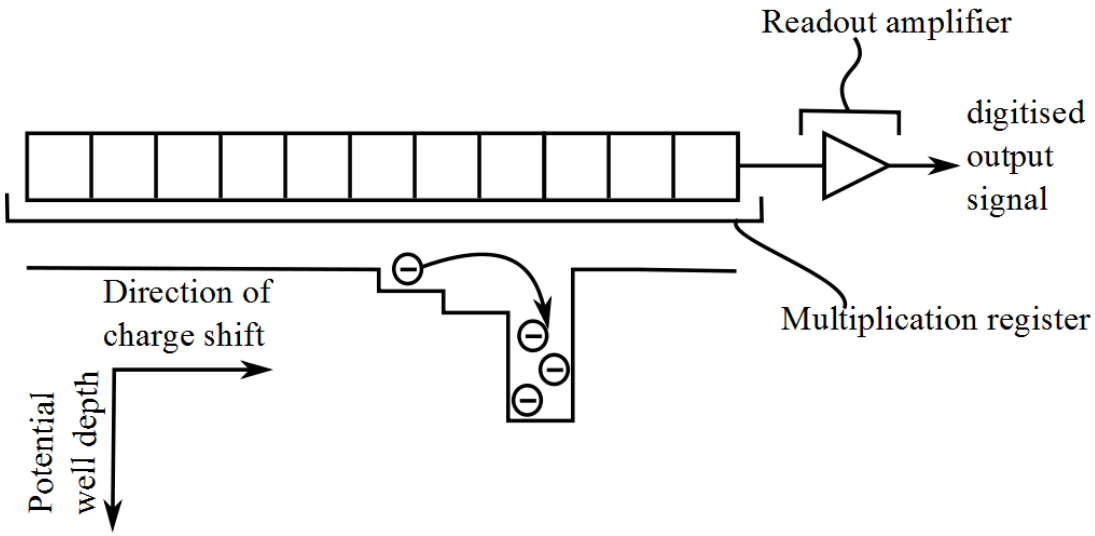

Figure 6.7: Diagram in which the multiplication register of an EMCCD array used to amplify the collected signal above the readout amplifier's noise floor is shown.

The process of amplification that takes place in the multiplication register is created by adjusting the size of the potential well in which each pixel stores its charge. These wells are created and controlled by electrodes in each pixel and so, by adjusting the voltage on the electrodes, the depth of the well can be changed. To create amplification, neighbouring wells are made deeper than previous wells and the charge is shifted into the adjacent deeper well. If the depth of the well is sufficient then there is a finite probability that additional charge will be liberated from the conduction band of the pixel. The amount of multiplication which occurs can be altered by varying the voltages (depth of the wells) in the pixels.

6.4.2 The ICCD

Intensified CCDs amplify the collected signal before it arrives at the CCD array. This is achieved with the use of an intensifier unit, shown in figure 6.8, which consists of a phosphor screen, a photocathode and a micro-channel plate encased inside an evacuated tube. The intensifier unit works by guiding incoming photons towards the photocathode where it liberates a photoelectron. Electric fields created by voltages applied to the photocathode and micro-channel plate result in the photoelectron being controllably guided into the micro-channel plate. This controllability is used to vary the gain applied to the photoelectron as it traverses the micro-channel plate which consists of a maze of $\approx$10 μm diameter glass channels covered in a resistive coating. When the photoelectron passes through these channels it can liberate extra electrons proportional to its initial energy when entering the channels. This results in the initial incident photon being amplified into a cloud of photoelectrons which are then guided onto the phosphor screen emitting a burst of photons related to the size of the photoelectron cloud. This photon burst is then collected by the CCD array and processed by the readout amplifier. If the amplification is sufficient the signal incident on the CCD can be large enough to consider the readout noise as negligible.

6.4.3 The PMT

Photomultiplier tubes (PMTs) utilise the photoelectric effect along with the ability of high velocity electrons to liberate additional electrons from a surface (known as secondary emission). A general layout of a PMT is shown in figure 6.9 depicting a linear arrangement of dynodes, however these can be arranged into any geometry. Incoming photons, incident on the PMT's photocathode, liberate photoelectrons which are accelerated by control

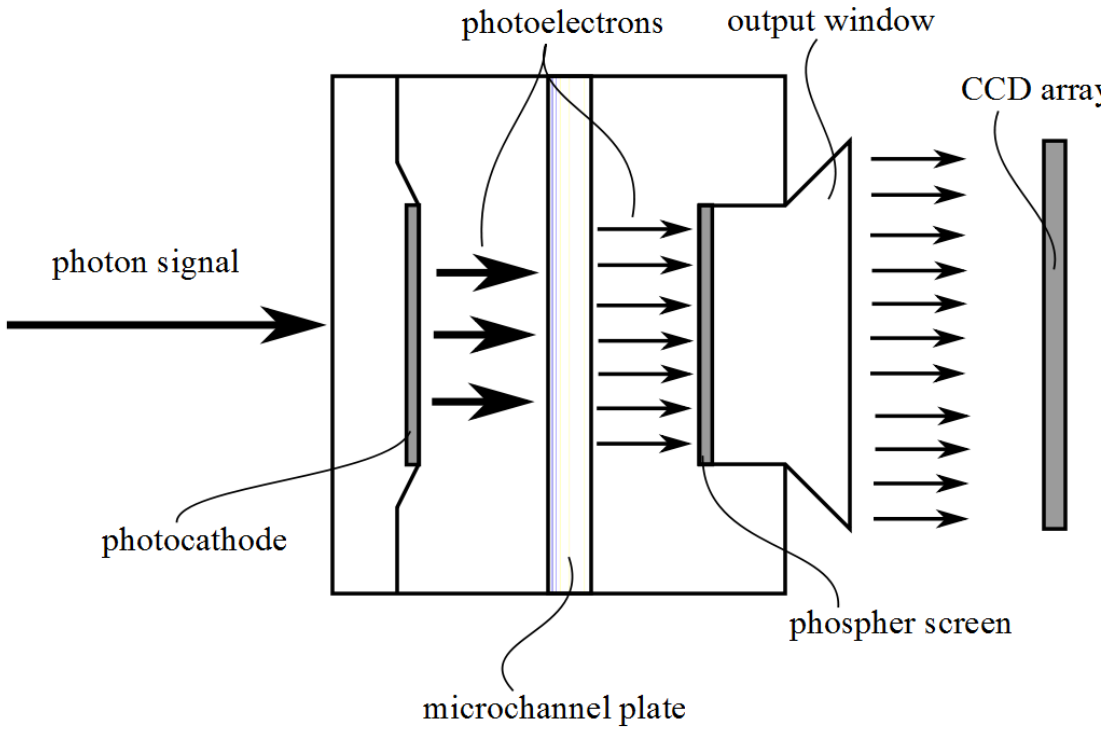

Figure 6.8: Diagram showing the layout of an ICCD's intensifier unit.

voltages towards a set of dynodes held at increasingly higher positive potentials. This allows secondary emission of electrons from the initial incident electrons. After passing through the series of dynodes the resulting cloud of electrons are collected at the anode from where an electrical current can be detected.

The photon counting PMT used in the imaging set up (Hamamatsu: H8259-01) is one which converts detected photons into TTL pulses which can then be counted by external electronics. This was preferred to a non-photon counting PMT as external electronics would have been required to convert the analogue signal created at the anode into pulses for the purpose of counting. In order for the PMT to produce pulses, which allow the number of photons detected to be counted, they must be spread out in time sufficiently. The PMT used in this work has a pulse-pair resolution of 35 ns, which means that photons arriving within 35 ns of each other will be counted as one photon. The width of the individual pulses is specified to 30 ns (with 5 ns between two consecutive pulses), and were measured to be 31±2 ns. The number of counts which the PMT detects is dependent on the count sensitivity of the device, C_s. This is a measurement of how many counts are detected per unit energy imparted onto the photocathode. By multiplying the count sensitivity by the energy of a single photon the more traditional quantum efficiency can

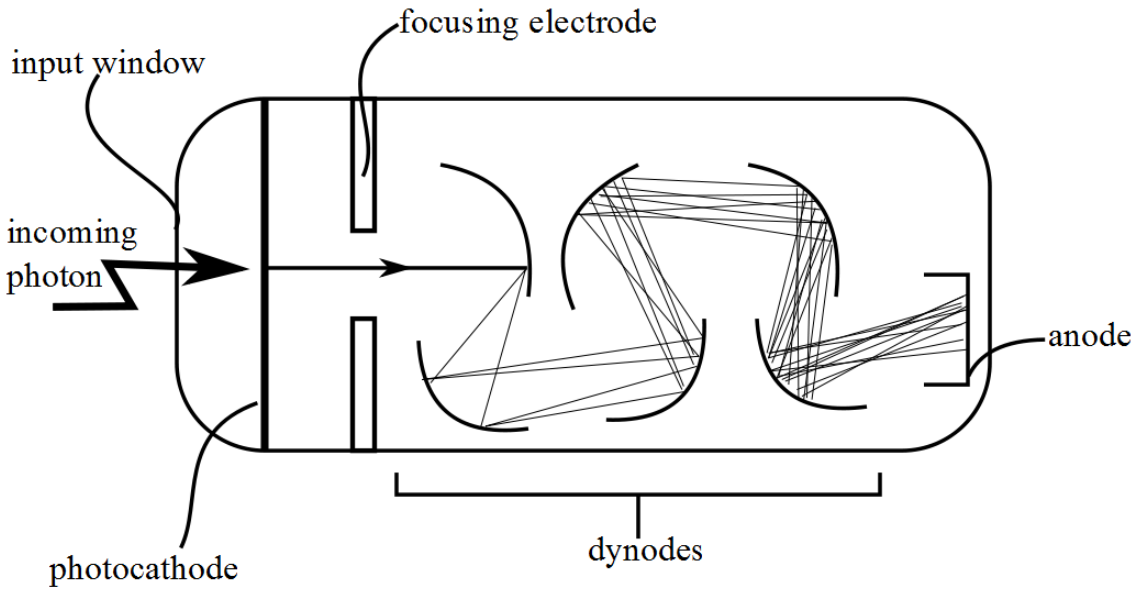

Figure 6.9: Diagram showing the general layout of a PMT. Shown is the photocathode used to convert the incoming photons into electrons, the electrodes used to focus the generated electrons onto the array of dynodes. The anode is also shown where the cloud of electrons created by the dynodes can be converted into an electronic signal.

be calculated. For example, the PMT used in this work has a count sensitivity of 3.3×10^5 s^{-1} pW^{-1} at a wavelength of 400 nm, which yields a quantum efficiency of $\approx 18\%$.

6.5 Comparison of photon detection devices

This section will describe the various noises which occur in the photon detection devices and then compare the signal to noise ratio of the various devices. This comparison will be carried out over a range of experimental parameters including photon flux incident on the detectors and then exposure time of the detectors to the incoming signal.

6.5.1 General noise

Shot Noise, N_{shot}

Shot noise is inherent in all devices which detect photon signals as it is a direct property of the emission from an ion, as it obeys Poissonian statistics. Emission of this type will have a noise associated with it given by $\sqrt{X}$ if the mean number of photons emitted is X. Because of this, the best a device can do in terms of noise is to approach this fundamental limit.

The shot noise, N_{shot}, of the signal detected by the photon detection devices is, therefore, given by

$$N_{shot} = FQ\sqrt{\phi_i \tau} \tag{6.14}$$

where Q is the quantum efficiency of the device, ϕ_i is the rate of incident photons arriving at the detector (given by equation 6.4) and τ is the time over which the signal is integrated (for a camera this would be the exposure time of one frame). F is a noise factor of the gain process and will vary slightly for each type of device but is generally in the range of 1.3 to 2 [72].

6.5.2 CCD noise

Dark noise, N_{dark}

Dark noise is associated with CCD arrays and is generated by thermally liberated electrons in the pixel's silicon structure. Camera specifications quote a dark current, I_{dark}, measured in photons per pixel per second and occurs regardless of any incoming signal. For this reason, single photon sensitive devices are cooled in order to reduce this level of noise to an acceptable level. Several techniques exist to cool CCD chips including water cooling and liquid nitrogen cooling, which require bulky external equipment to carry out. However, a simple solution is the use of a device similar to that of a Peltier cooler which can reduce the operating temperature of the CCD array to -100 °C without the need for bulky external equipment. The dark noise of a CCD camera can be obtained by multiplying the dark current, I_{dark}, by the number of pixels to be read out, P, and the time, τ, over which the signal is integrated.

$$N_{dark} = I_{dark} \tau P \tag{6.15}$$

However, it is important to note that, as the dark noise occurs on the pixel array, an EMCCD is subject to the gain of the device as the dark noise occurs before the signal is amplified. This is not the case in an ICCD, where the signal is amplified before the dark noise occurs.

The dark noise of a PMT is simply given as the number of spurious events counted by the device per second, C_{dark}. The dark noise of a PMT is, therefore, given by

$$N_{Pdark} = C_{dark} \tau \tag{6.16}$$

Readout noise, N_{read}

The collected signal must be amplified above this noise in order to be detectable. A device can detect a single photon if the signal produced by one photon can be amplified above this noise. The noise itself is generated by the electronic circuitry used to digitise the signal and is strongly dependant on the speed at which this is performed and so a greater signal to noise ratio can be achieved by reading out the signal slowly. However, many applications require a fast readout and so the various gain mechanisms must be used to increase the signal above this noise level to achieve single photon detection at high readout rates. The readout noise is generally quoted per pixel and so the total readout noise for a frame will be the number of pixels multiplied by the readout noise. This type of noise has no relationship with the time over which the signal is integrated.

Clock induced charge, N_{clock}

Clock induced charge noise arises from the same process that creates the signal multiplication in an EMCCD when charge stored in one pixel is shifted to an adjacent pixel and liberates electrons from the silicon structure. Because this noise occurs during the charge transfer it is important to use the slowest charge transfer rate (the pixel shift rate) possible for the detection in order to reduce this noise. Clock induced charge currents, I_{clock}, for cameras are quoted per pixel resulting in a dependence on the number of pixels used in the CCD, P.

$$N_{clock} = I_{clock} P \tag{6.17}$$

Again this noise is subject to gain in an EMCCD and not in an ICCD as the noise is created in the pixel array.

Equivalent background illuminance, N_{EBI}

The noise created by equivalent background illuminance is only applicable to the ICCD and is caused by spurious noise events in the microchannel plate. These spurious events are then collected by the CCD array and the equivalent background illuminance current, I_{EBI}, is quoted per pixel per second and, therefore, the noise created by this is given by

$$N_{EBI} = I_{EBI} P \tau \tag{6.18}$$

6.5.3 Signal to noise comparison

From the discussion on what types of noise are present in the three devices (EMCCD, ICCD and PMT) it is now possible to arrive at equations expressing the signal to noise ratio of each device. From these equations the signal to noise ratio of the devices can be compared under different experimental conditions in order to determine which device is best suited for different applications. As the noises of the devices add in quadrature the total noise for an exposure on the devices can be given as

$$N_{ICCD} = \sqrt{(GN_{shot})^2 + (N_{dark})^2 + (N_{clock})^2 + (GN_{EBI})^2 + N_{read}^2} \tag{6.19}$$

for the ICCD,

$$N_{EMCCD} = \sqrt{(GN_{shot})^2 + (GN_{dark})^2 + (GN_{clock})^2 + N_{read}^2} \tag{6.20}$$

for the EMCCD and,

$$N_{PMT} = \sqrt{N_{shot}^2 + N_{Pdark}^2} \tag{6.21}$$

for the PMT.

The signal, S_{CCD}, for the two types of CCD which is collected by the devices during each exposure time, τ, is given by

$$S_{CCD} = QG\phi\tau \tag{6.22}$$

where ϕ is the number of photons incident on the device every second, Q is the quantum efficiency of the device and G is the gain of the device. The signal, S_{PMT}, for the PMT is calculated via the device's count sensitivity, C_s. This is a measurement of how many counts the PMT produces for a given input of photon energy. By calculating the energy of a single photon, E, the number of output counts can be calculated by multiplication with the count sensitivity, C_s, and so the total signal detected by the PMT can be expressed as

$$S_{PMT} = EC_s\phi\tau \tag{6.23}$$

The signal to noise ratio of the three devices can then be expressed as

$$s/n_{ICCD} = \frac{S_{CCD}}{N_{ICCD}} = \frac{QG\phi\tau}{\sqrt{(GN_{shot})^2 + (N_{dark})^2 + (N_{clock})^2 + (GN_{EBI})^2 + N_{read}^2}} \tag{6.24}$$

for the ICCD,

$$s/n_{EMCCD} = \frac{S_{CCD}}{N_{EMCCD}} = \frac{QG\phi\tau}{\sqrt{(GN_{shot})^2 + (GN_{dark})^2 + (GN_{clock})^2 + N_{read}^2}} \tag{6.25}$$

for the EMCCD, and

$$s/n_{PMT} = \frac{S_{PMT}}{N_{PMT}} = \frac{EC_s\phi\tau}{\sqrt{N_{shot}^2 + N_{Pdark}^2}} \tag{6.26}$$

for the PMT.

It is important to note here that as the gain is increased in the EMCCD and ICCD the read-out noise becomes less important to the overall signal to noise ratio of the devices as the noises with a dependence on the gain, G, dominate the overall noise. It can be seen that when the gain is increased an ICCD will have a better signal to noise ratio compared to that of an EMCCD as the shot noise and EBI dominates, whereas in the EMCCD the combination of the shot, dark and clock noise is dominant. However, this is only the case if the incident photon signal, ϕ, is small (of a value that results in the shot noise being less than or equal to the dark and clock noise). If the incoming photon signal becomes large enough (of a value that results in the shot noise being much greater the dark and clock noise) then the shot noise will dominate over all the other noise terms and results in an EMCCD having a higher signal to noise ratio compared to that of an ICCD:

$$s/n_{ICCD} \approx \frac{QG\phi\tau}{\sqrt{(GN_{shot})^2 + (GN_{EBI})^2}} \tag{6.27}$$

$$s/n_{EMCCD} \approx \frac{QG\phi\tau}{\sqrt{(GN_{shot})^2}} \tag{6.28}$$

The reason for this is that the dominant noise in the EMCCD will be the shot noise whereas in the ICCD it will be the sum of the shot and EBI noises. This is illustrated in figure 6.10 as below about 100 photons per second incident on the detectors the ICCD has a superior signal to noise ratio compared to that of the EMCCD and after around 100 photons per second incident on the detectors the EMCCD has the superior signal to noise ratio. The estimated photon flux from a single ion is indicated by the vertical dashed in figure 6.10. Here it can be seen that the EMCCD has a slightly higher signal to noise ratio (≈ 40) compared to that of the PMT and IMCCD (≈ 30). For this case, although the EMCCD has the superior signal to noise ratio, all three types of detectors would be capable of detecting the florescence of a single ion.

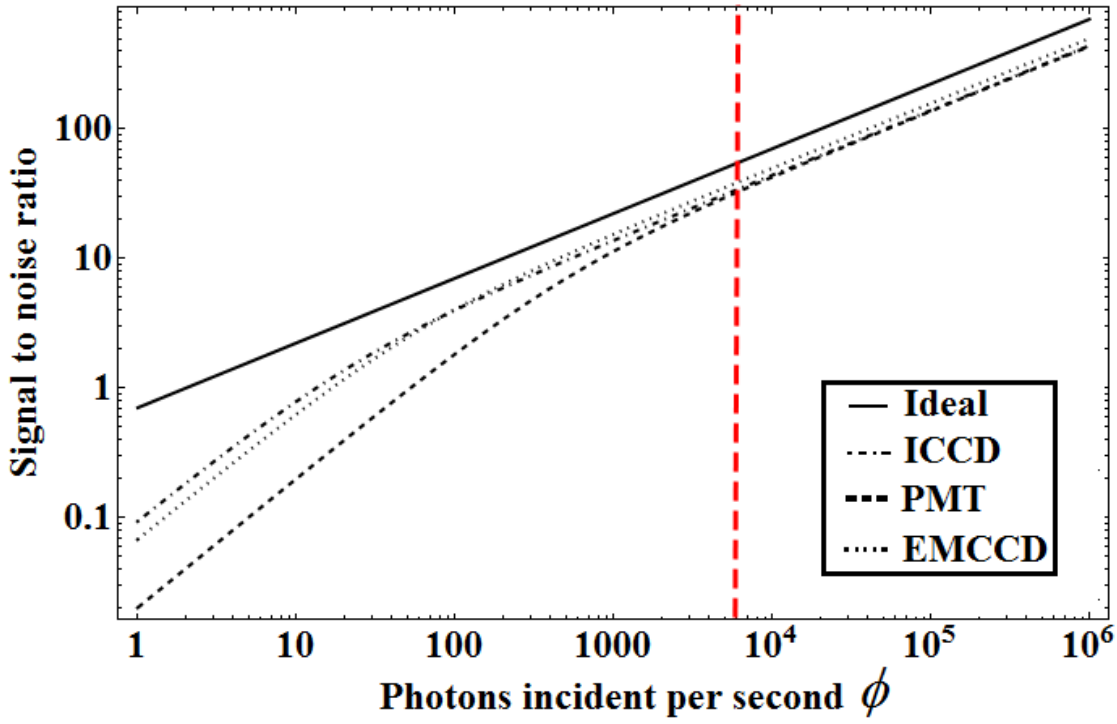

Figure 6.10: Graph showing the signal to noise ratio for a 10 by 10 pixel ROI of a typical EMCCD, PMT and ICCD as a function of the photons incident on the devices per second, ϕ. Also shown is the ideal signal to noise ratio given simply by the limit obtained from shot noise only. The vertical dashed line indicates the estimated approximate photon flux from a single ion.

6.5.4 Frame rate comparison

When carrying out an experiment with trapped ions it is important to choose the correct detection device. If spatial resolution of the ions is required the CCD must be used as the PMT does not offer this, but if spatial resolution is not an issue the device with the highest signal to noise ratio should be chosen. The noise of the CCD is dependent on the time over which the incident signal is integrated (the frame time), τ, and the number of pixels, P, over which the signal is spread (the ROI) and so it follows that the device with the highest signal to noise ratio will be dependent on these values. Figure 6.11 shows the area (shaded) in which an EMCCD (Andor: iXon^{EM}+ 885) has a higher signal to noise ratio compared to that of a PMT as a function of the number of pixels in the CCDs ROI and the number of photons incident on the detector per second. The graph shows that, generally, as the number of incident photons per second is reduced the size of the EMCCD ROI needed to provide a larger signal to noise ratio compared to that of the PMT is reduced. The reason for this is that as the incident photon rate reduces so does the shot noise error associated with the signal, becoming closer in value to the dark noise and clock induced charge. The approximated signal to noise expression in equation 6.28 becomes less valid at low incident photon levels. This means that the noise of the CCD is effected more by the devices dark noise, clock induced charge and readout noise, whereas, the PMT is only ever effected by the shot noise and its dark noise. For a low photon flux the expression for signal to noise given by equation 6.25 should be used. For the case of detecting a single trapped ion, the number of photons emitted from an ion per second is given by [50]

$$\gamma = \frac{s\frac{\Gamma}{2}}{1 + s + (\frac{2\Delta}{\Gamma})^2}$$

where Γ is the linewidth of the transition, s is the saturation parameter and Δ is the detuning of the laser from the transition frequency. For typical detection experiments s is around one and the detuning is around 10 MHz, providing the number of photons emitted from an ion per second as $\approx 330,000$. As the Special Optics triplet lens used collects 2.2% of the emitted photons (equation 6.8) and the transmission coefficient through the imaging optics, T, is estimated at being ≈ 0.9 the total number of photons incident on the detectors will be ≈ 6000 per second. Using this photon flux along with equations 6.25 and 6.26 the signal to noise ratio of the two devices can be calculated for different exposure times. For the exposure times used in figure 6.11 the EMCCD can be seen to have a superior signal to noise ratio when the image is spread over a pixel number shown

in the figure by the shaded region. Under conditions when the signal to noise ratio of the EMCCD is less than PMT but they both have a signal to noise ratio much larger than one (meaning that an ion is easily noticeable above the noise in both detectors) the EMCCD offers the advantage of spatial resolution whereas the PMT does not. This extra information provides vital information when aligning the laser beams into the centre of the trap and also of the position of the area being imaged in reference to the trap electrodes which is not as easy to achieve with a PMT. For these reasons it is advisable to use an EMCCD over a PMT to initially trap an ion. Additionally, the spatial resolution of the EMCCD provides a tool with which measurements of fluorescence of multiple ions can be made simultaneously, whereas the PMT would either not allow multiple ion measurement or the measurement would have to be undertaken on each individual ion separately.

Binning is a process whereby several pixels are used together as one larger pixel. The advantage of this is that fewer pixels need to be read out resulting in less readout noise being added to the signal. The other noise sources remain at the same level as the same total number of pixels is still in use. The disadvantage of binning, however, is the degradation in spatial resolution and so this process is only an option in experiments which require little spatial resolution (or can cope with a reduced resolution).

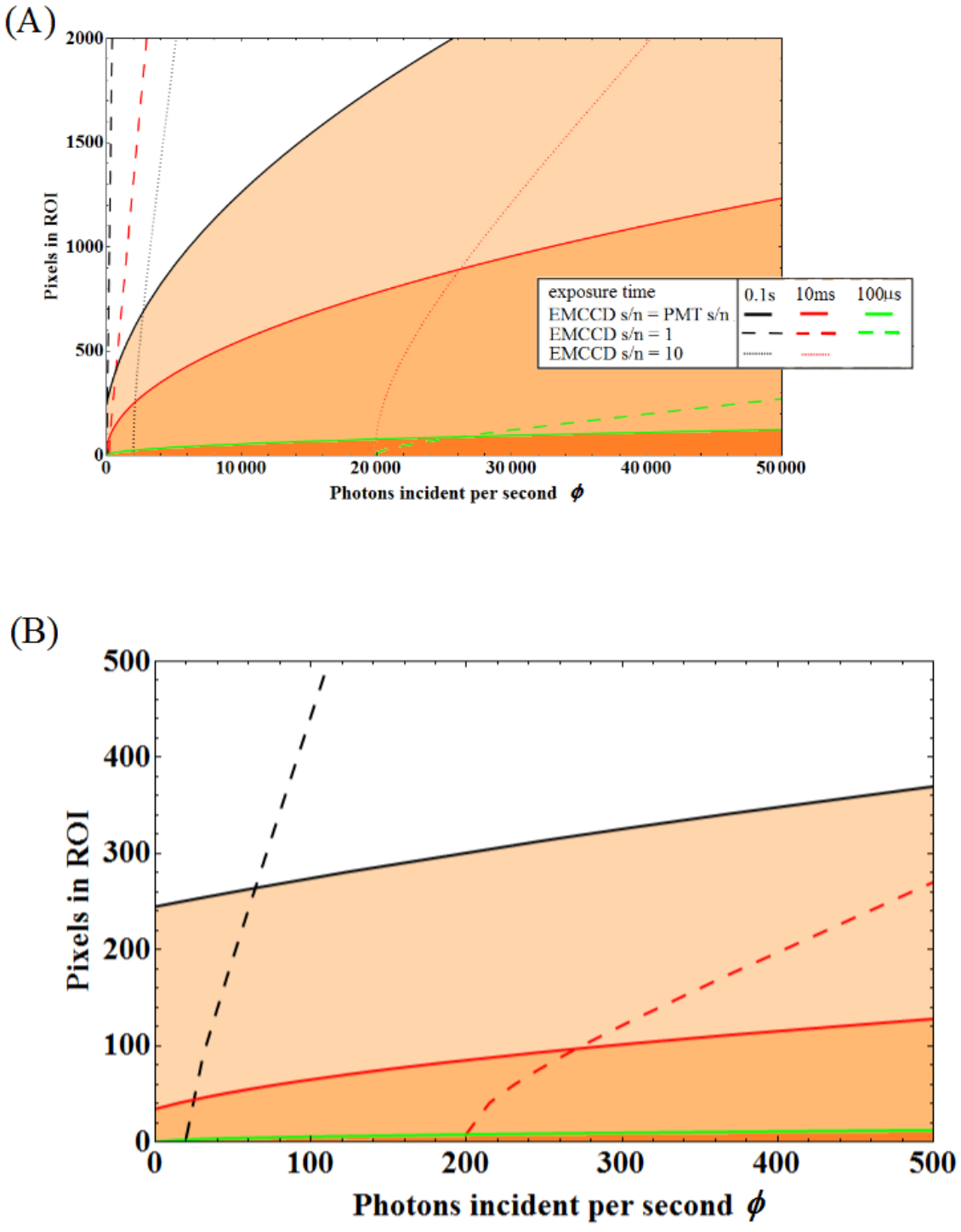

Figure 6.11: (A): Graph showing the area (shaded) where an EMCCD has a superior signal to noise ratio to a PMT. The signal to noise ratio for the EMCCD equalling 1 (dashed), 10 (dotted) are also shown. (B) Graph showing an inset of the graph in (A).

Chapter 7

Experiments with trapped ions

7.1 Introduction

This section describes several experiments which have been performed using the experimental apparatus introduced in this work. Initially the $^{174}Yb^{+}$ isotope is ionised, trapped and the secular frequencies of the ion experimentally determined. From this, the trap depth can be deduced by using a BEM (boundary element method) simulation along with the experimentally obtained frequencies. It was noted during this initial trapping procedure that Yb^{+} ion transition frequencies were not available to the required accuracy for successful trapping. For this reason the ^{170}Yb, ^{171}Yb, ^{172}Yb, ^{174}Yb and ^{176}Yb isotopes were ionised and trapped. Their transition frequencies were then found to an accuracy of 120 MHz. Heating rate measurements of Yb^{+} ions in a Paul trap were undertaken and shown to not be any higher than other elements used for ion trapping.

7.2 Initial trapping, secular frequency and trap depth determination

Using the experimental apparatus described in this thesis both single Yb^{+} ions and Yb^{+} ion crystals can be trapped, as shown in figures 7.1 and 7.2. The initial trapping of Yb^{+} ions was carried out using the blade trap described in section 3.3 and figure 3.6 with static voltages and an rf voltage and frequency shown in table 7.1.

Once a single ion of Yb^{+} was trapped, its secular frequencies were measured by applying a small amplitude (between 1 to 10 volts) ac voltage to one of the end cap electrodes. The frequency of this voltage was then scanned and, when equal to a secular frequency, causes the ion to be driven in that particular axis of motion. This excitation can be de-

Table 7.1: Experimentally measured trapping voltages for the macroscopic trap shown in figure 3.7

rf voltage	680 ± 10 V
rf frequency	21.48 ± 0.05 MHz
Static voltage 1	0 ± 0.01 V
Static voltage 2	7.36 ± 0.01 V
End 1	148.88 ± 0.01 V
End 2	25.03 ± 0.01 V
End 3	167.76 ± 0.01 V
End 4	0 ± 0.01 V
Comp 1	169.22 ± 0.01 V
Comp 2	-2.70 ± 0.01 V

.

tected as a visible distortion to the image of the ion on the EMCCD picture. The error on the secular frequency using this method corresponds to the frequency range over which the trapped ion's image is observed to distort. Using this method of detection the secular frequencies, $(\omega_x, \omega_y, \omega_z)/2\pi$, of a single trapped $^{174}Yb^+$ ion were measured as (2.069, 2.110, 1.030) $\pm$0.001 MHz respectively.

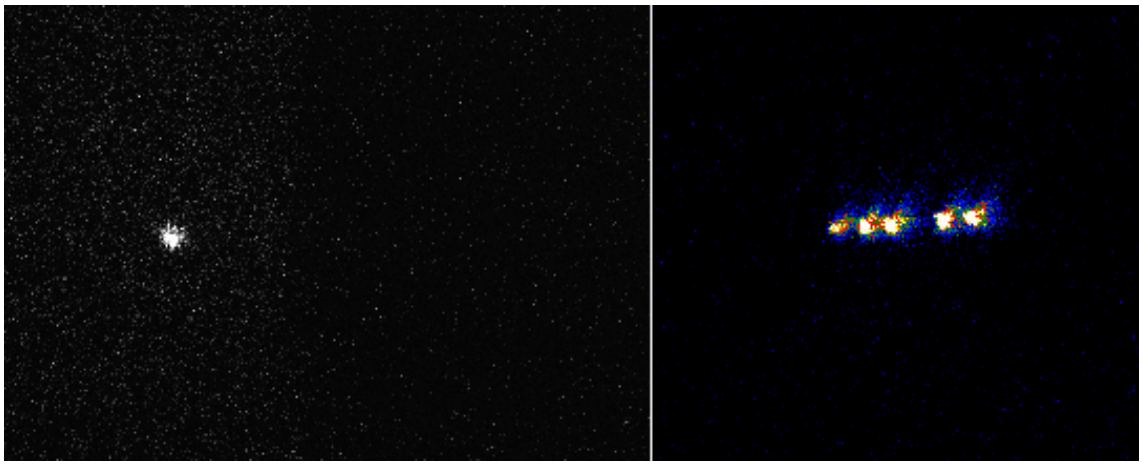

Figure 7.1: **Left:** A single Yb^+ ion is shown using an EMCCD. The slightly less noisy background on the right hand side indicates the position of an electrode. **Right:** A six ion multi isotope Yb^+ chain is shown. The gap in the chain indicates the presence of an isotope of Yb which is not resonant with the cooling laser. This demonstrates the set-up's ability to trap different isotopes towards performing sympathetic cooling.

Measuring the positions of the trap electrodes using the imaging system enables a

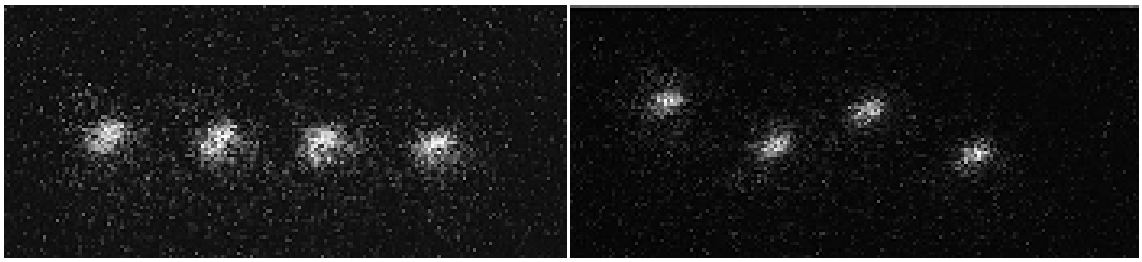

Figure 7.2: **Left:** An EMCCD image of a chain of four Yb^+ ions. **Right:** The same chain of four ions are shown in a zig-zag configuration. This is achieved by increasing the axial secular frequency with respect to the radial secular frequencies.

boundary element method (BEM) simulation of the electric field created by the actual trap constructed (as opposed to a simulation using the designed perfect electrode positions). By doing this a more accurate rf null position can be obtained aiding initial trapping. The rf voltage cannot be directly measured, however, it can be inferred from the BEM simulation of the trapping field by finding the rf voltage required to create the measured secular frequencies. Using this inferred rf voltage the trap depth can also be inferred from the field simulation. For the voltages shown in table 7.1, the trap depth was calculated to be 4.9 ± 0.2 eV. With these trapping conditions ion lifetimes of hours are observed, even without the presence of optical cooling.

7.3 Yb^+ transition frequency measurements

Previous works [33] have used hollow cathode lamps to measure the Yb^+ Doppler broadened absorption line at 369.525 nm with a width and accuracy around 3 GHz in order to frequency stabilise lasers. This accuracy, however, is not sufficient to determine the wavelengths required to cool the various Yb^+ isotopes as they are required to be known to within a few tens of MHz. For this reason it was the aim of this work to measure the absorption lines of the individual isotopes to a precision which allows this. To initially trap ions, the wavelengths of the lasers were systematically varied within the previous work's Doppler broadened measurement until an ion of the desired species was trapped and cooled. The 398.9 nm ionisation laser was set to the specific ion's transition frequency for an angle of 63° to the atomic oven flux [36]. Once an ion was visible the 369.5 nm cooling laser's frequency was increased until the detected florescence of the ion dropped suddenly back to that of the background noise level. This indicates that the frequency was now blue detuned from resonance and the ion was being heated by the laser. It can be assumed that resonant frequency of the transition is the one which corresponds to the

peak ion florescence. This process was carried out for the 170, 171, 172, 174 and 176 Yb isotopes and the wavelengths for each are shown in table 7.2. The wavelengths were measured using a wavemeter (High Finesse: WS7). For the even isotopes no external magnetic field was applied but for $^{171}Yb^{+}$ ions an external 0.5 mT magnetic field was applied in order to remove the degeneracy within this isotope's Zeeman levels.

Table 7.2: Table showing the transition wavelengths of neutral Yb ($^1S_0 \leftrightarrow {}^1P_1$) for the purpose of ionisation. Also show are the Yb^{+} ion wavelengths needed for cooling ($^2S_{1/2} \leftrightarrow {}^2P_{1/2}$) and re-pumping ($^2D_{3/2} \leftrightarrow {}^3D[3/2]_{1/2}$).

Yb isotope	$^1S_0 \leftrightarrow {}^1P_1$ wavelength [nm]	$^2S_{1/2} \leftrightarrow {}^2P_{1/2}$ wavelength [nm]	$^2D_{3/2} \leftrightarrow {}^3D[3/2]_{1/2}$ wavelength [nm]
170	398.91051(6)	369.52364(6)	935.19751(20)
171	398.91070(6)	369.52604(6)	935.18768(20)
172	398.91083(6)	369.52435(6)	935.18736(20)
174	398.91114(6)	369.52494(6)	935.17976(20)
176	398.91144(6)	369.52550(6)	935.17252(20)

During the measurements of the ion transition wavelengths, the intensities of the 369 nm and 935 nm lasers were set at 0.4 Wcm^{-2} and 0.02 Wcm^{-2} respectively. By setting the beam intensities to these values, any effects on the transition frequency due to power broadening and the ac Stark shift can be ignored. Once the 369 nm transition has been determined by observing the point at which the ion fluorescence drops back to background noise levels the wavelength of the 935 nm laser can be optimised. This is done by varying the 935 nm laser and observing the wavelength when the fluorescence from the ion peaks to a maximum. Precise measurements of the 638 nm ($^2F_{7/2} \leftrightarrow {}^1D[5/2]_{5/2}$) transition are difficult to obtain due to the infrequent population of the F state. For this reason the transition was power broadened by applying an intensity of 120W cm^{-2} using 638.618 nm for the even isotopes and scanning between 638.610 nm and 638.616 nm for the 171 isotope in order to account for the hyperfine states [44]. These values were found to produce no obvious interruptions in the ion fluorescence indicating that the wavelengths used are close enough to immediately remove the ion from the F state.

The errors associated with the 369 nm and 935 nm laser wavelengths quoted in table 7.2 are due to the accuracy of the wavemeter, which is specified to be 200 MHz below 370 nm and 60 MHz between 370 nm and 1100 nm. To reduce the 200 MHz error on the 369 nm wavelength, the wavelength of the 739 nm (with an error of 60 MHz) laser can be

measured resulting in a 369 nm error of 120 MHz. To eliminate any systematic offsets of the wavemeter and to reduce any drift in the wavemeter over the course of the wavelength data collection the wavemeter was calibrated using a 780 nm laser locked to a ^{87}Rb D^2 line and confirmed with a He-Ne laser (both with a frequency accurate to below 1 MHz) before each measurement. The errors associated with the 399 nm laser wavelengths are due to the error associated with aligning florescence spots from counter propagating beams in a bell jar with neutral atomic flux present as described in [36].

7.4 Heating rate measurement

Quantum computation and simulation rely on interactions between ions and lasers to prepare, entangle, manipulate and read-out atomic states which are dependent on the motional state of the ions. Because of this it is important to know how much uncontrolled heating occurs in a particular trap structure. In the procedures required for quantum computation, any uncontrolled heating of the ion motion provides a limiting factor on the fidelity of the procedures and, therefore, the overall fidelity of the computation. This section will describe the basic theory and method used to measure the heating rate of a single Yb^+ ion in the blade trap described in this thesis in chapter 3 and based on that proposed by J. H. Wesenberg et al [34].

A single trapped Yb^+ ion is not cooled by removing the 369 nm Doppler cooling laser using an acousto-optic modulator (AOM (Isomet: 1212-2-949)) for periods of 1, 3, 5 and 7 seconds. The response time of the AOM was specified to be on the order of $\approx$ 100 ns which means that it can be ignored when considering the amount of time the cooling light is removed for. Once the 369 nm laser is switched back on, the fluorescence of the ion is measured for 4 ms, split into 50 μs bins. For the method described in [34] the ion's energy change is required to be dominated by heating along one axis of motion only. As it is known that the heating rate of an ion obeys a $1/\omega^2$ law [66, 73] (where ω is the angular secular frequency), the secular frequencies $(\omega_x, \omega_y, \omega_z)/2\pi$ were set to (2.069, 2.110, 0.178)$\pm$0.001 MHz respectively. The timing of the experiment, shown in figure 7.3, was controlled using a LabVIEW FPGA module implemented on an NI-Compact RIO (National Instruments: PXI-1033) and an NI-PXI-7842R card. The reason for the overlap between the cooling laser switch off phase and the photon detection on phase was to ensure that all the ion florescence was collected correctly in the event of delayed detection.

When the ion is subject to heating, its velocity, v, increases as well as its instantaneous Doppler shift, $\Delta_D = -kv$, where k is the wave vector of the cooling laser. The maximum

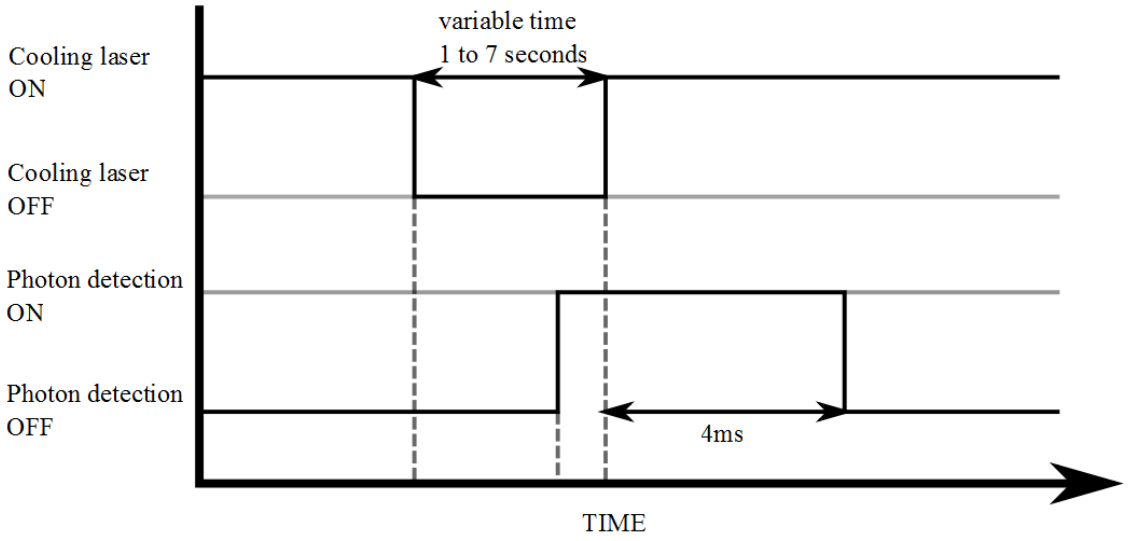

Figure 7.3: Diagram showing the timing of the heating experiment.

instantaneous Doppler shift is denoted as Δ_{max}. The probability of the ion experiencing a particular Δ_D can be described by the probability density $P_D(\Delta_D)$ [34] and so the scattering rate of the ion is affected by the overlap of $P_D(\Delta_D)$ with the Lorentzian line profile, $L(\Delta)$. When in a situation where the ion is hot (where $\Delta_{max} \gg |\Gamma| + |\Delta|$ with Δ being the detuning of the cooling laser from resonance) the Doppler shift probability and the Lorentzian line profile overlap poorly, as seen in figure 7.4(a), resulting in low scattering rates. When in the situation where the ion is cold, as shown in figure 7.4(b), the probability density overlaps well with the Lorentzian line profile resulting in an increased scatter rate.

The energy change of an ion during one period of oscillation in the trapping potential is much less than the total energy change during the whole of the re-cooling experiment. This allows the energy over an oscillation (and hence the scatter rate) to be averaged and given by [34]

$$\left\langle \frac{dN}{dt} \right\rangle = \int \frac{dN}{dt} P_D(\Delta_D) d\Delta_D \tag{7.1}$$

where dN/dt is the instantaneous scatter rate of the ion. In the case of a hot ion, figure 7.4 (a), the probability density, $P_D(\Delta_D)$, can be approximated as being uniform over the

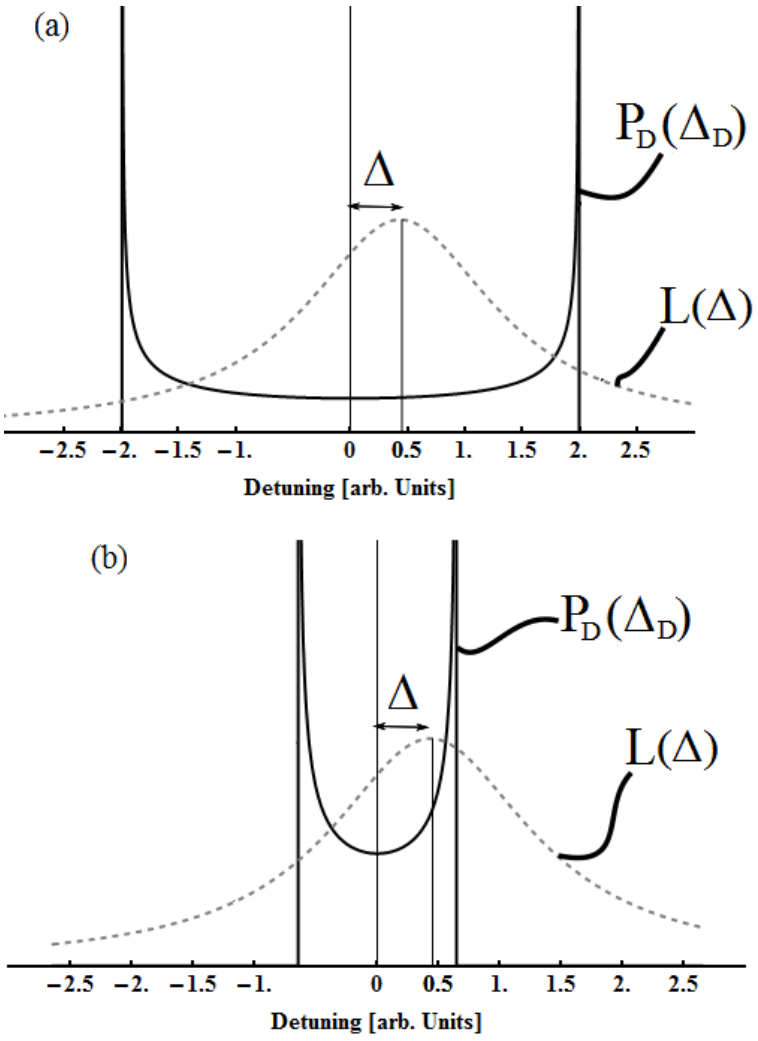

Figure 7.4: Diagram of Doppler overlap with the Lorentzian line profile. (a) Shows the case of a hot ion where there is a poor overlap between the Doppler shift probability and the Lorentzian line profile, $L(\Delta)$. (b) Shows the case for a cold ion, where the Doppler shift probability overlaps well with the Lorentzian line profile, $L(\Delta)$.

Lorentzian line profile. The probability density can then be factored out and the scatter rate of the ion can be expressed in terms of the ion's energy at time t, $E(E_0, t)$, and energy before cooling, E_0, [34]

$$\left\langle \frac{dN}{dt} \right\rangle (E(E_0, t)) = \frac{1}{\sqrt{E(E_0, t)}} \frac{s\Gamma^2}{2\sqrt{\frac{2}{m} k_z (1+s)^{\frac{3}{2}}}} \tag{7.2}$$

where m is the ion mass, k_z is the Z component of the laser beam vector, Γ is the observed transition linewidth and s is the saturation parameter. Using a one-dimensional Maxwell-Boltzmann distribution [34] to describe the thermal distribution of the ion before re-cooling, E_0, the average scattering rate for the ion is then [34]

$$\left\langle \frac{dN}{dt} \right\rangle_{E_0} = \int_0^\infty P_B(E_0) \left\langle \frac{dN}{dt} \right\rangle (E(E_0, t)) dE_0 \tag{7.3}$$

where $P_B(E_0)$ is the 1D Maxwell-Boltzmann distribution [34].

For the heating measurements carried out a detuning of $\Delta = 6 \pm 2$ MHz, a saturation parameter of $s = 1.0 \pm 0.2$ and the Z-component of the laser beam vector of $k_z = 0.45k$ were used. With these parameters the linewidth, Γ, of a trapped $^{174}Yb^+$ was measured as 40 ± 5 MHz and is assumed to be broadened due to the effects of power broadening and any uncompensated micromotion. Each heating measurement, described by figure 7.3, was repeated 500 times and averaged for each delay time due to the thermal distribution of the ions initial energy, E_0. Equation 7.3 can then be fitted to the average ion fluorescence by using E_0 as a free fitting parameter, as shown in figure 7.5.

The ion energy can be converted into motional quanta via $\langle n \rangle = E/\hbar\omega$ and so the change in motional quanta after the different delay periods can be calculated, and are shown in figure 7.6. This process was then repeated at different secular frequencies, (178, 287, 355)$\pm$1 KHz and the heating rate as a function of this secular frequency was shown to obey the predicted $1/\omega^2$ relationship [66, 73]

$$\langle \dot{n} \rangle = \frac{q^2}{4m\hbar\omega_z} S_E(\omega_z) \tag{7.4}$$

where q is the charge of an ion, m the mass of an ion and $S_E(\omega_z)$ is the electric field noise density and is proportional to ω^{-1} [66]. The results for the heating rate as a function of secular frequency are shown in figure 7.7.

Figure 7.6 shows an offset of Δn. This offset is thought to be caused, primarily, by two processes. Firstly, any micromotion present will act to heat the ion and raise the initial n. As micromotion was only very crudely compensated for in this experiment it is likely that

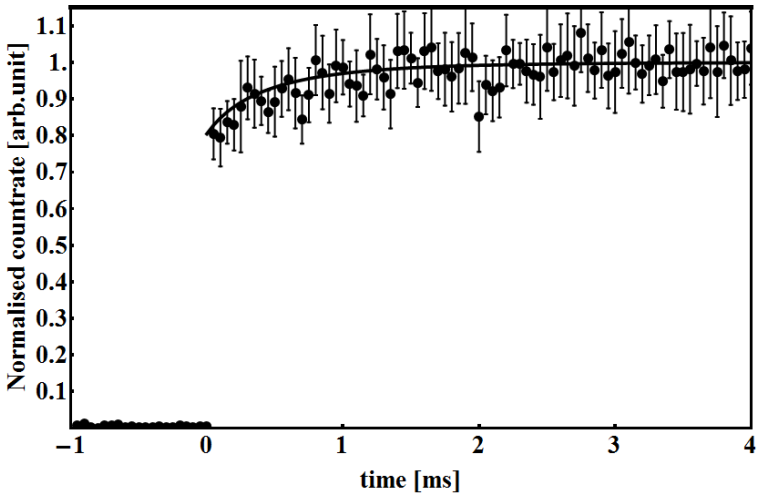

Figure 7.5: Graph showing a result for the ion fluorescence during the photon detection phase described in figure 7.3 after being subjected to heating as a result of the cooling laser being switched off for five seconds. Time zero corresponds to when the cooling laser was turned on again after heating. This result was achieved with a secular frequency of $\omega_z = 180$ kHz.

this process has a significant effect on the offset in figure 7.6. Secondly, it is possible that the ion is displaced from the exact trapping centre by radiation pressure from the cooling laser. When this laser is turned off, to allow heating to occur, the ion will move back to the centre of the trap, effectively heating the ion and causing an offset in figure 7.6.

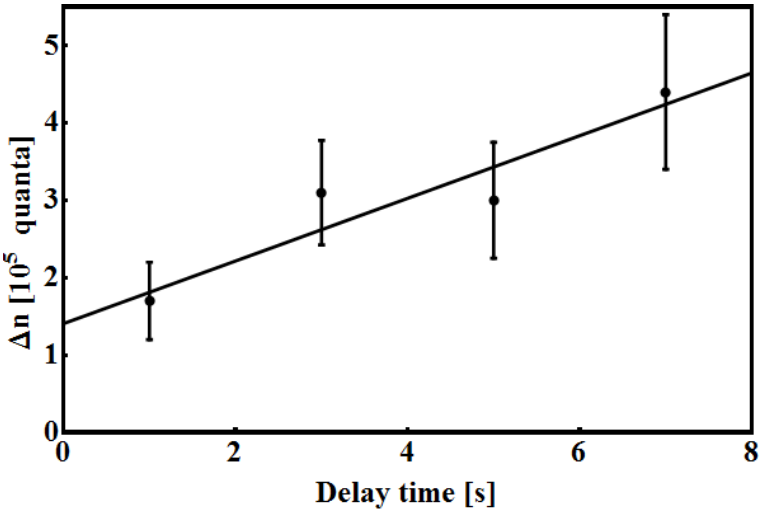

Figure 7.6: Graph showing the change in motional quanta after heating periods of 1,3,5 and 7 seconds. Each result is an average of 500 measurements.

Figure 7.8, taken from [3], shows current published experimental results of the product of electric field noise spectral density $S_E(\omega)$ and the secular frequency, ω, versus ion-

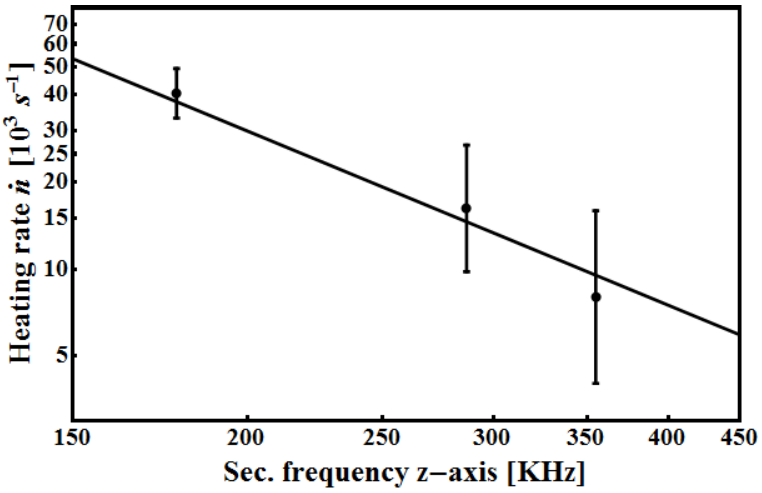

Figure 7.7: Graph showing the heating rate of a $^{174}Yb^{+}$ as a function of secular frequency.

electrode distance, r, taken at both room and cryogenic temperatures obtained in other ion-trapping experiments. The result obtained in this work is indicated by the dashed box. The dashed line shows a $1/r^4$ trend though the data taken at room temperature. The product of electric field noise spectral density and the secular frequency found in this work is shown to be consistent with existing experimental results at room temperature.

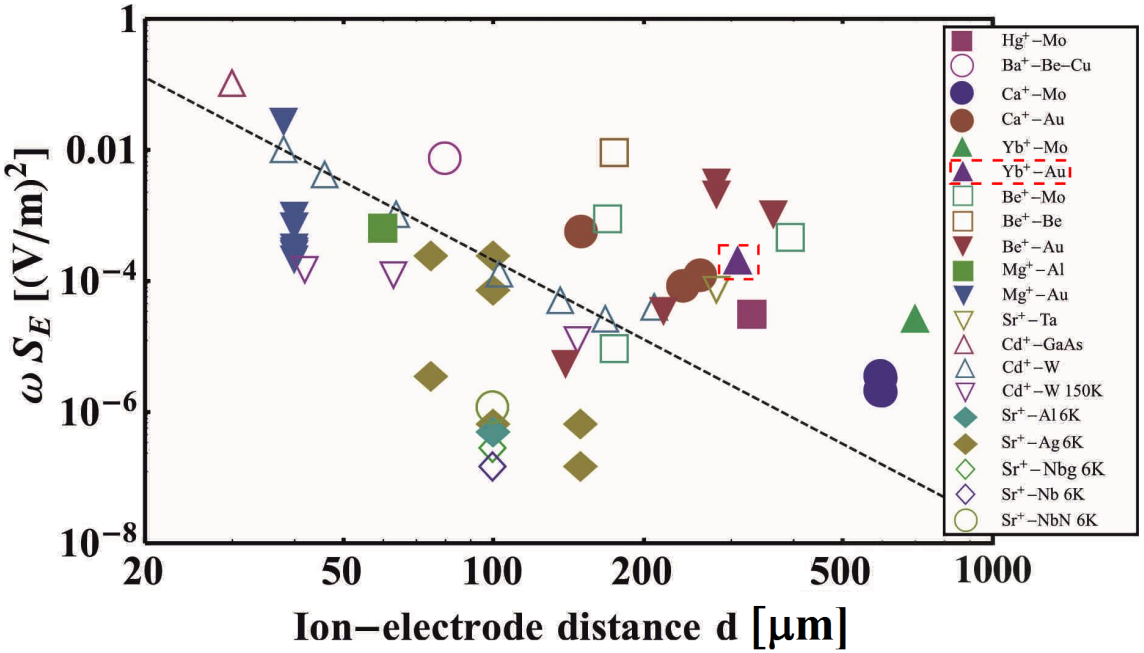

Figure 7.8: (Figure taken from [3]) Previously published measurements of motional heating plotted as the product of electric field noise spectral density $S_E(\omega)$ and the secular frequency ω, versus ion-electrode distance, r. A $1/r^4$ trend line is also shown. Each label shows both the ion species and the electrode material used and the electrode temperature is also noted if the measurement is performed below room temperature. The result obtained in this work is indicated by the dashed box. The data points are associated with the following references. (Hg^+−Mo [74], Ba^+−Be-Cu [75], Ca^+−Mo [76], Ca^+−Au [77, 78, 79], Yb^+−Mo [80], Yb^+−Au [81], Be^+−Mo [66], Be^+−Be [66], Be^+−Au [66, 82], Mg^+−Al [83], Mg^+−Au [31, 83, 84, 85, 86], Cd^+−GaAs [32], Cd^+−W [73], Cd^+−W 150 K [73], Sr^+−Al 6 K [87], Sr^+−Ag 6 K [88], Sr^+−Nbg 6 K, Sr^+−Nb 6 K, Sr^+−NbN 6 K [87])

Chapter 8

Two-dimensional ion trap surface array design optimisation for an analogue quantum simulation

8.1 Introduction

Trapped ions possess long lived addressable internal states and can be highly decoupled from their environment. This makes them an important tool in the development of quantum information processing [57, 89] and quantum simulation [90, 91, 92, 93, 94]. When used for quantum simulation they enable complex spin systems, among others, to be investigated beyond the practical limitations of classical computation. For example, trapped ions have been used for quantum simulations of the evolution of paramagnetic into (anti-)ferromagnetic order in a spin system, [95, 96] and frustrated anti-ferromagnetic Ising interactions, [97, 98]. These first simulations were carried out using one-dimensional trapping arrays and state dependant forces applied using laser beams.

More complex simulations will require ions trapped in 2D arrays and interaction schemes compatible with these. Advances towards 2D trapping arrays suitable for quantum simulations have been made by trapping ions in a millimetre-scale mechanically fabricated metal mesh [61] and by the successful implementation of microfabrication techniques for ion traps [3]. In addition, interaction schemes based on large oscillating or static magnetic field gradients have been proposed [99, 100] and demonstrated in an on-chip microwave gate [29, 101]. With the recent advances in the field, ion trap quantum simulations using large scale 2D ion trap lattices are within the reach of current technology.

In order to create a 2D array of trapped ions a repeating 2D surface geometry is re-

quired. Decoherance due to anomalous heating is a major issue for large scale quantum simulations. As this heating scales approximately as r^{-4} [66], where r is the ion height above the trapping surface, it is advantageous for ions to be trapped high above the surface. However, when individual surface microtraps are placed together so that their separation is less than around twice the ion height the individual electric fields start to overlap and distort the resulting trapping fields [102]. In extreme cases this can lead to the traps combining to produce a singular trapping zone. To compensate for this the electrode structure has to be altered when operating within this regime [102]. Schmied et al. [102] have investigated surface-electrode geometries and developed an algorithm that optimises geometries to maximise the electric field curvatures of individual trapping sites for arbitrary ion heights and separations. Individual trapping sites shown in [102, 103] were optimised using this algorithm leading to non-intuitive electrode patterns which can contain many isolated radio-frequency (rf) and static voltage electrodes. Another proposal [104] working outside this regime uses rf electrodes with controllable rf voltages to lower trap frequencies and decrease ion-ion distances and, therefore, increase interaction strengths. However, this requires the use of multiple independent rf electrodes and individually controllable rf voltages posing an additional experimental complication.

This works presents an optimisation process for ion trap topologies based on a single rf electrode island, reducing the requirement for buried rf wires and multiple rf electrodes. A focus is made on the development of an optimum lattice geometry where the ratio of coupling rate to the decoherence rate due to ion heating is maximised and made homogeneous across the lattice. This is achieved by minimising the secular frequencies of the trapping sites whilst, simultaneously, keeping the trapping depths above a minimum trap depth (for illustrative purposes we use 0.1eV) to allow for successful operation of the proposed 2D lattice designs. We will concentrate on the optimum lattice topology for hexagonal, square and centred rectangle lattices. An investigation is also carried out on how optimal geometries depend on the overall lattice size, and we discuss the choice of and scaling for experimental parameters such as rf voltage, drive frequency, ion mass and electric field noise density.

Additionally it is possible that two-dimensional ion arrays of this type could also be used for quantum computation. For example, cluster state quantum computation could be carried out in such a system [105, 106]. However, additional constraints may also have to be taken into account.

8.2 Ion-ion interactions and Lattice Geometry

8.2.1 Ion-ion interactions

Two-dimensional lattices of ions can be used as a quantum simulator for many body spin-1/2 systems [59]. Forces such as the trapping potential, $F_T = -m\omega_i^2$, and the coulomb force, $F_C = -e^2/(4\pi\epsilon_0 A^2)$, between the individual ions determine the equilibrium position. Laser beams or magnetic field gradients can be used to impart an additional force to the ions which displace the ion(s) depending on its internal state. This displacement leads to a change in the coulomb force and thereby displaces the neighbouring ion(s) dependent on their own internal state. This state dependant coupling is given by [59]

$$J = \frac{\beta F^2}{m\omega^2} \tag{8.1}$$

where m is the mass of an ion, F is the magnitude of the state dependant force applied to each ion and ω is the trap's secular frequency. Exactly how this force is applied will be discussed later in the chapter. β is the ratio of the change in the Coulomb force to the change in the restoring force due to the displacement of the ions caused by the state dependant force and is given by [59]

$$\beta = \frac{e^2}{2\pi\epsilon_0 m\omega^2 A^3}, \tag{8.2}$$

where A is the ion-ion spacing. There are two cases to consider, when $\beta > 1$ the change in the Coulomb force, δF_C, due to the displacement of an ion is dominant over the change in the restoring force, δF_T. This results in an interaction over a large number of trapping sites. When $\beta < 1$, the opposite is true resulting in an interaction which decays rapidly across the array. Trapping ions in a 2D array of microtraps makes it possible to satisfy the condition that $\beta < 1$ allowing systems with short range interactions to be simulated. An illustration of this system is shown in figure 8.1.

It is important to consider sources of decoherence when designing a 2D ion trap array. The internal state of an ion can remain coherent for 10's of seconds [22, 107]. However, motional decoherence due to anomalous heating of ions will be an important factor during quantum operations within small scale ion traps as the implementation of spin dependant couplings involves the use of motional states of the ion. The coupling, J, will be observable if the coupling time, $T_J = 1/J$, is less than the motional decoherence time in the system and, therefore, the ratio of these two times is an important parameter of the system and is given by

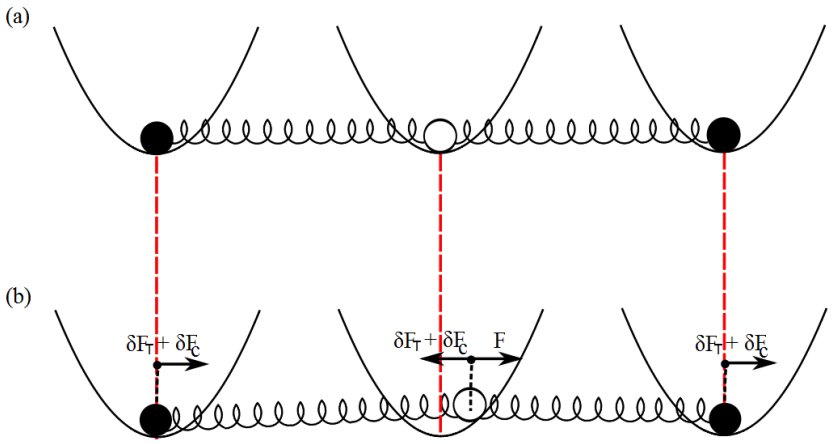

Figure 8.1: Pictorial diagram of three ions in adjacent traps. The ions feel a Coulomb force indicated by the springs between each ion and can be placed in two different states indicated by their colour. (a) Pictorial diagram showing the case with no state dependent force present. (b) Pictorial diagram showing how the system reacts to the presence of a state dependent force, F. Here the ions feel a change in the Coulomb force, δF_C, due to the displacement of the ions and a change in the restoring force, δF_T.

$$K_{sim} = \frac{T_{\dot{n}}}{T_J} \tag{8.3}$$

where [66],

$$T_{\dot{n}} = \frac{4m\omega\hbar}{e^2 S_E(\omega)}. \tag{8.4}$$

Here $S_E(\omega)$ is the electric field noise density [3, 66]. In order for an interaction to occur on faster time-scales than the decoherence in the system, it is required that $K_{sim} > 1$ and it is the aim of the optimisation process presented in this work to optimise the geometry in order to maximise this parameter. To acquire an understanding of how a geometry can affect K_{sim} it is necessary to determine its form with respect to the geometry variables. The form of T_J can be found by substituting equation 8.2 into 8.1 and is given by

$$T_J = \frac{2\pi\epsilon_0 m^2\omega^4 A^3\hbar}{e^2F^2}. \tag{8.5}$$

The K_{sim} parameter can then be expressed as

$$K_{sim} = \frac{2F^2}{S_E(\omega)\pi\epsilon_0 m\omega^3 A^3}. \tag{8.6}$$

The secular frequency, ω, of a trapped ion [39] can be expressed as a function of α defined as

$$\alpha = \frac{V}{\Omega} \tag{8.7}$$

where V is the amplitude of the rf voltage applied to the trap and Ω is 2π times the drive frequency in Hz, yielding,

$$\omega = \frac{eV\eta_{geo}}{\sqrt{2}m\Omega r^2} = \frac{e\alpha\eta_{geo}}{\sqrt{2}mr^2} \tag{8.8}$$

where r is the height of an ion above the surface, e is the charge of an electron and η_{geo} is an efficiency factor which can range between zero and one depending on the form of the geometry [39].

The secular frequency given in equation 8.8 can then be used along with $S_E(\omega) = \Xi r^{-4}\omega^{-1}$, where Ξ is a coefficient that can be experimentally obtained and depends on the temperature and surface of the trap electrodes (see [3] for a listing) to re-express equation 8.6 in the form

$$K_{sim} = \frac{4F^2mr^8}{\Xi\alpha^2\eta_{geo}^2\pi\epsilon_0 A^3}. \tag{8.9}$$

To further understand how the geometry effects the K_{sim} value the parameters of a lattice geometry will now be introduced and related to equation 8.9.

8.2.2 Two-dimensional ion trap lattice geometry

A lattice is a regular tiling of a space by a primitive unit cell. Previous works [61, 104] concentrate on lattices created from square unit cells. In total there exist five types of cell which can be used to form a 2D lattice: centred rectangular, hexagonal and square as shown in figure 8.2, and rectangular and oblique [108]. The rectangular and oblique structures are not considered in this work due to their non-uniform ion-ion distances.

Figure 8.2 shows the polygon-polygon separation which is equal to the ion-ion distance, A, in equation 8.9. The polygon radius, R, along with the separation, will determine the height above the surface at which the ion is trapped, r, with larger polygon radii yielding higher ion heights. Another variable to be considered is the gap between the outer polygon in the array to the edge of the rf electrode, g. This can be used to alter the homogeneity of the individual trapping sites within the array. In general a non-homogeneous system results in spin dependant coupling rates which are a function of the lattice site, posing a significant problem for the scalability of such an array [109].

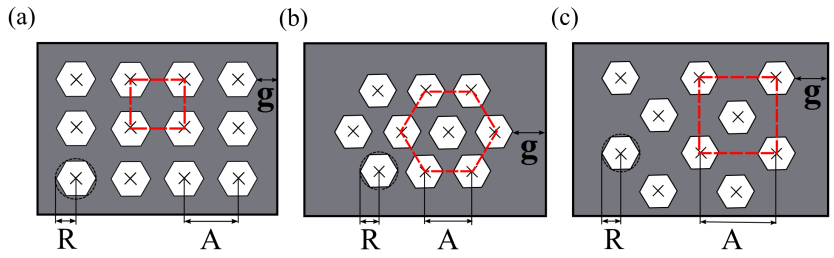

Figure 8.2: Diagrams showing the polygon radii R, the separation between the polygon centrers, A, and the distance between the last polygon and the edge of the rf electrode (shown in grey), g. (a) Diagram showing a three by four ion trap surface array consisting of six sided polygons arranged with square unit cells. (b) Diagram showing a similar surface array arranged into hexagonal unit cells. (c) Diagram showing a surface array arranged into centred rectangular unit cells. The unit cells are indicated by dashed lines.

8.3 Simulation of lattices

To determine the electric field produced by a two-dimensional array a method based on the Biot-Savart like law described by Oliveira and Miranda [2] was used. This method calculates the electric field produced by an arbitrarily shaped two-dimensional electrode which is held at a potential V whilst the rest of the plane is held at a potential of zero. The electric field observed at a given point, $\overline{X}$, in space due to such an area held at a potential and bounded by a path C is given by [2]

$$E_{(\overline{X})} = \frac{V}{2\pi} \oint_C \frac{(\overline{x} - \overline{x}') \times d\overline{s}}{|\overline{x} - \overline{x}'|^3} \tag{8.10}$$

where the curve, C, bounds the electrode and $\overline{x}'$ and $\overline{x}$ are vectors that locate the source point and field point respectively. By calculating the electric field in this manner an assumption is made that there is no gap between the areas held at the potential, V, and the areas held at zero. In microfabricated surface traps, gaps between the electrodes are required and typically range from 3μm - 10μm [3]. If, however, these gaps are small in comparison to the electrode structures they will not alter the trapping fields significantly [1, 85, 110]. The electric fields of individual electrodes can then be combined to determine potential nils and, therefore, trapping positions in the 2D trap arrays, using the numerical Gauss-Newton algorithm. The secular frequencies, trap depths and ion heights at these positions can then be determined.

To calculate the error of the numerical integration simulations of five wire symmetric surface trap geometries with different central static electrode and rf rail widths in the

gapless plane approximation using the method of Oliveira and Miranda [2] were compared to results obtained with analytical equations described by House [1]. In all the geometries simulated the two rf rails were of equal width. Similarly to House, the outer static voltage electrodes were approximated as an infinitely long ground plane although the length of the inner rails were set to 3000 μm instead of infinite. A selection of these simulation results are shown in table 8.1.

Electrode parameters				Simulations		House equations	
rf width [μm]	central static electrode width [μm]	rf Volt. [V]	rf freq. [MHz]	r [μm]	ω [MHz]	r [μm]	ω [MHz]
100	50	250	75	55.8	6.86	55.9	6.87
100	50	500	60	55.8	4.29	55.9	4.29
200	100	250	30	110.1	2.17	111.8	2.20
200	100	500	40	110.1	3.26	111.8	3.30
500	150	250	20	165.4	1.48	167.7	1.52
500	150	500	25	165.4	2.37	167.7	2.43

Table 8.1: Table showing the secular frequency, ω, and ion height, r, for different five wire surface trap geometries as calculated by the analytical method in House [1] and simulated by the method used in this work based on the Biot-Savart like law [2].

In these results a general error for the ion heights and secular frequencies of less than 2% and 3% respectively was found, which leads to a maximum error in K_{sim} of 10%. For the following simulations it is therefore assumed that the maximum K_{sim} error is 10%. Additionally, numerical simulations of the geometries were carried out using methods described in [111], which indicate similar errors and trends for the ion height and secular frequency as the results obtained with the Biot-Savart like method.

8.4 Lattice geometry optimisation

In this section it will be shown how the parameters of the lattice geometry (discussed in section 8.2.2) can be optimised to achieve the highest possible K_{sim} value across the array for a given set of experimental parameters. To do this, it is first shown how the homogeneity of individual site properties over an array can be maximised by varying the distance between the outer polygon in the array to the edge of the rf electrode, g, and then shown how this scales with lattice size. These homogeneous arrays will then be used

to calculate the optimum number of sides, n, a polygon within the array should possess in order to maximise K_{sim}. A method will then be outlined describing the optimisation of the polygon radii, R, and separation, A, of an array and show how these vary with increased lattice size and ion mass.

8.4.1 Increasing the homogeneity of K_{sim} across the array

This is achieved by ensuring homogeneous secular frequencies, ion heights and trap depths across all the array sites. As shown in figure 8.3 the K_{sim} of trapping sites in an array can be altered to approach a common value if the distance, g, between the edge of the outer polygon and the edge of the rf electrode containing the polygon array is adjusted. As the value of g is increased, the K_{sim} value of the sites towards the centre drop, however, the outer sites K_{sim} value rises, resulting in the properties converging towards each other. If the distance g is increased further beyond the point at which maximum homogeneity occurs the outer site properties drift away from those of the central sites and, therefore, decrease the homogeneity of the array.

To provide a value of g which is universal for all lattice sites, its value is given in units of lattice side length, L. The lattice side length is determined by the polygon separation, A, and radius, R, and can be expressed as

$$L = (M-1)A + 2R, \tag{8.11}$$

where M is the number of lattice sites along one side of an array.
In order to quantify the array's homogeneity, H is defined as the average deviation of K_{sim} of each lattice site from the K_{sim} of the central site and is given by

$$H = \frac{1}{N}\sum_{n=1}^{N}\left|1 - \frac{K_{sim_n}}{K_{sim_{centre}}}\right| \tag{8.12}$$

where N is the total number of trapping sites in the lattice.

Figure 8.4 shows H for a five by five square type unit cell lattice for $0 < g/L < 1.5$. The maximum homogeneity, and thus the optimum g/L, is found when H is minimised. The error associated with H is given by

$$\sigma_H = \frac{\sqrt{N(\sigma_{Ksim})^2 + N(\sigma_{Ksim_{centre}})^2}}{N} \tag{8.13}$$

where the error on all K_{sim} values is 10%, as shown in section 8.3. This yields an overall percentage error on H of $0.13/\sqrt{N}\%$.

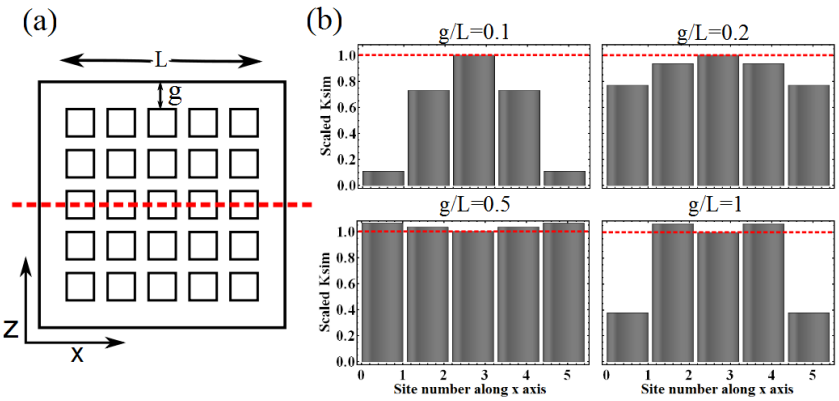

Figure 8.3: Diagram showing the effect of varying the distance g on the scaled K_{sim} value of the individual trapping sites. The K_{sim} values shown are scaled with that of the central site. (a) Representation of a 5 by 5 square type lattice array indicating the axis labelling. (b) Slices across the array (indicated by the dotted line in (a)) for g/L values of 0.1, 0.2, 0.5 and 1.

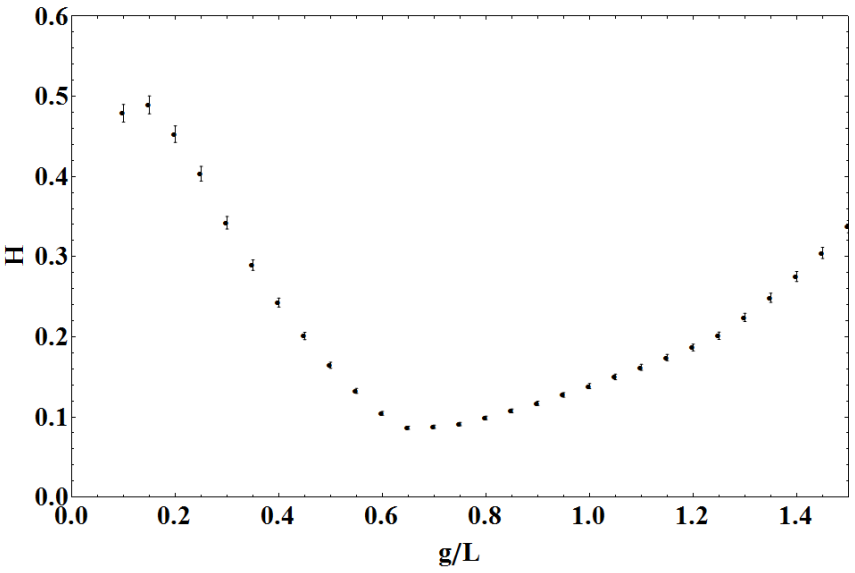

Figure 8.4: Graph showing the average deviation of the K_{sim} of each lattice site from the K_{sim} of the central site, H, for a five by five square type unit cell lattice for $0 < g/L < 1.5$. The error on H is given by $\frac{0.13}{\sqrt{N}}H$ and the error of the minimum of H is determined by observing the spread of g/L which agrees, within error, with the minimum position.

Lattice Type	a	b	B
Square	0.20±0.01	5.21±0.38	0.74±0.03
Hexagonal	0.39±0.08	3.76±1.40	0.54±0.14
Centre Rectangular	0.31±0.04	7.84±2.43	0.76±0.11

Table 8.2: Table showing a and b values for the fits which describe g/L as a function of the number of sites in the lattice.

Figure 8.5 shows the optimum g/L for hexagonal, central rectangular and square unit cell lattices of different sizes. The curves are found to be described by an equation of the form $g/L = a + bN^{-B}$ with a, b and B values for different lattice types shown in table 8.2. For large lattices, g/L is independent of N, as trapping sites close to the edge of the lattice are influenced only by the electric field created by that edge. In small lattices, however, the optimum g/L increases as the effect of the electric field from the opposite edge of the lattice increases.

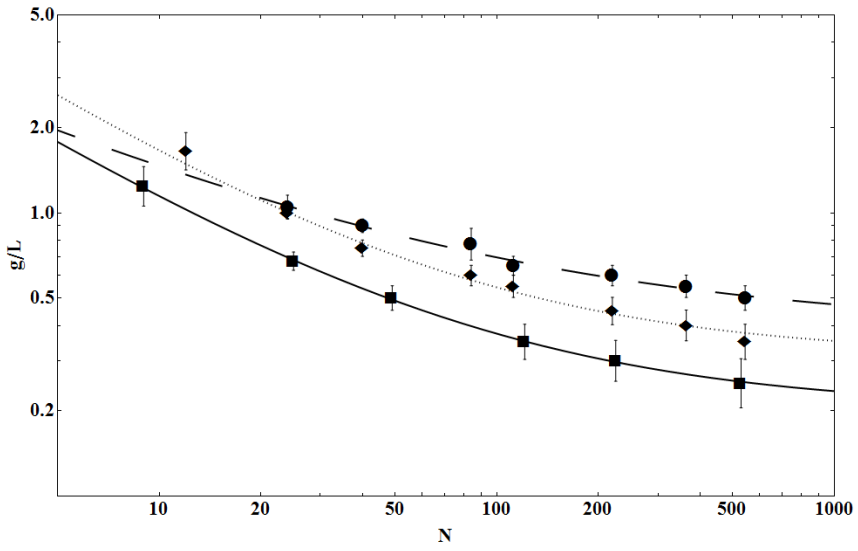

Figure 8.5: Graph showing the optimum g/L as a function of the total number of trapping sites, N, for square lattices (square markers), hexagonal lattices (circular markers) and centre rectangular lattices (diamond markers). The curves are given by $g/L = a + bN^{-B}$ with a, b and B values for different lattice types shown in table 8.2.

8.4.2 Optimising the number of polygon sides

An investigation will now be carried out to find the optimum number of polygon sides, n, which provide the highest K_{sim} value on the central trapping site (located above the

central polygon) of a lattice. This is important as the time taken to simulate a geometry is a function of the number of sides in a polygon. It is, therefore, advantageous from a simulations point of view to keep the number of polygon sides to a minimum without compromising the functionality of the resultant geometry.

To ensure the results are universal for all lattice geometries, g/L is set to the value which maximises the homogeneity of each array, and all other parameters are scaled by normalising K_{sim} to that of an identical geometry with polygons of 100 sides. This also allows comparison between the different types of lattices.

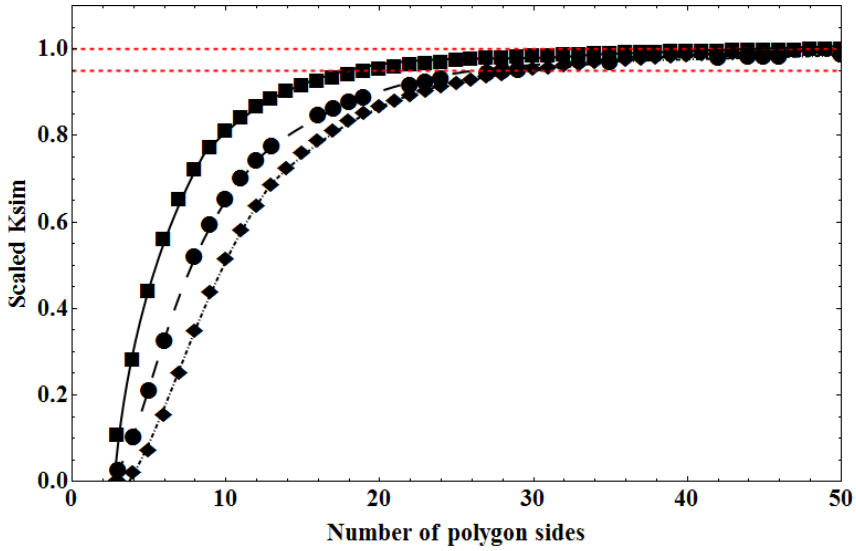

Figure 8.6: Graph showing the relationship between the number of polygon sides and K_{sim} for square (square markers), hexagonal (circular markers) and central rectangular (diamond markers) unit cell lattices. The dashed lines show the values of 1 and 0.95 of the scaled K_{sim} value.

Figure 8.6 shows the scaled K_{sim} for the central site as the number of polygon sides is varied. As the number of sides is increased the value of K_{sim} approaches an asymptote, shown by the upper dashed line. This indicates that the best geometry will be made from circular electrodes. However, simulation times grow with increasing polygon side number and so it is advantageous to reduce this number to a minimum. It is shown that 95% of the maximum achievable K_{sim} (indicated by the lower dashed line) can be achieved with around $\geq$ 25-30 sides in the polygons.

8.4.3 Optimisation method for polygon separation and radius

In this section it will be shown how to maximise the K_{sim} of any arbitrary geometry. Optimum geometries will then be determined and it will be shown how they scale and,

ultimately, are determined by $\alpha = V/\Omega$. In all the geometries discussed here the value of g used is that determined in section 8.4.1 in order to provide the maximum K_{sim} homogeneity across the lattice, and the number of polygon sides is set to 25 as this provides a good approximation to the optimum circular geometry while keeping the simulation time at a minimum, as shown in section 8.4.2.

When considering any fixed arbitrary geometry, equation 8.9 shows that K_{sim} can be maximised by reducing the value of α. However, the minimum achievable α is limited by the lowest usable trap depth, as the trap depth is proportional to α^2 and is given by

$$T_D = \frac{\zeta e^2 \alpha^2}{\pi^2 m} \tag{8.14}$$

where e is the charge of an ion and ζ is a geometrical factor which is a function of A and R [1].

Optimal geometries, which we define as geometries which yield the highest value of K_{sim} for a given value of α, will now be found. This will be carried out by fixing the trap depth at a reasonable minimum value (0.1 eV is used here for illustration purposes) which, as discussed above, provides the maximum K_{sim} for a given geometry, and then investigating the dependence of polygon radius, separation and ion height with α. To determine these dependencies a K_{sim} contour plot is made by calculating the K_{sim} over a range of polygon separation, A, and radius, R, with a resolution of $1\mu m$. The range of polygon radius and separation used should not create traps with inter-well barriers of less than the minimum trap depth value, and to ensure this the polygon radius was kept to less than a third of the polygon separation. For each combination of polygon separation and radius a value of α is found which yields the minimum trap depth and, thus, maximises the K_{sim} of the particular geometry. By following this method one can obtain the α required to achieve the minimum trap depth, the ion height, r, and K_{sim} for each geometry. From the resulting data the polygon separation and radius which yields the highest K_{sim} for a given α (the optimum geometry) can then be found. A graphical example of such data is shown in figure 8.7.

It can be seen from this method and the example data in figure 8.7 that the highest K_{sim} will be achieved with an infinite value of α, R and A. However, other effects may limit the magnitude of α. In order to determine a limit on α it is, therefore, necessary to describe the various array and trapping field dependant properties (such as secular frequency, ion height and K_{sim}) in terms of α.

By plotting these optimum parameters (polygon radius, separation and ion height) as

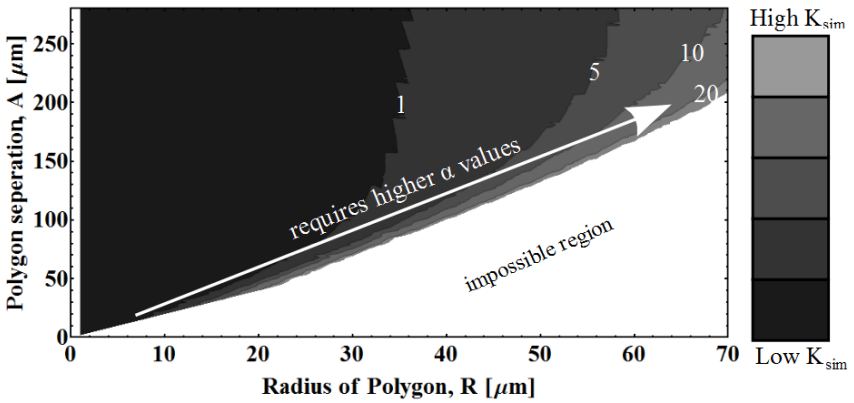

Figure 8.7: Example graph showing how the K_{sim} (absolute values indicated by numbers on contour lines) varies as a function of polygon radius and separation. The graph also indicates that the value of α increases as the radius and separation are increased. This data was obtained using the method described in section 8.4.3 with a polygon separation and radius resolution of 1μm and a minimum trap depth of 0.1 eV. The value of α in the figure ranges from zero to $5/\pi$ VMHz^{-1}. The impossible region describes geometries where individual trapping sites start to combine to a single one and so possess a polygon radius, R, greater than or equal to a third of the polygon separation, A.

a function of α, as shown in figures 8.8(a), (b) and (c), linear relationships of the form

$$r = k_r \alpha \tag{8.15}$$

$$A = k_A \alpha \tag{8.16}$$

and

$$R = k_R \alpha \tag{8.17}$$

are found for the optimal geometries. The values of k_r, k_A and k_R are dependant on the number of trapping sites in an array, as shown in figures 8.9(a),(b) and (c) respectively, for lattices made from square type unit cells of polygons.

It is important to stress that equations 8.15, 8.16 and 8.17 are only valid in the case of optimal geometries, which depend solely on α. With this in mind, it is now possible to re-express the secular frequency in equation 8.8 to describe the secular frequency of an optimised geometry as:

$$\omega = \frac{e\eta_{geo}}{\sqrt{2}k_r^2 m\alpha}. \tag{8.18}$$

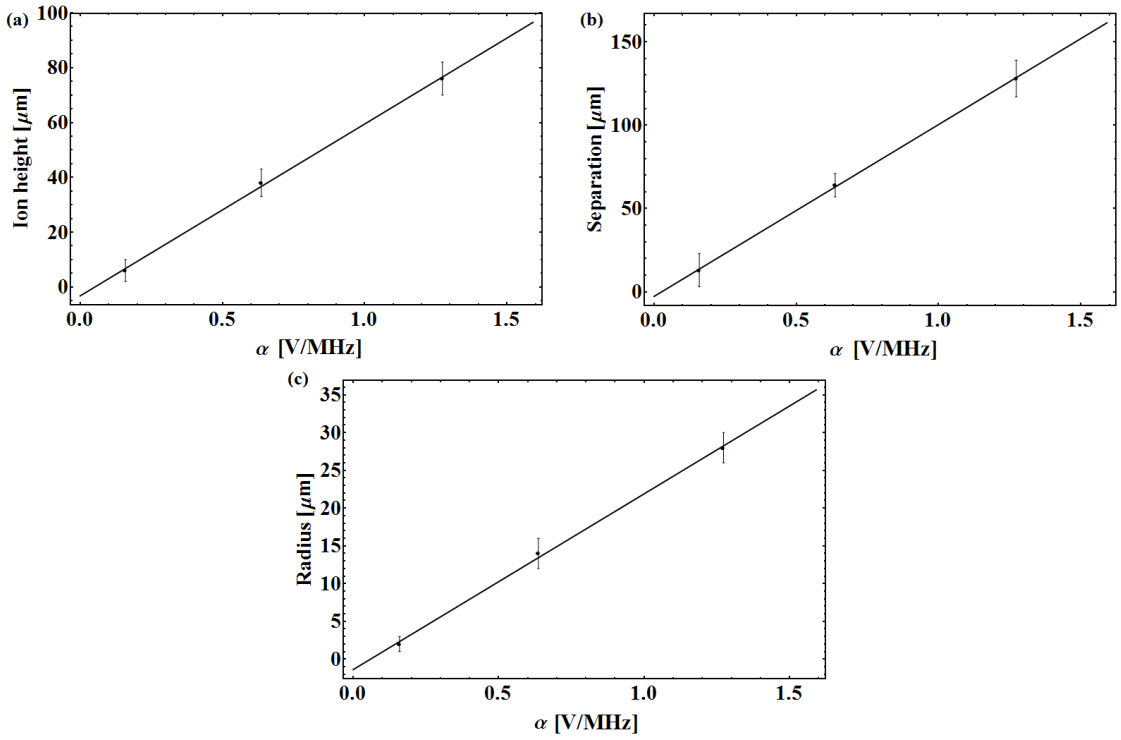

Figure 8.8: Graphs showing the ion height (a), polygon separation (b) and polygon radius (c) of an optimised lattice as a function of the ratio α. In all cases the plots are shown using $\alpha = V/\Omega$ where Ω is 2π times the drive frequency in Hz, and for arrays made from square type unit cells of polygons with 81 sites and for $^{171}Yb^{+}$ ions.

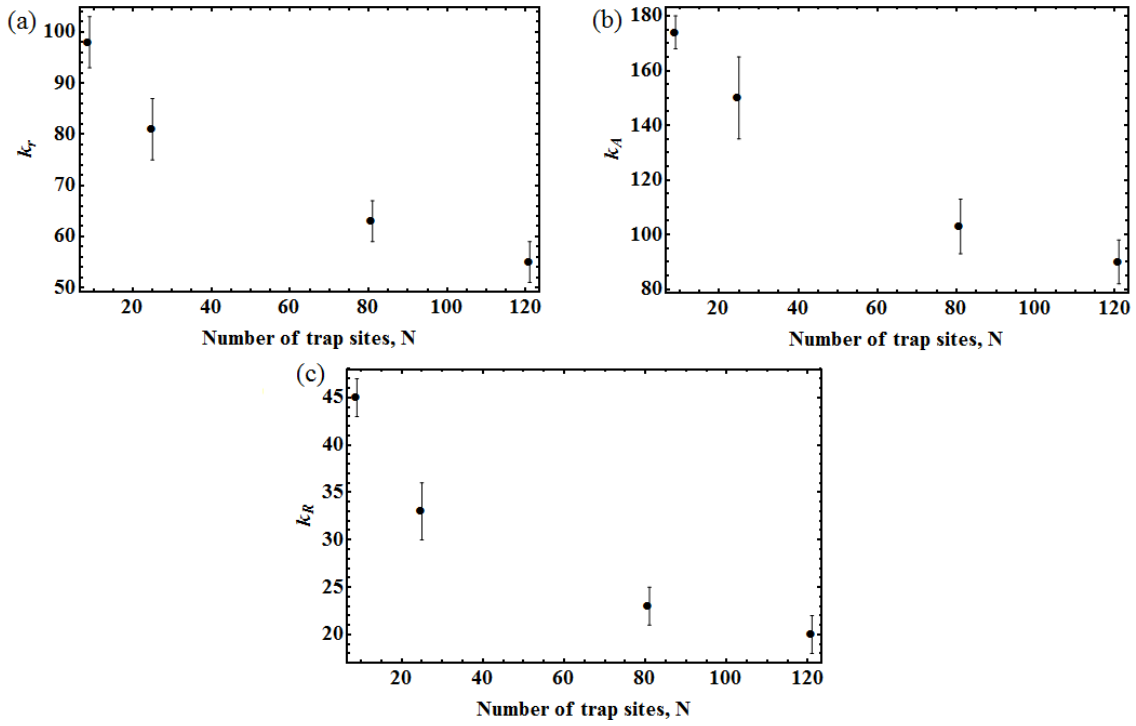

Figure 8.9: Graphs showing the value of k_r (a), k_A (b) and k_R (c) as a function of the number of trapping sites, N. In all cases the plots are shown using $\alpha = V/\Omega$ where Ω is 2π times the drive frequency in Hz and are for arrays made from square type unit cells of polygons using $^{171}Yb^{+}$ ions.

K_{sim} in equation 8.9 can also be re-expressed to describe that of an optimised geometry:

$$K_{sim} = \frac{4F^2 m k_r^8 \alpha^3}{\Xi \eta_{geo}^2 \pi \epsilon_0 k_A^3}. \tag{8.19}$$

Equation 8.19 shows that, for optimal geometries, K_{sim} is proportional to α^3 (as the value of α determines the electrode dimensions to be used) and so, to produce an array with a high K_{sim} for a given number of lattice sites (as k_r and k_A are a function of the number of trapping sites), a large value of α is preferable. Equations 8.16 and 8.17 show that the optimum geometry size is proportional to α. It, therefore, follows that larger lattice geometries will produce larger values of K_{sim}. This effect is illustrated in figure 8.7 which shows the K_{sim} as a function of polygon radius and separation. For optimised lattices, the optimal radius and separation will fall on a line described by $A = (k_A/k_R)\, R$, with higher values of α required for higher values of separation and radius as shown in equations 8.16 and 8.17 respectively.

The heating rate in ion traps has a strong dependency on the ion height ($\propto 1/r^4$) [66]. A large K_{sim} is achieved with large values of α, resulting in large ion heights, as shown in equation 8.15. It, therefore, can be concluded that a different scaling of the heating rate (for example in cryogenic systems) does not change the optimisation process and optimal geometries.

It has now been shown that the optimal geometry for a given minimum trap depth and ion mass is determined solely by the value of α.

Optimal geometries and their K_{sim} values (in units of $1/\alpha^3$) can now be found by creating contour plots (such as shown in figure 8.7) for different values of lattice size, N, lattice unit cell type and ion mass, m. The error on the K_{sim} value, calculated from equation 8.9, was determined to be $\pm 10\%$ by comparing the secular frequency and ion heights obtained using the program with those predicted by House's analytical solutions for a five wire surface trap geometry [1].

8.5 Optimisation results and analysis

In this section, optimum polygon separations, A, and radii, R, are obtained using the method outlined above for square, hexagonal and centre rectangular unit cell type lattices. These are shown as function of lattice sizes and ion masses with the experimental constraint, α, scaled out. Throughout this optimisation example, $^{171}Yb^+$ ions will be used unless otherwise stated.

Lattice Type	c	d	E
Square	-5±1	101±7	0.29±0.03
Hexagonal	1±3	85±6	0.40±0.08
Centre Rectangular	-2±2	68±6	0.34±0.05

Table 8.3: Table showing c, d and E values for the fits which describe R/α as a function of the number of sites in the lattice.

Figure 8.10 shows how the optimum scaled radius, R/α, and separation, A/α, of polygons vary as a function of lattice size for $^{171}Yb^{+}$ ions. As explained in the previous section a minimum trap depth of 0.1 eV has been assumed for illustrative purposes. It can be seen from this figure that as the size of the lattice increases, the optimum polygon radius and separation asymptotically tend towards values representative of an infinitely large lattice. This is expected as once a lattice becomes large enough, the addition of extra lattice sites will represent only a small change in the overall electrode geometry and, therefore, produce a small change in the electric field produced by the geometry. When the lattice is small however, additional lattice sites will represent a larger change in the geometry and will, therefore, cause a larger change in the electric field. Figure 8.11 shows how the scaled $K_{sim}/(F^2\alpha^3)$ scales as a function of the number of lattice sites, N, using scaled optimum polygon radii, R/α, and separations, A/α. The state dependant force F will be considered in more detail in section 8.6.2. Due to the dependency of K_{sim} on the geometry, the relationship between $K_{sim}/(F^2\alpha^3)$ and the number of sites is expected to be of similar form to that for optimal polygon radii, R/α, and separation, A/α, with the maximum $K_{sim}/(F^2\alpha^3)$ asymptotically tending towards a value representative of an infinitely large lattice.

Using the data shown in figures 8.10(a), 8.10(b) and 8.11 the optimum radii and separation of the polygons as a function of number of sites, N, were found to follow a $c + dN^{-E}$ and $f + gN^{-G}$ relationship, respectively, while the maximum $K_{sim}/(F^2\alpha^3)$ follows a $k + lN^{-Q}$ trend. The values of c, d, E, f, g, G k, l, and Q are shown in tables 8.3, 8.4 and 8.5.

Using the data shown in figures 8.12(a) and 8.12(b) the optimum radii and separation of the polygons as a function of mass were found to follow a $o + pm^{-0.5}$ and $q + sm^{-0.5}$ relationship, respectively, with values of o, p, q and s shown in tables 8.6 and 8.7. Figure 8.13 shows how the optimum $K_{sim}/(F^2\alpha^3)$ varies as a function of the mass of the trapped ion, m, for 220 (square type unit cells) and 225 (hexagonal and centre rectangular type

Lattice Type	f	g	G
Square	-136±7	457±5	0.15±0.01
Hexagonal	13±24	547±288	0.48±0.21
Centre Rectangular	40±15	831±282	0.57±0.13

Table 8.4: Table showing f and g and G values for the fits which describe A/α as a function of the number of sites in the lattice.

Lattice Type	k	l	Q
Square	$-(2.69\pm2.97)\times10^{34}$	$(3.09\pm1.31)\times10^{36}$	(0.61±0.13)
Hexagonal	$(0.52\pm6.00)\times10^{33}$	$(3.51\pm1.54)\times10^{36}$	(0.86±0.12)
Centre Rectangular	$-(3.09\pm6.12)\times10^{35}$	$(5.23\pm5.11)\times10^{37}$	(0.65±0.26)

Table 8.5: Table showing k, l and Q values for the fits which describe $K_{sim}/(F^2\alpha^3)$ as a function of the number of sites in the lattice.

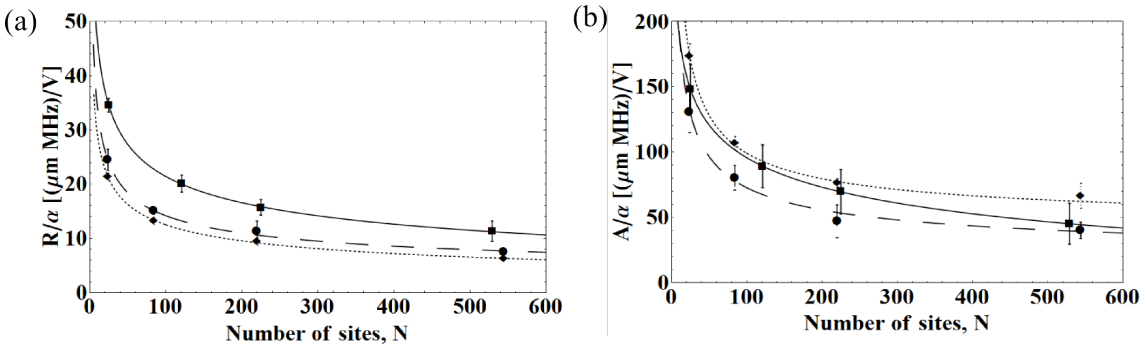

Figure 8.10: (a) Graph showing how the optimum polygon radius, R/α, varies as a function of the number of sites. (b) Graph showing how the optimum polygon separation, A/α, varies as a function of the number of sites. For both (a) and (b) the results shown are for square (square markers), hexagonal (circular markers) and centre rectangular (diamond markers) unit cell lattices with $^{171}Yb^{+}$ ions.

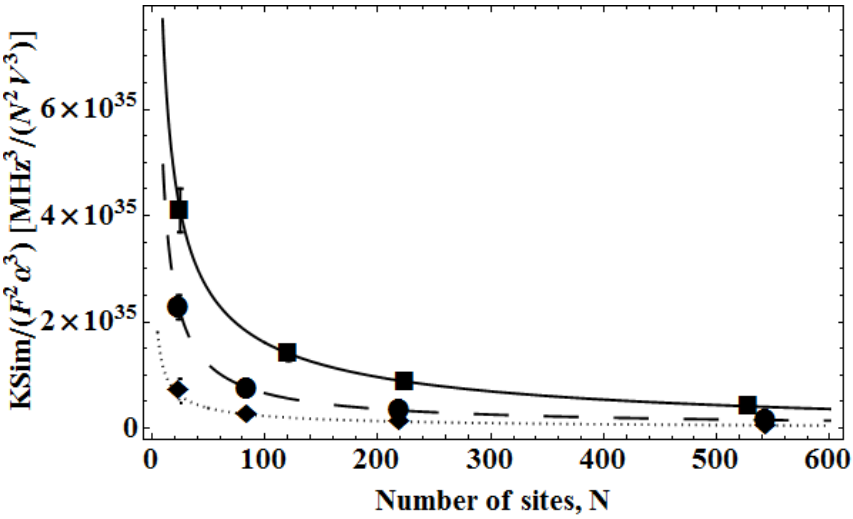

Figure 8.11: Graph showing how the optimum $K_{sim}/(F^2\alpha^3)$ varies as a function of the number of sites for optimum lattices with $^{171}Yb^+$ ions. This is shown for square (square markers), hexagonal (circular markers) and centre rectangular (diamond markers) unit cell lattices. Here F is a state dependant force applied to the ions in the lattice.

Lattice Type	o	p
Square	-56±6	138±10
Hexagonal	-34±7	88±11
Centre Rectangular	-48±3	110±6

Table 8.6: Table showing o and p values for the fits which describe R/α as a function of ion mass.

unit cells) trapping sites. It is found that the optimum $K_{sim}/(F^2\alpha^3)$ scales as $u + vm^{-0.5}$, with the values of u and v shown in table 8.8.

It should be noted, as shown in figure 8.12, that as the mass of the ion is increased, the polygon radii and separation will have to be decreased in order to provide trapping regions with a depth of above 0.1 eV for a given α for 220 (square type unit cells) and 225 (hexagonal and centre rectangular type unit cells) trapping sites. It is also clear to see that ions with lighter masses will provide higher $K_{sim}/(F^2\alpha^3)$ values but will require larger lattice geometries compared to heavier ions.

8.6 Constraints on α

In this section the considerations which could limit the value of α will be discussed. To do this it will be shown how the power dissipation in a chip trap, the quantum simulation

Lattice Type	q	s
Square	-176±47	489±65
Hexagonal	-311±15	678±22
Centre Rectangular	-402±28	911±51

Table 8.7: Table showing q and s values for the fits which describe A/α as a function of ion mass.

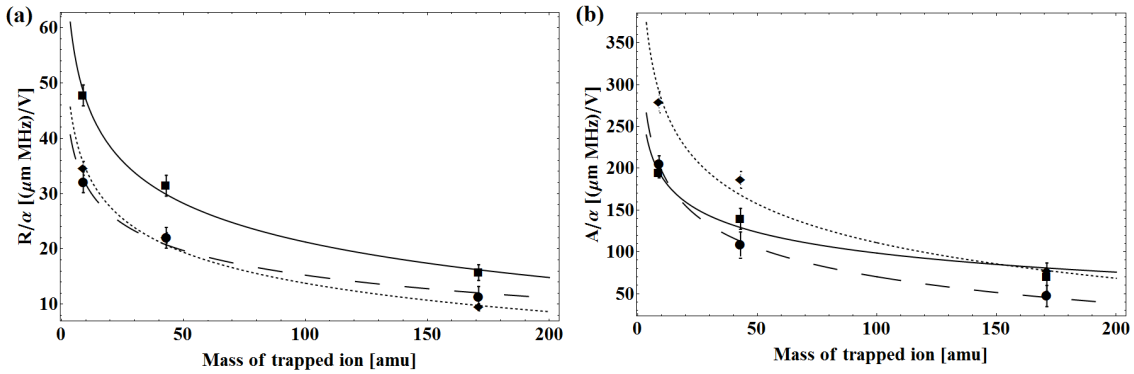

Figure 8.12: (a) Graph showing how the optimum polygon radius varies as a function of the ion mass for 220 (square type unit cells) and 225 (hexagonal and centre rectangular type unit cells) trapping sites. (b) Graph showing how the optimum polygon separation varies as a function of the ion mass. In both graphs this is shown for square (square markers), hexagonal (circular markers) and centre rectangular (diamond markers) unit cell lattices and the polygon radii and separations are scaled with α.

Lattice Type	u	v
Square	$-(5.25\pm3.00)\times10^{35}$	$(7.96\pm1.72)\times10^{36}$
Hexagonal	$-(1.25\pm0.60)\times10^{35}$	$(5.08\pm1.29)\times10^{36}$
Centre Rectangular	$-(2.56\pm1.28)\times10^{34}$	$(3.27\pm0.86)\times10^{36}$

Table 8.8: Table showing u and v values for the fits which describe $K_{sim}/(F^2\alpha^3)$ as a function of the ion mass.

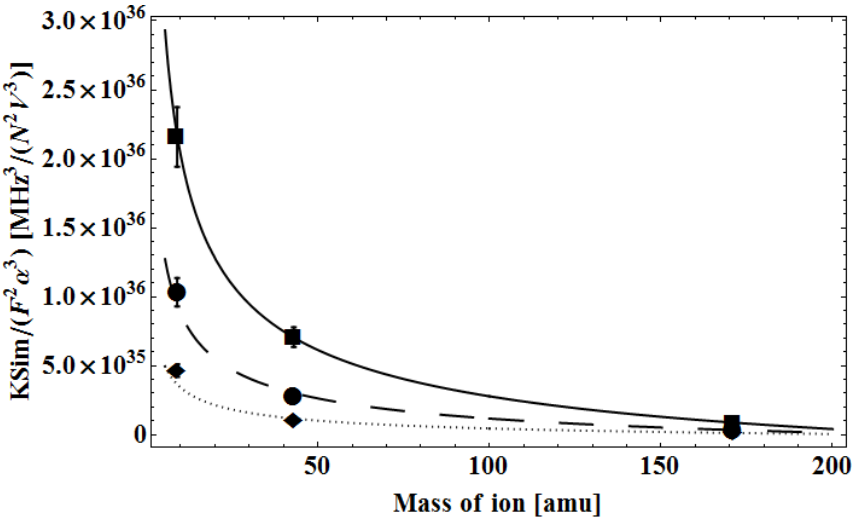

Figure 8.13: Graph showing how the optimum $K_{sim}/(F^2\alpha^3)$ varies as a function of the ion mass for 220 (square type unit cells (circular markers)) and 225 (hexagonal and centre rectangular type unit cells (square markers and diamond markers respectively)) trapping sites.

error and the interaction time vary as a function of α. This is important as from this a value of α can be determined for a given experiment, which will be shown in section 8.7.

8.6.1 Power dissipation in optimised arrays

The power dissipation of an ion trap chip is determined by the voltage, V, frequency, Ω, as well as the capacitance and resistance of the trap itself. This may, for a given capacitance and resistance, affect the value of α (the ratio between the rf voltage and drive frequency) which can be used. As the value of α is used to determine the optimum polygon radii and separation of a geometry, as shown in figure 8.10, for a given number of sites, N, and stability parameter, q, it is important to know how the power dissipation varies as a function of α.

The power dissipation of a chip is approximately given by [3]

$$P_D \approx \frac{1}{2}V^2C^2R\Omega^2, \tag{8.20}$$

where C and R are the capacitance and resistance of the chip. It is not possible to apply any combination of V and Ω to a geometry as they must be chosen so that the ion is stably trapped with a stability parameter given by [39, 61]

$$q = \frac{2e\eta_{geo}V}{mr^2\Omega^2} = \frac{2e\eta_{geo}\alpha}{mr^2\Omega} \tag{8.21}$$

between zero and 0.9, where e is the charge of an electron.

The ion height, r, of ions trapped in the optimised lattices shown in this work have been found to be linearly proportional to α. This relationship is shown in figure 8.8 (a) with the constant of proportionality, k_r found to be = 63(4) $\mathrm{mV^{-1}s^{-1}}$ for the example case of square type lattice with 81 sites using $^{171}\mathrm{Yb}^+$ ions. Considering one particular ion height, r_0, and substituting for $r_0 = k_r\alpha_0$ and rearranging equation 8.21 for Ω yields

$$\Omega_0 = \frac{2e\eta_{geo}}{mk_r^2\alpha_0 q}. \tag{8.22}$$

This equation can be re-expressed for V_0 by noting that $V_0 = \Omega_0\alpha_0$:

$$V_0 = \frac{2e\eta_{geo}}{mk_r^2 q}. \tag{8.23}$$

Equations 8.22 and 8.23 show that, for a given ion mass, m, ion height, r_0, stability parameter, q, and number of trapping sites in the array (as k_r is a function of the number of trapping sites), there is one unique voltage, V_0, and unique parameter α_0. This means that a given ion height (and, therefore, a chosen value of α) determines both the voltage and drive frequency to be applied to the trap.

To express the power dissipation, P_D, in terms of α equations 8.22 and 8.23 can be substituted into equation 8.20 giving

$$P_D = \frac{8\eta_{geo}^4 e^4 C^2 R}{k_r^8 m^4 q^4 \alpha^2}. \tag{8.24}$$

Equation 8.24 shows that as α is increased, the power dissipated is reduced. This means that the power dissipation is low for high values of α and, as high values of α provide high values of K_{sim} (see figures 8.11 and 8.13), power dissipation will not impact on producing high values of K_{sim} in optimised geometries. However, a low value of α will result in a high power dissipation in the chip and, so, the maximum allowable power dissipation in a chip will determine the lowest α which can be applied to a geometry.

8.6.2 Quantum simulation error

An upper limit on the value of α can be obtained from an estimation of the error of a quantum simulation using the method described in [112], where the error for the Ising model is given by

$$E_0 \approx \frac{1}{2}\eta^2 \sum_j (2\overline{n}+1) \left\langle \left[\left[O(t), \sigma_j^z(t) \right], \sigma_j^z(t) \right] \right\rangle. \tag{8.25}$$

Here $\overline{n}$ is the mean radial phonon number of the ions, O is the observable of the quantum simulation and η is a parameter which characterises phonon displacement caused by the state dependant force and is given by [112]

$$\eta = \frac{F\sqrt{\hbar/(2m\omega)}}{\hbar\omega} \tag{8.26}$$

where m is the mass of a trapped ion and $\omega/2\pi$ is its secular frequency.

If O is an M-site observable then there exist M non-vanishing commutators (for example a two-site correlation function ($M = 2$) or a spin average ($M = 1$)) and so the error on the simulation will not be dependant on the number of ions, N, in the array [112]. The error in equation 8.25 can now be re-written as

$$E_0 \approx \frac{F^2 M(\overline{n} + \frac{1}{2})}{2\hbar m\omega^3}. \tag{8.27}$$

Equations 8.19 and 8.27 show that both the K_{sim} and the error of the simulation, E_0, are proportional to the square of the state dependant force, F. It follows that the way in which this force is applied to the ions will determine the dependence of the simulation error on α. A discussion on the possible effects of the heating rate on the error can be found in Appendix A. In this work we will consider applying this state dependant force via laser beams and magnetic field gradients.

To calculate the laser power required to achieve a force, F, it is assumed, for illustrative purposes, that the laser beam is focused to a sheet given by 25 μm multiplied by the width of the array. The laser intensity required to provide a state dependant force, F, can be provided by a laser beam of power, P. If the output power of the laser used is assumed to be constant, then the force applied to the ions will be dependant on α. This is because the lattice size will increase with increasing α and, therefore, so will the spacial area of the beam required to impart a force onto the ions. It is, therefore, required to express this force as a function of α. The intensity of a beam required to provide a state dependant force, F, is given by [113]

$$I_0 = \frac{3F\Delta\lambda I_{sat}}{2\pi\hbar\gamma^2} \tag{8.28}$$

where Δ is the detuning of the laser from resonance, λ is the wavelength of the laser, I_{sat} is the saturation intensity of the ion and γ is 2π times the transition linewidth. The power of a laser beam is given by

$$P = I_0 a \tag{8.29}$$

where a is the spacial area to which the beam is focused. In this work the beam is assumed to be focused to form a light sheet across the array with an area given by $a = (n_s - 1)AW = (n_s - 1)k_A \alpha W$, where n_s is the number of trapping sites (or polygons) along one side of the array and W is the width of the light sheet. By using equations 8.28 and 8.29 the force applied to the ions by a laser power, P, can be expressed as

$$F = \frac{2\pi\hbar P\gamma^2}{3a\Delta\lambda I_{sat}}. \tag{8.30}$$

The form of E_0 for the case of lasers applying the state dependant force can now be found by using equations 8.18, 8.30 and the general error equation 8.27 yielding

$$E_{0laser} = \frac{4\sqrt{2}}{9}\frac{\pi^2\hbar}{e^3}\frac{Mk_r^6\gamma^4 m^2 P^2\alpha(\overline{n}+\frac{1}{2})}{\eta_{geo}^3(n_s-1)^2k_A^2W^2\Delta^2\lambda^2 I_{sat}^2}. \tag{8.31}$$

It follows that both the K_{sim} and simulation error E_0 will decrease with increasing laser detuning, Δ. Therefore, the optimum detuning, for a given laser power and α, corresponds to the lowest detuning which provides the required K_{sim}. The optimum detuning to achieve the lowest simulation error for $^{171}\mathrm{Yb}^+$ will be discussed in section 8.6.3.

Magnetic fields can also be used to provide the state dependant force, F, and is given by [91]

$$F_{\hat{i}} = \left(\frac{\hbar}{2}\right)\partial_i\omega\left\langle\sigma^{(\hat{i})}\right\rangle \tag{8.32}$$

where $\omega = \gamma_g bi$ is the position dependant spin resonance frequency with $\gamma_g = e/m_e$ the gyromagnetic ratio and i is the x, y or z direction. The magnetic field gradient b is assumed to arise from a magnetic field of the form $\overline{B} = \overline{B_0} + b\hat{i}$, where B_0 is a constant magnetic field offset. From this, the state dependant force, $F_{\hat{i}}$, produced from a magnetic field gradient, $b_{\hat{i}}$, is found to be

$$F_{\hat{i}} \approx \frac{\hbar e b_{\hat{i}}}{2m_e} \tag{8.33}$$

where m_e and e is the mass and charge of an electron respectively. If one assumes the magnetic field is created by a current carrying wire located on the surface of a polygon, at a distance a from the centre of the polygon and making an angle of 45° with respect to the x-axis then the magnetic field gradient will be of the form

$$b_{r'} = \frac{\mu_0 I}{2\pi r'^2}. \tag{8.34}$$

Here μ_0 is the permeability of free space, I is the current flowing through the wire and r'^2 is the distance squared of the ion from the current carrying wire and is equal to $r^2 + a^2$ where r is the ion height. It is assumed, for simplicity, that the distance a scales linearly with α with a constant of proportionality of k_a in order to keep the angle of r' to the x-z plane, θ, independent of α. As the ion height is known to scale linearly with α, from equation 8.15, it is possible to express the magnetic field gradient along r' as

$$b_{r'} = \frac{\mu_0 I}{2\pi\alpha^2 \left(k_r^2 + k_a^2\right)}. \tag{8.35}$$

The component of this magnetic field gradient in the x-z plane can now be shown to be

$$b_{x,z} = \frac{\mu_0 I \cos\theta}{4\pi\alpha^2 \left(k_r^2 + k_a^2\right)}. \tag{8.36}$$

The form of K_{sim} for the case of magnetic field gradients applying the state dependant force can be found by using equations 8.18, 8.33, 8.36 and the general error equation 8.27 yielding

$$E_{0mag} = \frac{\sqrt{2}}{64} \frac{\hbar\mu_0}{\pi^2 m_e^2 e} \frac{k_r^6 m^2 I^2 \cos^2\theta M \left(\overline{n} + \frac{1}{2}\right)}{\eta_{geo}^3 \left(k_r^2 + k_a^2\right)^2 \alpha}. \tag{8.37}$$

Equations 8.31 and 8.37 show that the quantum simulation error is proportional to α for a state dependant force created by a laser beam and proportional to α^{-1} for a magnetic field gradient created by current carrying wires. For the case of laser beams the α scaling implies that as α is increased (yielding larger K_{sim} values and geometries as shown in section 8.4.3) the quantum simulation error will rise and, therefore, provide an upper limit on the value of α. For the magnetic field gradient case the upper limit on α comes from the current creating the gradient. While the α scaling for the quantum simulation error using magnetic field gradients implies that a larger α is advantageous, the current required to achieve a given magnetic field gradient scales as α^2 as can be deduced from equation 8.35. The maximum current that one can apply to the lattice therefore provides an upper limit for α.

It is also interesting at this point to note the different scaling with α of the laser and magnetic field gradient forces given in equations 8.30 and 8.32. The laser force can be seen to be $\propto \alpha^{-1}$ as it is a function of the inverse of laser sheet cross section, a, which is $\propto \alpha^1$. The magnetic gradient force, on the other hand, is $\propto \alpha^{-2}$ as it is a function of the magnetic field gradient $b_{r'}$ which is $\propto \alpha^{-2}$ due to r' having a linear relationship with α in the geometry considered.

8.6.3 Spontaneous emission

When applying the state dependant force to the ions using a laser beam additional decoherence will occur via spontaneous emission. The spontaneous emission rate is given by [114, 115]

$$S = \frac{\gamma g^2}{6}\left(\frac{1}{\Delta^2} + \frac{2}{(\Delta_{fs} - \Delta)^2}\right) \tag{8.38}$$

where γ is 2π times the linewidth in Hz, Δ is the laser detuning from resonance, Δ_{fs} is the fine structure splitting of the ion (approximately 100 THz for $^{171}Yb^{+}$) and g is the single photon Rabi frequency given by

$$g = \gamma\sqrt{\frac{I_0}{2I_{sat}}}. \tag{8.39}$$

Here, I_0 is the laser intensity and I_{sat} is the saturation intensity of the ion. It is possible to express the single photon Rabi frequency in terms of the laser power, P, by using equation 8.29 giving

$$g = \gamma\sqrt{\frac{P}{2(n_s - 1)k_A\alpha W I_{sat}}}. \tag{8.40}$$

It is now possible to describe an additional parameter, L_{sim}, which describes the ratio of interaction rate to the spontaneous emission rate as

$$L_{sim} = \frac{T_S}{T_J} \tag{8.41}$$

where

$$T_S = \frac{1}{S}. \tag{8.42}$$

It has been shown that the detuning which minimises the effect of spontaneous emission is approximately 33 THz for $^{171}Yb^{+}$ [116]. It, therefore, follows that the value of L_{sim} will be maximised with this detuning. This additional parameter is analogous to the parameter K_{sim} in equation 8.3 and is also required to be greater than unity, just like the original K_{sim}, when considering a state dependent force created using laser light. If magnetic field gradients are to be used to apply the state dependent force then L_{sim} is no longer relevant.

8.6.4 Other considerations

It is important to note here that an increase in α will increase the time taken for ion-ion interactions to take place in optimised lattice structures, as will be shown in equation 8.44.

Equation 8.5 gives an expression for the time taken for an ion-ion interaction to occur in any given fixed lattice structure. This can be expressed for optimised lattice structures by including the expressions for the ion-ion separation (polygon separation, A) and secular frequency, ω, from equations 8.16 and 8.18 respectively, to yield

$$T_J = \frac{e^2\pi\epsilon_0\hbar}{2}\frac{\eta_{geo}^4 k_A^3}{k_r^8 F^2 m^2 \alpha}. \tag{8.43}$$

An expression to give the interaction time in optimised lattices as a function of α can now be arrived at by using equations 8.30 and 8.43,

$$T_J = \frac{9}{8}\frac{e^2\epsilon_0}{\pi\hbar}\frac{\eta_{geo}^4 k_A^3((n_s-1)k_A W)^2\Delta^2\lambda^2 I_{sat}^2\alpha}{k_r^8\gamma^4 P^2 m^2}. \tag{8.44}$$

Equation 8.44 clearly shows that as α is increased the time taken for an ion-ion interaction will increase and, so, it may be preferable to limit the magnitude of α after taking into account the effects on K_{sim}. A similar equation can also be derived for the use with magnetic field gradients. It is also important to note here that increasing the laser power, P, will increase the value of L_{sim} as the spontaneous emission rate is proportional to P whereas the coupling rate is proportional to P^2 as shown in equations 8.38 and 8.44 respectively.

With the use of the equations derived in this section, optimal geometries can be calculated given certain experimental parameters and will be described in the following section.

8.7 Example case study

In this section, an example case will be presented to show how a 2D lattice for the use in quantum simulations can be designed using the work in this paper, whose successful operation is within reach of current technology when using lasers. It will then go on to show that while magnetic field gradients can be used to create a state dependant force their use may be more challenging.

From equation 8.23 we can see that there is a unique voltage for a given mass, m, lattice type and stability parameter, q. For this example case we choose a lattice comprised of square type unit cells with 9 trapping sites for $^{171}\mathrm{Yb}^+$ ions with a stability parameter $q = 0.5$. Using these parameters the voltage can now be determined by calculating k_r. k_r can be found by plotting the ion height of an optimised lattice against α, as shown in figure 8.8 (a), and finding the gradient of this linear relationship. For this example case $k_r = 98(5)\ \mathrm{mV}^{-1}\mathrm{s}^{-1}$. Using this result and equation 8.23 the unique voltage is found to

be 33(2) V where η_{geo} has been calculated to be 0.14(1).

The α dependant polygon radius and separation can be calculated by producing the corresponding graphs in figure 8.10, using the method described in section 8.4.3, for the lattice type and ion to be used. For this example case the optimum radius and separation of the polygons in terms of α is 45(1)α μm and 174(1)α μm respectively.

The next step is to choose a laser detuning from resonance and a maximum acceptable error, E_0, to be used. For $^{171}Yb^+$, as explained in section 8.6.3, the optimum detuning is approximately 33 THz giving a wavelength of 355 nm which is therefore used in this example case together with a maximum acceptable error of 0.25. Note that in this example case the array is assumed to be at cryogenic temperatures which correspond to an electric field noise density three orders of magnitude less than at room temperature. It can see from equation 8.31 that α needs to be minimised in order to keep the quantum simulation error low. The minimum α is determined by the lowest ion height one can easily achieve which for this example case is chosen to be equal to 30 μm. For this case α is found to be 0.30(2) $VMHz^{-1}$. Having determined α the optimum radius and separation are found to be equal to 14(1) μm and 52(3) μm respectively. To calculate the laser power required equation 8.31 should be set to the maximum acceptable error and solved for the laser power, which is found to be 7(1) W assuming the ions to be cooled to $\overline{n} \ll 1$ and M = 1 (one site average observable). These conditions provide a coupling rate, J, of 530$\pm$110 Hz with a $\beta = (2.8\pm0.2)\times10^{-5}$. This laser power can, for example, be achieved using a commercially available diode pumped solid state (Coherent Paladin range) or fibre (Coherent Talisker range) laser system. Table 8.9 summarises all parameters for this example case study.

Figure 8.14 shows the effect a change of α and laser power, P, has on the quantum simulation error (solid curves), K_{sim} (dashed curves) and L_{sim} (dotted lines). The cross corresponds to the 2D lattice designed in this example case which represents the optimum case in terms of achieving the highest K_{sim} and L_{sim} for a maximum quantum simulation error of 0.25. It should be noted at this point that the main limitations in achieving lower quantum simulation errors stem from the lowest achievable ion height (lowest α) and magnitude of electric field noise density. Figure 8.14 also shows that higher values of K_{sim} and L_{sim} can be achieved with any given geometry (given by the value of α) by simply increasing the power of the laser. However, this can only be achieved at the expense of higher quantum simulation errors.

State dependant forces can also be created using magnetic field gradients as described in section 8.6.2. Figure 8.15 shows the K_{sim} (solid curves) and the quantum simulation

α	R [μm]	A [μm]	Δ [THz]	P [W]	M	K_{sim}	L_{sim}	E_0
0.30(2)	14(1)	52(3)	33	7(1)	1	35	1.5	0.25

Table 8.9: Table summarising the parameters for a 3 by 3 square type unit cell lattice at cryogenic temperature as shown in the example case study

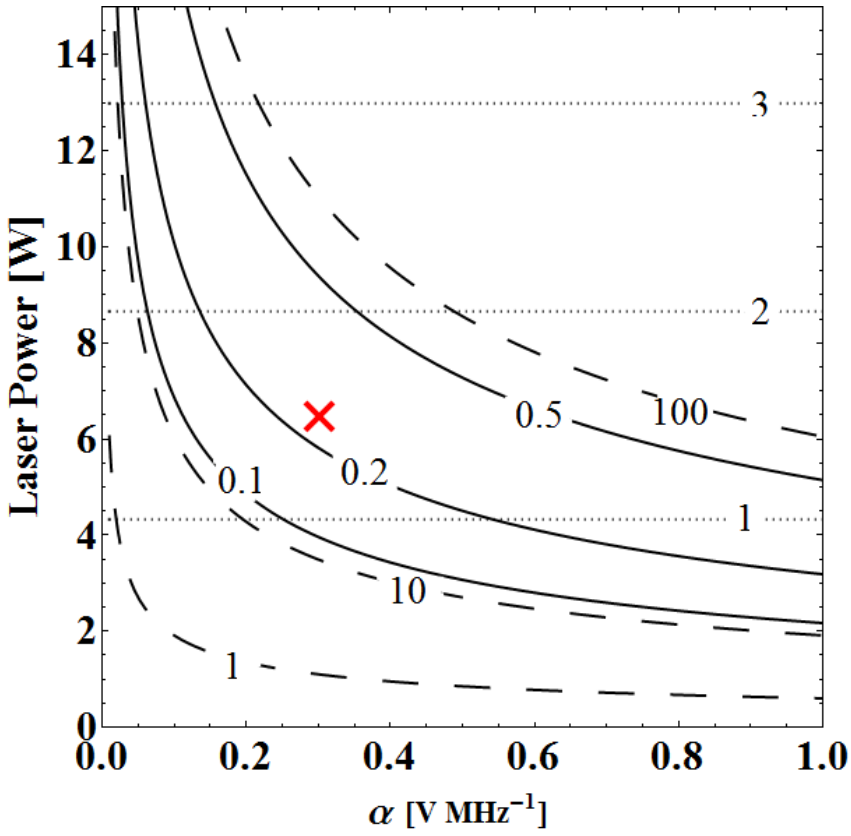

Figure 8.14: Graph showing the quantum simulation error (solid curves), K_{sim} (dashed curves) and L_{sim} (dotted lines) for a three by three square type unit cell lattice with $^{171}Yb^{+}$ ions as a function of α and laser power. Here traps are operated at cryogenic temperature. The cross indicates the example case.

error (dashed curves) as a function of the magnetic field gradient, b, and α for traps operated at cryogenic temperature. Here $^{171}Yb^{+}$ ions are used in a three by three square unit cell array. As described in section 8.6.2, $E_0 \propto \alpha^{-1}$ indicating that a large α is advantageous. The limit on the maximum α is dependant on the maximum current one can apply to the geometry. Using equation 8.35 it is possible to calculate the current required to create a desired magnetic field gradient. In order to illustrate the magnitude of currents required we assume $k_a = k_r$, which will result in an angle $\theta = 45°$ (refer to section 8.6.2 for more information). The value of α is set to 0.30(2) VMHz^{-1}, determined by the lowest achievable ion height which, for illustration purposes, we have set to 30 μm. The reason for choosing the minimum α value can be seen when considering equation 8.35 which clearly shows that, for a given magnetic field gradient, $I \propto \alpha^2$. In the magnetic field gradient case, the chosen α sets K_{sim} and E_0. For this case, again, the value of M is chosen to be one, $\overline{n} \ll 1$, $K_{sim} = 2$ and $E_0 = 0.01$ which requires a magnetic field gradient of 30,500±3500 Tm^{-1} and is indicated by the cross on figure 8.15. This is achievable with a current of approximately 1,200 A yielding a coupling rate, J, of 240 Hz and a $\beta = (2.8 \pm 0.2) \times 10^{-8}$. From this simple example case one can conclude that using magnetic field gradients to provide state dependant forces for the use in quantum simulations using the methods and trap designs shown in this work is quite challenging. However, geometries trapping ions in chains allow for sizeable magnetic gradient induced couplings [117] and, so, a detailed investigation into optimising the wires used for producing magnetic field gradients in the geometries discussed in this work could improve results.

8.8 Conclusion

Two-dimensional arrays of surface ion traps have the potential to provide a technology with which quantum simulations can be performed. In order for ion traps to be used successfully for this purpose a greater understanding is required of how the various geometry parameters affect the ions trapped above them. Throughout this work square, hexagonal and centre rectangular unit cell arrays of microtraps have been modelled in the gap-less plane approximation using the Biot-Savart like law in electrostatics [2]. Decoherence due to motional heating [66] was then compared to the ion-ion interaction [59] to provide a ratio used to describe how much faster an ion-ion interaction occurs in comparison to the motional decoherence, K_{sim}. This work investigates how various parameters in the array can be adjusted in order to optimise the device's ability to perform quantum simulations and shows how the interactions can be made as homogeneous as possible over the device.

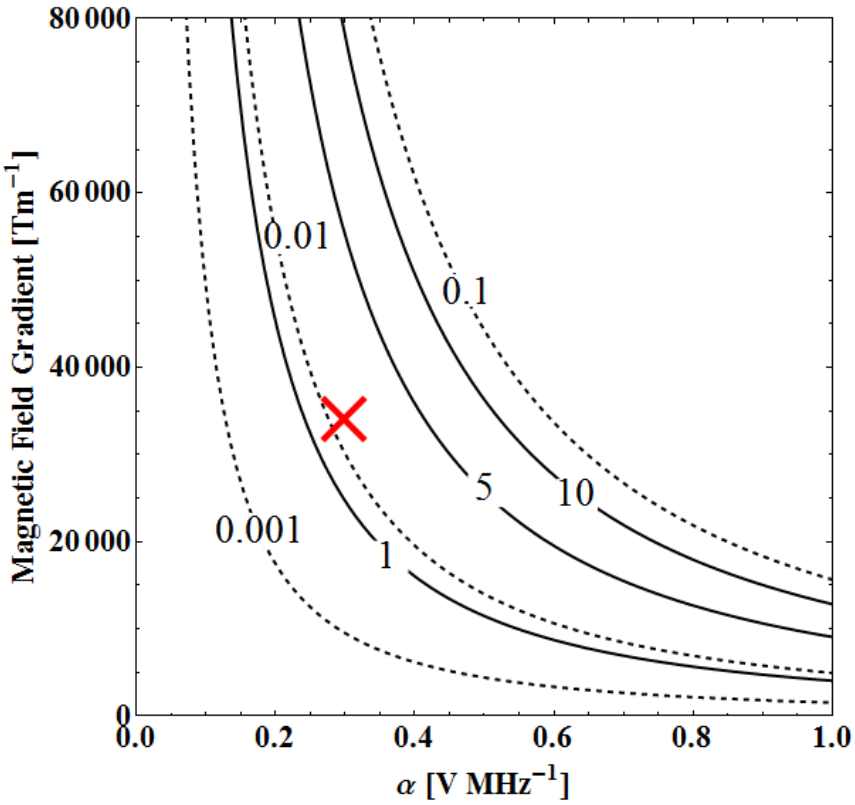

Figure 8.15: Graph showing the quantum simulation error (dashed curves) and the K_{sim} (solid curves) of a three by three square type unit cell lattice with $^{171}Yb^{+}$ ions as a function of α and magnetic field gradient. Here traps are operated at cryogenic temperatures.

It has been shown how the homogeneity of the K_{sim} across an array can be altered by varying the distance from the outer polygon to the edge of the rf electrode. The distance required to maximise the K_{sim} homogeneity is also shown to vary as a function of the total size of the lattice. The number of polygon sides, n, required to maximise K_{sim} has also been found.

It has been shown that the K_{sim} of a given lattice geometry can be maximised by reducing the value of α. However, as α reduces so does the trap depth. This results in the conclusion that the maximum K_{sim} of a geometry can be achieved by reducing the value of α until the trap depth reaches a reasonable minimum value.

Using this information, optimal geometries as a function of α are presented. This has been achieved by finding the relationships of polygon separation and radius with α for optimal geometries. It was found that, for these optimal geometries, K_{sim} scales as α^3. The individual polygon separation and radius were found to possess a linear relationship with α and, therefore, larger geometries have been found to produce larger values of K_{sim}. Therefore, the optimal lattice geometry is dependent solely on the value of α for a given ion mass and number of trapping sites in the array.

A case study for determining an optimum geometry consisting of 9 trapping sites arranged into square type unit cells for $^{171}Yb^{+}$ ions has been presented. It has been shown how the value of α can be chosen (and, therefore, the geometry dimensions) by taking into account the laser power (or static magnetic field gradient) required to produce a state dependant force acting on the ions, the K_{sim} and the error on the simulation. From this it has been found that to carry out quantum simulations with reasonable K_{sim} and error values it is preferable to use traps held at cryogenic temperatures as this reduces decoherence due to heating effects on the ions. Other methods known to significantly decrease the anomalous heating rate include pulsed laser electrode cleaning [118] and Argon-ion beam electrode cleaning [119].

The scaling of anomalous heating has not yet been fully understood and is thought to possess a dependence with the ion height, r, of between r^{-4} and r^{-2}. In this work we have used r^{-4} however, if the anomalous heating is found to possess a relationship with ion height nearer r^{-2} then the equations in this work can be adjusted and this is discussed in more detail in Appendix B.

The relationships between lattice size and α with the polygon radii and separation obtained using the method described in this work will allow for the construction of two-dimensional surface trap lattice arrays with high ratios of ion-ion interaction rates to

decoherence rates, providing a system which could be used to perform quantum simulations.

Chapter 9

Conclusion

In this thesis the design, set-up and implementation of an Yb^+ ion trapping experiment, capable of housing both symmetric and asymmetric ion traps with up to 90 electrical connects, has been described. This includes details on the vacuum system used to house the macroscopic ion trap presented along with descriptions of the lasers and associated electronics required to provide frequency stable light sources. The optics and detectors used to image trapped ions is presented along with signal to noise calculations that show under what conditions a PMT or EMCCD is the preferred photon detection device. An experimental set-up of this type allows for the implementation and testing of a wide range of ion traps with short turnaround times as the vacuum system housing the trap does not need to be redesigned for each trap used.

A detailed study is presented on the application of high voltages at radio frequencies to ion traps using helical resonators. This has been carried out by modelling a helical resonator connected to an ion trap load as a lumped element circuit allowing expressions for the quality factor of resonance and the resonant frequency to be deduced. A design guide for helical resonators attached to ion trap loads has been presented. This study and design guide enables a resonator to be constructed which will optimise the device's quality factor and increase the radio frequency noise filtering of a given experiment resulting in less noise injected into the system. This reduction in noise could lead to increased ion lifetimes and secular frequencies and more efficient cooling of trapped ions.

The successful trapping of the 170, 171, 172, 174 and 176 Yb^+ isotopes has been presented. It was noted during this initial trapping procedure that Yb^+ ion transition frequencies were not available to the required accuracy for successful trapping. For this reason the transition frequencies for each isotope trapped have been measured to an accuracy of 120 MHz. By measuring these transition frequencies the initial trapping procedure

for future Yb^+ ion trap experiments will be made much simpler. Additionally, heating rate measurements of $^{174}Yb^+$ ions confined in a linear macroscopic Paul trap are presented and shown not to be unusually high. This shows that the Yb^+ ion is not subject to abnormally high heating rates as feared due to coating of electrodes and cements its place as a leading candidate for performing quantum information processing with trapped ions.

Two-dimensional arrays of trapped ions provide a system with which quantum simulations can be carried out. Quantum simulators provide an attainable stepping stone between current classical computing and fully fledged quantum computing. However, in order to develop technology capable of this goal a greater understanding of the geometries required to trap two-dimensional arrays of ions is required. In this work it is shown how arrays of static voltage islands in a radio frequency surface electrode can be used to trap two-dimensional arrays of ions. It is shown how varying the space at the edge of this surface array can affect the homogeneity of the individual trapping sites above these islands. The number of sides in the polygons which make up the islands has been investigated and it has been shown that polygons with over 25 sides produce a K_{sim} within 95% of that of a circular shaped island. Below this value the value of K_{sim} is shown to drop markedly. Providing trapping fields which allow decoherence times to be greater than interaction times (with a $K_{sim} > 1$) is important, if this is not the case then any simulations carried out will be subject to low fidelities. With the aim of maximising the ratio between decoherence times and interaction times a method has been presented which shows how the radii and centre-centre separation of polygons in surface geometries can be optimised. It is then shown that the optimal surface geometry is dependant on the value of α (the ratio of rf voltage to drive frequency) for a given ion mass and number of trapping sites.

It has been shown how the value of α can be chosen (and, therefore, the optimum geometry dimensions) by taking into account the laser power (or static magnetic field gradient) required to produce a state dependant force acting on the ions, the K_{sim} and the error on the simulation. From this it has been found that to carry out quantum simulations with reasonable K_{sim} and error values it is preferable to use traps held at cryogenic temperatures as this reduces decoherence due to heating effects on the ions. A case study is presented which describes the optimisation process for a geometry with 9 trapping sites and $^{171}Yb^+$ ions. By showing how the homogeneity and ratio of decoherence time to interaction time can be maximised in two-dimensional surface trap arrays a geometry optimised for the purpose of performing quantum simulations can be conceived bringing the technology of quantum simulators within our reach.

Bibliography

[1] M. G. House. Analytic model for electrostatic fields in surface-electrode ion traps. *Phys. Rev. A*, 78:033402, Sep 2008. Cited on xix, 122, 123, 128, 132

[2] Mário H. Oliveira and José A. Miranda. Biot-Savart-like law in electrostatics. *European Journal of Physics*, 22(1):31, 2001. Cited on xix, 122, 123, 146

[3] Marcus D. Hughes, Bjoern Lekitsch, Jiddu A. Broersma, and Winfried K. Hensinger. Microfabricated ion traps. *Contemporary Physics*, 52:505–529, 2011. Cited on xxix, 2, 113, 115, 117, 120, 121, 122, 137

[4] Alan M. Turing. On computable numbers, with an application to the Entscheidungsproblem. *Proceedings of the London Mathematical Society*, 42:230–265, 1936. Cited on 1

[5] Richard Feynman and Peter W. Shor. Simulating physics with computers. *SIAM Journal on Computing*, 26:1484–1509, 1982. Cited on 1

[6] David Deutsch. Quantum theory, the Church-Turing principle and the universal quantum computer. *Proc. R. Soc. A*, 400(1818):97–117, 1985. Cited on 1

[7] D. Deutsch and R. Jozsa. Rapid solution of problems by quantum computation. *Proc. R. Soc. A*, 439:553–558, October 1992. Cited on 1

[8] Peter W. Shor. Algorithms for quantum computation: Discrete logarithms and factoring. *Proceedings of the 35th Annual Symposium on the Foundations of Computer Science*, pages 124–134, 1994. Cited on 1

[9] Peter W. Shor. Polynomial-time algorithms for prime factorization and discrete logarithms on a quantum computer. *SIAM Journal on Computing.*, 26:1484–1509, October 1997. Cited on 1

[10] Lov K. Grover. Quantum mechanics helps in searching for a needle in a haystack. *Phys. Rev. Lett.*, 79(2):325–328, July 1997. Cited on 1

[11] C. H. Bennett and G. Brassard. Quantum cryptography: Public key distribution and coin tossing. *Proceedings of the IEEE International Conference on Computers Systems and Signal Processing*, pages 175–179, December 1984. Cited on 1

[12] Artur K. Ekert. Quantum cryptography based on Bell's theorem. *Phys. Rev. Lett.*, 67(6):661–663, Aug 1991. Cited on 1

[13] W.K. Wootters and W.H. Zurek. A single quantum cannot be cloned. *Nature*, 299:802–803, October 1982. Cited on 1

[14] J. I. Cirac and P. Zoller. Quantum computations with cold trapped ions. *Phys. Rev. Lett.*, 74(20):4091–4094, May 1995. Cited on 2, 49

[15] Klaus Mølmer and Anders Sørensen. Multiparticle entanglement of hot trapped ions. *Phys. Rev. Lett.*, 82(9):1835–1838, Mar 1999. Cited on 2

[16] C. Monroe, D. M. Meekhof, B. E. King, W. M. Itano, and D. J. Wineland. Demonstration of a fundamental quantum logic gate. *Phys. Rev. Lett.*, 75(25):4714–4717, Dec 1995. Cited on 2

[17] D. Leibfried, B. DeMarco, V. Meyer, D. Lucas, M. Barrett, J. Britton, W. M. Itano, B. Jelenković, C. Langer, T. Rosenband, and D. J. Wineland. Experimental demonstration of a robust, high-fidelity geometric two ion-qubit phase gate. *Nature*, 422:412–415, 2003. Cited on 2, 13

[18] H.C. Nägerl, W. Bechter, J. Eschner, F. Schmidt-Kaler, and R. Blatt. Ion strings for quantum gates. *Applied Physics B: Lasers and Optics*, 66:603–608, May 1998. Cited on 2

[19] Ferdinand Schmidt-Kaler, Hartmut Häffner, Mark Riebe, Stephan Gulde, Gavin P. T. Lancaster, Thomas Deuschle, Christoph Becher, Christian F. Roos, Jürgen Eschner, and Rainer Blatt. Realisation of the Cirac-Zoller controlled-NOT quantum gate. *Nature*, 422:408–411, March 2003. Cited on 2, 13

[20] C. A. Sackett, D. Kieplinski, B. E. King, C. Langer, V. Meyer, C. J. Myatt, M. Rowe, Q. A. Turchette, W. M. Itano, D. J. Wineland, and C. Monroe. Experimental entanglement of four particles. *Nature*, 404:256–259, March 2000. Cited on 2

[21] M. D. Barrett, J. Chiaverini, T. Schaetz, J. Britton, W. M. Itano, J. D. Jost, E. Knill, C. Langer, D. Leibfried, R. Ozeri, and D. J. Wineland. Deterministic quantum teleportation of atomic qubits. *Nature*, 429:737–739, June 2004. Cited on 2

[22] H. Häffner, F. Schmidt-Kaler, W. Hänsel, C. F. Roos, T. Körber, M. Chwalla, M. Riebe, J. Benhelm, U. D. Rapol, C. Becher, and R. Blatt. Robust entanglement. *Appl. Phys. B*, 81:151–153, July 2005. Cited on 2, 119

[23] M. Riebe, H. Häffner, C. F. Roos, W. Hänsel, J. Benhelm, G. P. T. Lancaster, T. W. Körber, C. Becher, F. Schmidt-Kaler, D. F. V. James, and R. Blatt. Deterministic quantum teleportation with atoms. *Nature*, 429:734–737, June 2004. Cited on 2

[24] K.-A. Brickman, P. C. Haljan, P. J. Lee, M. Acton, L. Deslauriers, and C. Monroe. Implementation of Grover's quantum search algorithm in a scalable system. *Phys. Rev. A*, 72(5):050306, Nov 2005. Cited on 2

[25] H. Häffner, W. Hänsel, C. F. Roos, J. Benhelm, D. Chek al kar, M. Chwalla, T. Körber, U. D. Rapol, M. Riebe, P. O. Schmidt, C. Becher, O. Gühne, W. Dür, and R. Blatt. Scalable multiparticle entanglement of trapped ions. *Nature*, 438, 2005. Cited on 2

[26] H. Häffner, C.F. Roos, and R. Blatt. Quantum computing with trapped ions. *Physics Reports*, 469:155 – 203, 2008. Cited on 2, 49

[27] D. Leibfried, E. Knill, S. Seidelin, J. Britton, R. B. Blakestad, J. Chiaverini, D. B. Hume, W. M. Itano, J. D. Jost, C. Langer, R. Ozeri, R. Reichle, and D. J. Wineland. Creation of a six-atom 'Schrödinger cat' state. *Nature*, 438(7068):639–642, 2005. Cited on 2

[28] N. Timoney, I. Baumgart, M. Johanning, A. F. Varón, M. B. Plenio, A. Retzker, and Ch. Wunderlich. Quantum gates and memory using microwave-dressed states. *Nature*, 476:185 – 188, August 2011. Cited on 2

[29] C. Ospelkaus, U. Warring, Y. Colombe, K. R. Brown, J. M. Amini, D. Leibfried, and D. J. Wineland. Microwave quantum logic gates for trapped ions. *Nature*, 476:181 – 184, August 2011. Cited on 2, 117

[30] G.-D. Lin, S.-L. Zhu, R. Islam, K. Kim, M.-S. Chang, S. Korenblit, C. Monroe, and L.-M. Duan. Large-scale quantum computation in an anharmonic linear ion trap. *Europhys. Lett.*, 86(6):60004, 2009. Cited on 2

[31] S. Seidelin, J. Chiaverini, R. Reichle, J. J. Bollinger, D. Leibfried, J. Britton, J. H. Wesenberg, R. B. Blakestad, R. J. Epstein, D. B. Hume, W. M. Itano, J. D.

Jost, C. Langer, R. Ozeri, N. Shiga, and D. J. Wineland. Microfabricated surface-electrode ion trap for scalable quantum information processing. *Phys. Rev. Lett.*, 96(25):253003, June 2006. Cited on 2, 115

[32] D. Stick, W. K. Hensinger, S. Olmschenk, M. J. Madsen, K. Schwab, and C. Monroe. Ion trap in a semiconductor chip. *Nature Physics*, 2:36–39, 2006. Cited on 2, 115

[33] E. W. Streed, T. J. Weinhold, and D. Kielpinski. Frequency stabilization of an ultraviolet laser to ions in a discharge. *Applied Physics Letters*, 93:071103, 2008. Cited on 3, 107

[34] J. H. Wesenberg, R. J. Epstein, D. Leibfried, R. B. Blakestad, J. Britton, J. P. Home, W. M. Itano, J. D. Jost, E. Knill, C. Langer, R. Ozeri, S. Seidelin, and D. J. Wineland. Fluorescence during Doppler cooling of a single trapped atom. *Phys. Rev. A*, 76(5):053416, Nov 2007. Cited on 3, 109, 110, 112

[35] Chr. Balzer, A. Braun, T. Hannemann, Chr. Paape, M. Ettler, W. Neuhauser, and Chr. Wunderlich. Electrodynamically trapped Yb^+ ions for quantum information processing. *Phys. Rev. A*, 73(4):041407, April 2006. Cited on 5, 6

[36] Altaf H. Nizamani, James J. McLoughlin, and Winfried K. Hensinger. Doppler-free Yb spectroscopy with the fluorescence spot technique. *Phys. Rev. A*, 82(4):043408, Oct 2010. Cited on 6, 19, 107, 109

[37] S. Earnshaw. On the nature of the molecular forces which regulate the constitution of the luminiferous ether. *Trans. Camb. Phil. Soc.*, 7:97–112, 1839. Cited on 6

[38] Walfgang Paul. Electromagnetic traps for charged and neutral particles. *Rev. Mod. Phys.*, 62:531–540, July 1990. Cited on 6, 7, 49

[39] M.J. Madsen, W.K. Hensinger, D. Stick, J.A. Rabchuk, and C. Monroe. Planar ion trap geometery for microfabrication. *Applied Physics B*, 78:639–651, 2004. Cited on 6, 7, 120, 121, 137

[40] H.G. Dehmelt. Radiofrequency spectroscopy of stored ions I: Storage. volume 3 of *Advances in Atomic and Molecular Physics*, pages 53 – 72. Academic Press, 1968. Cited on 7

[41] S. Olmschenk, K. C. Younge, D. L. Moehring, D. N. Matsukevich, P. Maunz, and C. Monroe. Manipulation and detection of a trapped Yb^+ hyperfine qubit. *Phys. Rev. A*, 76(5):052314, Nov 2007. Cited on 10

[42] D. Engelke and Chr. Tamm. Dark times in the resonance fluorescence of trapped ^{171}Yb ions caused by spontaneous quantum jumps to the $^2D_{3/2}(F = 2)$ state. *Europhys. Lett.*, 33(5):347, 1996. Cited on 10

[43] K. Hosaka, S.A. Webster, P.J. Blythe, A. Stannard, D. Beaton, H.S. Margolis, S.N. Lea, and P. Gill. An optical frequency standard based on the electric octupole transition in $^{171}Yb^+$. *Instrumentation and Measurement, IEEE Transactions on*, 54:759 – 762, April 2005. Cited on 12

[44] M. Roberts, P. Taylor, S. V. Gateva-Kostova, R. B. M. Clarke, W. R. C. Rowley, and P. Gill. Measurement of the $^2S_{1/2} -^2 D_{5/2}$ clock transition in a single $^{171}Yb^+$ ion. *Phys. Rev. A*, 60:2867–2872, Oct 1999. Cited on 13, 108

[45] N. Timoney, V. Elman, S. Glaser, C. Weiss, M. Johanning, W. Neuhauser, and Chr. Wunderlich. Error-resistant single-qubit gates with trapped ions. *Phys. Rev. A*, 77(5):052334, May 2008. Cited on 13

[46] J. P. Home, M. J. McDonnell, D. M. Lucas, G. Imreh, B. C. Keitch, D. J. Szwer, N. R. Thomas, S. C. Webster, D. N. Stacey, and A. M. Steane. Deterministic entanglement and tomography of ion-spin qubits. *New Journal of Physics*, 8(9):188, 2006. Cited on 13

[47] J. Chiaverini, D. Leibfried, T. Schaetz, M. D. Barrett, R. B. Blackestad, J. Britton, W. M. Itano, J. D. Jost, E. Knill, C. Langer, R. Ozeri, and D. J. Wineland. Realisation of quantum error correction. *Nature*, 432:602–605, 2004. Cited on 13

[48] D. J. Wineland, R. E. Drullinger, and F. L. Walls. Radiation-pressure cooling of bound resonant absorbers. *Phys. Rev. Lett.*, 40:1639–1642, Jun 1978. Cited on 13

[49] Wayne M. Itano and D. J. Wineland. Laser cooling of ions stored in harmonic and Penning traps. *Phys. Rev. A*, 25:35–54, Jan 1982. Cited on 13

[50] Harold J. Metcalf and Peter van der Straten. *Laser Cooling and Trapping*. Springer-Verlag New York, Inc., 1999. Cited on 13, 15, 102

[51] D. Hucul, M. Yeo, C. Olmschenk, C. Monroe, W. K. Hensinger, and J. Rabchuk. On the transport of atomic ions in linear and multidimensional ion trap arrays. *Quantum Info. Comput.*, 8(6):501–578, July 2008. Cited on 26

[52] A. S. Arnold, J. S. Wilson, and M. G. Boshier. A simple extended-cavity diode laser. *Rev. Sci. Instrum.*, 69:1236–1239, 1998. Cited on 30

[53] W. Z. Zhao, J. E. Simsarian, L. A. Orozco, and G. D. Sprouse. A computer-based digital feedback control of frequency drift of multiple lasers. *Rev. Sci. Instrum.*, 69:3737–3740, 1998. Cited on 33, 36

[54] Nicolas Seymour-Smith, Peter Blythe, Matthias Keller, and Wolfgang Lange. Fast scanning cavity offset lock for laser frequency drift stabilization. *Rev. Sci. Instrum.*, 81:075109, 2010. Cited on 33

[55] J. J. Bollinger, D. J. Heinzen, W. M. Itano, S. L. Gilbert, and D. J. Wineland. A 303 MHz frequency standard based on trapped Be^+ ions. *Conference on Precision Electromagnetic Measurements, 1990. CPEM '90 Digest*, 40, 1991. Cited on 49

[56] P.H. Fisk, M.J. Sellars, M.A. Lawn, and C. Coles. Accurate measurement of the 12.6 GHz 'clock' transition in trapped $^{171}Yb^+$ ions. *IEEE Trans. Ultrasonics, Ferroelectrics, and Frequency*, 44:344–254, 1997. Cited on 49

[57] D. Kielpinski, C.R. Monroe, and D.J. Wineland. Architecture for a large-scale ion-trap quantum computer. *Nature*, 417:709–711, June 2002. Cited on 49, 117

[58] P. A. Ivanov, S. S. Ivanov, N. V. Vitanov, A. Mering, M. Fleischhauer, and K. Singer. Simulation of a quantum phase transition of polaritons with trapped ions. *Phys. Rev. A*, 80:060301, Dec 2009. Cited on 49

[59] D. Porras and J. I. Cirac. Effective quantum spin systems with trapped ions. *Phys. Rev. Lett.*, 92:207901, May 2004. Cited on 49, 119, 146

[60] H. Schmitz, A. Friedenauer, C. Schneider, R. Matjeschk, M Enderlein, T. Huber, J. Glueckert, D. Porras, and T. Schaetz. The "arch" of simulating quantum spin systems with trapped ions. *Applied Physics B*, 95:195–203, March 2009. Cited on 49

[61] Robert J. Clark, Tongyan Lin, Kenneth R. Brown, and Isaac L. Chuang. A two-dimensional lattice ion trap for quantum simulation. *Journal of Applied Physics*, 105:013114, 2009. Cited on 49, 117, 121, 137

[62] Ming Yu and Van Dokas. High performance helical resonator filters. *34th European Microwave Conference, 2004*, 2:989–982, October 2004. Cited on 49

[63] J.C. Collingwood and J.W. White. Helical resonators for spin resonance spectroscopy. *J. Sci. Instrum.*, 44:509–513, 1967. Cited on 49

[64] W. Meyer. Helical resonators for measuring dialectric properties of materials. *IEEE Transactions on Microwave Theory and Techniques*, 29(3):240–247, March 1981. Cited on 49

[65] W.W. Macalpine and R.O. Schildknecht. Coaxial resonators with helical inner conductor. *Proceedings of the IRE*, 47:2099–2105, December 1959. Cited on 49, 50, 61, 63

[66] Q. A. Turchette, Kielpinski, B. E. King, D. Leibfried, D. M. Meekhof, C. J. Myatt, M. A. Rowe, C. A. Sackett, C. S. Wood, W. M. Itano, C. Monroe, and D. J. Wineland. Heating of trapped ions from the quantum ground state. *Phys. Rev. A*, 61:063418, May 2000. Cited on 51, 52, 109, 112, 115, 118, 120, 132, 146

[67] R.G.Medhurst. H.F. resistance and self-capacitance of single-layer solenoids. *Wireless Engineer*, pages 35–43, 80–92, February and March 1947. Cited on 61

[68] A.I. Zverev and H.J. Blinchikoff. Realization of a filter with helical components. *IRE Transactions on Component Parts*, 8:99–110, 1961. Cited on 65

[69] Martin John Madsen. *Advanced Ion Trap Development and Ultrafast Laser-Ion Interactions*. PhD thesis, The University of Michigan, 2006. Cited on 81

[70] Daniel Lynn Stick. *Fabrication and Characterization of Semiconductor Ion Traps for Quantum Information Processing*. PhD thesis, The University of Michigan, 2007. Cited on 81

[71] Steven Matthew Olmschenk. *Quantum Teleportation between Distant Matter Qubits*. PhD thesis, The University of Michigan, 2009. Cited on 81

[72] Andor Technology. *Scientific Digital Camera Solutions*. 2006. Cited on 97

[73] L. Deslauriers, S. Olmschenk, D. Stick, W. K. Hensinger, J. Sterk, and C. Monroe. Scaling and suppression of anomalous heating in ion traps. *Phys. Rev. Lett.*, 97:103007, Sep 2006. Cited on 109, 112, 115

[74] F. Diedrich, J. C. Bergquist, Wayne M. Itano, and D. J. Wineland. Laser cooling to the zero-point energy of motion. *Phys. Rev. Lett.*, 62:403–406, Jan 1989. Cited on 115

[75] Ralph G. DeVoe and Christian Kurtsiefer. Experimental study of anomalous heating and trap instabilities in a microscopic ^{137}Ba ion trap. *Phys. Rev. A*, 65:063407, Jun 2002. Cited on 115

[76] Ch. Roos, Th. Zeiger, H. Rohde, H. C. Nägerl, J. Eschner, D. Leibfried, F. Schmidt-Kaler, and R. Blatt. Quantum state engineering on an optical transition and decoherence in a Paul trap. *Phys. Rev. Lett.*, 83:4713–4716, Dec 1999. Cited on 115

[77] Stephan A. Schulz, Ulrich Poschinger, Frank Ziesel, and Ferdinand Schmidt-Kaler. Sideband cooling and coherent dynamics in a microchip multi-segmented ion trap. *New Journal of Physics*, 10:045007, April 2008. Cited on 115

[78] D. T. C. Allcock, J. A. Sherman, D. N. Stacey, A. H. Burrell, M. J. Curtis, G. Imreh, N. M. Linke, D. J. Szwer, S. C. Webster, A. M. Steane, and D. M. Lucas. Implementation of a symmetric surface-electrode ion trap with field compensation using a modulated Raman effect. *New J. Phys.*, 12:053026, May 2010. Cited on 115

[79] N. Daniilidis, S. Narayanan, S. A. Möller, R. Clark, T. E. Lee, P. J. Leek, A. Wallraff, St. Schulz, F. Schmidt-Kaler, and H. Häffner. Fabrication and heating rate study of microscopic surface electrode ion traps. *New J. Phys.*, 13:013032, January 2011. Cited on 115

[80] Chr. Tamm, D. Engelke, and V. Bühner. Spectroscopy of the electric-quadrupole transition ${}^2S_{1/2}(F=0) - {}^2D_{3/2}(F=2)$ in trapped ${}^{171}\mathrm{Yb}^+$. *Phys. Rev. A*, 61:053405, Apr 2000. Cited on 115

[81] James J. McLoughlin, Altaf H. Nizamani, James D. Siverns, Robin C. Sterling, Marcus D. Hughes, Bjoern Lekitsch, Björn Stein, Seb Weidt, and Winfried K. Hensinger. Versatile ytterbium ion trap experiment for operation of scalable ion-trap chips with motional heating and transition-frequency measurements. *Phys. Rev. A*, 83:013406, Jan 2011. Cited on 115

[82] M. A. Rowe, A. Ben-Kish, B. DeMarco, D. Leibfried, V. Meyer, J. Beall, Joe Britton, J. Hughes, W. M. Itano, B. Jelenković, C. Langer, T. Rosenband, and D. J. Wineland. Transport of quantum states and separation of ions in a dual RF ion trap. *Quantum Information and Computation*, 2:257–271, 2002. Cited on 115

[83] J. Britton. *Microfabrication techniques for trapped ion quantum information processing.* PhD thesis, arxiv:1008.2222v1, Univeristy of Colorado, 2008. Cited on 115

[84] R. J. Epstein, S. Seidelin, D. Leibfried, J. H. Wesenberg, J. J. Bollinger, J. M. Amini, R. B. Blakestad, J. Britton, J. P. Home, W. M. Itano, J. D. Jost, E. Knill,

C. Langer, R. Ozeri, N. Shiga, and D. J. Wineland. Simplified motional heating rate measurements of trapped ions. *Phys. Rev. A*, 76:033411, Sep 2007. Cited on 115

[85] J. M. Amini, H. Uys, J. H. Wesenberg, S. Seidelin, J. Britton, J. J. Bollinger, D. Leibfried, C. Ospelkaus, A. P. VanDevender, and D. J. Wineland. Toward scalable ion traps for quantum information processing. *New Journal of Physics*, 12(3):033031, 2010. Cited on 115, 122

[86] J. Britton, D. Leibfried, J. A. Beall, R. B. Blakestad, J. H. Wesenberg, and D. J. Wineland. Scalable arrays of rf Paul traps in degenerate Si. *Appl. Phys. Lett.*, 95:173102, Oct 2009. Cited on 115

[87] Shannon X. Wang, Yufei Ge, Jaroslaw Labaziewicz, Eric Dauler, Karl Berggren, and Isaac L. Chuang. Superconducting microfabricated ion traps. *Appl. Phys. Lett.*, 97:244102, 2010. Cited on 115

[88] Jaroslaw Labaziewicz, Yufei Ge, Paul Antohi, David Leibrandt, Kenneth R. Brown, and Isaac L. Chuang. Suppression of heating rates in cryogenic surface-electrode ion traps. *Phys. Rev. Lett.*, 100:013001, Jan 2008. Cited on 115

[89] J. I. Cirac and P. Zoller. A scalable quantum computer with ions in an array of microtraps. *Nature*, 404:579–581, April 2000. Cited on 117

[90] C. Ospelkaus, C. E. Langer, J. M. Amini, K. R. Brown, D. Leibfried, and D. J. Wineland. Trapped-ion quantum logic gates based on oscillating magnetic fields. *Phys. Rev. Lett.*, 101:090502, Aug 2008. Cited on 117

[91] Michael Johanning, Andrés F Varón, and Christof Wunderlich. Quantum simulations with cold trapped ions. *Journal of Physics B: Atomic, Molecular and Optical Physics*, 42(15):154009, 2009. Cited on 117, 140

[92] R. Gerritsma, B. P. Lanyon, G. Kirchmair, F. Zähringer, C. Hempel, J. Casanova, J. J. García-Ripoll, E. Solano, R. Blatt, and C. F. Roos. Quantum simulation of the Klein paradox with trapped ions. *Phys. Rev. Lett.*, 106:060503, Feb 2011. Cited on 117

[93] Ch Schneider, Diego Porras, and Tobias Schaetz. Experimental quantum simulations of many-body physics with trapped ions. *Reports on Progress in Physics*, 75(2):024401, 2012. Cited on 117

[94] K. Kim, S. Korenblit, R. Islam, E. E. Edwards, M-S. Chang, C. Noh, H. Carmichael, G-D. Lin, L-M. Duan, C. C. Joseph Wang, J. K. Freericks, and C. Monroe. Quantum simulation of the transverse Ising model with trapped ions. *New Journal of Physics*, 13(10):105003, 2011. Cited on 117

[95] A. Friedenauer, H. Schmitz, J. T. Glueckert, D. Porras, and T. Schaetz. Simulating a quantum magnet with trapped ions. *Nature Physics*, 4:757–761, July 2008. Cited on 117

[96] R. Islam, E.E. Edwards, K. Kim, S. Korenblit, C. Noh, H. Carmichael, G.-D. Lin, L.-M. Duan, C.-C. Joseph Wang, J.K. Freericks, and C. Monroe. Onset of a quantum phase transition with a trapped ion quantum simulator. *Nature Communications*, 2(377), July 2011. Cited on 117

[97] K. Kim, M.-S. Chang, S. Korenblit, R. Islam, E.E. Edwards, J.K. Freericks, G.-D. Lin, L.-M. Duan, and C. Monroe. Quantum simulation of frustrated ising spins with trapped ions. *Nature*, 465:590–593, June 2010. Cited on 117

[98] Simcha Korenblit, Dvir Kafri, Wess C. Campbell, Rajibul Islam, Emily E. Edwards, Zhe-Xuan Gong, Guin-Dar Lin, Luming Duan, Jungsang Kim, Kihwan Kim, and Chris Monroe. Quantum simulation of spin models on an arbitrary lattice with trapped ions. *arXiv:1201.0776v1*, 2012. Cited on 117

[99] J. Chiaverini and W. E. Lybarger. Laserless trapped-ion quantum simulations without spontaneous scattering using microtrap arrays. *Phys. Rev. A*, 77:022324, Feb 2008. Cited on 117

[100] Florian Mintert and Christof Wunderlich. Ion-trap quantum logic using long-wavelength radiation. *Phys. Rev. Lett.*, 87:257904, Nov 2001. Cited on 117

[101] A. Khromova, Ch. Piltz, B. Scharfenberger, T. F. Gloger, M. Johanning, A. F. Varón, and Ch. Wunderlich. Designer spin pseudomolecule implemented with trapped ions in a magnetic gradient. *Phys. Rev. Lett.*, 108:220502, Jun 2012. Cited on 117

[102] Roman Schmied, Janus H. Wesenberg, and Dietrich Leibfried. Optimal surface-electrode trap lattices for quantum simulation with trapped ions. *Phys. Rev. Lett.*, 102:233002, Jun 2009. Cited on 118

[103] Roman Schmied, Janus H. Wesenberg, and Dietrich Leibfried. Quantum simulation

of the hexagonal Kitaev model with trapped ions. *New Journal of Physics*, 13:115011, 2011. Cited on 118

[104] Muir Kumph, Michael Brownnutt, and Rainer Blatt. Two-dimensional arrays of radio-frequency ion traps with addressable interactions. *New Journal of Physics*, 13:073043, July 2011. Cited on 118, 121

[105] Harald Wunderlich, Christof Wunderlich, Kilian Singer, and Ferdinand Schmidt-Kaler. Two-dimensional cluster-state preparation with linear ion traps. *Phys. Rev. A*, 79:052324, May 2009. Cited on 118

[106] Xu You-Yang, Zhou Fei, Zhang Xiao-Long, and Feng Mang. Fast generation of cluster states in a linear ion trap. *Chinese Physics B*, 19(9):090317, 2010. Cited on 118

[107] C. Langer, R. Ozeri, J. D. Jost, J. Chiaverini, B. DeMarco, A. Ben-Kish, R. B. Blakestad, J. Britton, D. B. Hume, W. M. Itano, D. Leibfried, R. Reichle, T. Rosenband, T. Schaetz, P. O. Schmidt, and D. J. Wineland. Long-lived qubit memory using atomic ions. *Phys. Rev. Lett.*, 95:060502, Aug 2005. Cited on 119

[108] Charles Kittel. *Introduction to Solid State Physics*. New York: John Wiley and Sons, 1996. Cited on 121

[109] D. Mc Hugh and J. Twamley. Quantum computer using a trapped-ion spin molecule and microwave radiation. *Phys. Rev. A*, 71:012315, Jan 2005. Cited on 121

[110] Roman Schmied. Electrostatics of gapped and finite surface electrodes. *New Journal of Physics*, 12:023038, February 2010. Cited on 122

[111] Kilian Singer, Ulrich Poschinger, Michael Murphy, Peter Ivanov, Frank Ziesel, Tommaso Calarco, and Ferdinand Schmidt-Kaler. Colloquium: Trapped ions as quantum bits: Essential numerical tools. *Rev. Mod. Phys.*, 82:2609–2632, Sep 2010. Cited on 123

[112] X.-L. Deng, D. Porras, and J. I. Cirac. Effective spin quantum phases in systems of trapped ions. *Phys. Rev. A*, 72:063407, Dec 2005. Cited on 138, 139

[113] P. C. Haljan, K.-A. Brickman, L. Deslauriers, P. J. Lee, and C. Monroe. Spin-dependent forces on trapped ions for phase-stable quantum gates and entangled states of spin and motion. *Phys. Rev. Lett.*, 94:153602, April 2005. Cited on 139

[114] R. Ozeri, W. M. Itano, R. B. Blakestad, J. Britton, J. Chiaverini, J. D. Jost, C. Langer, D. Leibfried, R. Reichle, S. Seidelin, J. H. Wesenberg, and D. J. Wineland. Errors in trapped-ion quantum gates due to spontaneous photon scattering. *Phys. Rev. A*, 75:042329, April 2007. Cited on 142

[115] D. J. Wineland, M. Barrett, J. Britton, J. Chiaverini, B. DeMarco, W. M. Itano, B. Jelenković, C. Langer, D. Leibfried, V. Meyer, T. Rosenband, and T. Schätz. Quantum information processing with trapped ions. *Phil. Trans. R. Soc.*, 361(1808):1349–1361, July 2003. Cited on 142

[116] W. C. Campbell, J. Mizrahi, Q. Quraishi, C. Senko, D. Hayes, D. Hucul, D. N. Matsukevich, P. Maunz, and C. Monroe. Ultrafast gates for single atomic qubits. *Phys. Rev. Lett.*, 105:090502, August 2010. Cited on 142

[117] J. Welzel, A. Bautista-Salvador, C. Abarbanel, V. Wineman-Fisher, C. Wunderlich, R. Folman, and F. Schmidt-Kaler. Designing spin-spin interactions with one and two dimensional ion crystals in planar micro traps. *Eur. Phys. J. D*, 65:285–297, 2011. Cited on 146

[118] D. T. C. Allcock, L. Guidoni, T. P. Harty, C. J. Ballance, M. G. Blain, A. M. Steane, and D. M. Lucas. Reduction of heating rate in a microfabricated ion trap by pulsed-laser cleaning. *New Journal of Physics*, 13:123023, 2011. Cited on 148

[119] D. A. Hite, Y. Colombe, A. C. Wilson, K. R. Brown, U. Warring, R. Jördens, J. D. Jost, D. P. Pappas, D. Leibfried, and D. J. Wineland. Reduction of anomalous heating in an in-situ-cleaned ion trap. *arXiv:1112.5419v1*, 2011. Cited on 148

Appendix A

Additional calculations for including motional heating rate in simulation error

The simulation error in equation 8.27 can be adjusted to take into account the heating of the ions during a simulation. If this occurs the mean radial phonon number $\overline{n}$ will become time dependent, $\overline{n}(t)$. It, therefore, follows that the error will also become time dependent and is given by

$$E_0(t) \approx \frac{F^2 M(\overline{n}(t) + \frac{1}{2})}{2\hbar m\omega^3}. \tag{A.1}$$

The time dependent mean radial phonon number will be a function of the heating rate $\dot{n}$, the interaction time, T_J, and the initial mean phonon number, $\overline{n}_0$ and is given by

$$\overline{n}(T_J) = \overline{n}_0 + \dot{n}T_J \tag{A.2}$$

yielding an error given by

$$E_0(T_J) \approx \frac{F^2 M(\overline{n}_0 + \dot{n}T_J + \frac{1}{2})}{2\hbar m\omega^3}. \tag{A.3}$$

It should be noted here that $\dot{n}T_J = 1/K_{sim}$ and so the error can be expressed as

$$E_0(T_J) \approx \frac{F^2 M(\overline{n}_0 + \frac{1}{K_{sim}} + \frac{1}{2})}{2\hbar m\omega^3}. \tag{A.4}$$

Equation A.4 shows that as K_{sim} increases the error will tend towards that in equation 8.27 in section 8.6.2 for the case of $\bar{n} \ll 1$. This is because higher values of K_{sim} mean that less heating takes place during an interaction until the mean radial phonon number can be approximated as constant.

Appendix B

K_{sim} with alternate heating rate scaling

In the work presented we have used a motional heating rate, $\dot{n}$, which has an r^{-4} scaling, where r is the ion height. However the scaling of this anomalous heating has not yet been fully understood and so it is conceivable that a different scaling will be required to describe the effect. For this reason it is the aim of this appendix to outline the steps and main expressions required to obtain an optimised two-dimensional ion trap array with an anomalous heating rate which possess an arbitrary scaling with the ion height r^{-x}.

For the case of optimising the homogeneity of K_{sim} across an array the results shown in section 8.4.1 will hold for any scaling of the heating rate with ion height. This is because this optimisation aims to give each trapping site in the array the same properties and this is independent of the heating rate. The same applies to the optimisation of the number of polygon sides described in section 8.4.2.

Equation 8.19 describing K_{sim} for an optimised geometry can be altered to take into account a different scaling of the heating rate with ion height. For an arbitrary scaling r^{-x} this equation can be expressed as

$$K_{sim} = \frac{4F^2 m k_r^{(4+x)} \alpha^{(x-1)}}{\Xi \eta_{geo}^2 \pi \epsilon_0 k_A^3}. \tag{B.1}$$

It can be seen in equation B.1 that the K_{sim} is proportional to $\alpha^{(x-1)}$. The values of k_r, k_A and k_R (described in section 8.4.3) are independent of the value of x and, so, the optimum geometry for a given α will be the same regardless of the scaling of the heating rate with ion height. Using this procedure optimum geometries can be computed for an

arbitrary scaling of the anomalous heating with the ion height, r^{-x}.